

LABORATOIRE LEON BRILLOUIN

ANNUAL REPORT 2014





INSIDE PA20 : A NEW SANS/GISANS INSTRUMENT AT LLB



ANNUAL
REPORT
LABORATOIRE
LEON BRILLOUIN

**2
0
1
4**

TABLE OF CONTENTS

ABOUT THE LLB	5
EVENTS AND WORKSHOPS	9
<i>International year of crystallography</i>	10
<i>Participation organization international meetings</i>	11
<i>Visiting committee</i>	12
<i>Workshops</i>	13
YEAR IN REVIEW	15
SCIENTIFIC HIGHLIGHTS	18
<i>Axe 1 Magnetism and superconductivity</i>	21
<i>Axe 2 Materials and nanosciences</i>	33
<i>Axe 3 Soft matter and biophysics</i>	45
PUBLICATIONS	57
NEWS FROM THE SPECTROMETERS	65
TEACHING AND EDUCATION	73
BEAM TIME ACCESS	79

ABOUT THE LLB



Christiane Alba-Simionesco
Director of LLB

Using the Orphée reactor as its principle neutron resource, the Laboratoire Léon Brillouin (LLB) is the hub for neutron scattering in France connecting researchers, academic or industrial, instrument developers and other scientific facilities in France or in Europe. It is part of and profits from the exceptional scientific environment provided by the “Plateau de Saclay”, which includes the synchrotron radiation source SOLEIL and renown Universities and Engineering Schools. LLB plays a critical role in preserving and developing the French know-how in neutron based research. This includes training new users, providing critical access to neutrons for established users, and developing a cohort of French researchers and engineers who know how to build and develop instrumentation.

In 2014, the LLB welcomed a large number of students for education and training and for their first experiments; the LLB celebrated **the year of Crystallography** and also supported number of scientific and instrumental workshops to promote and make popular the use of neutron probe. New instruments were open to the user program completing the instrument suite available so far.



Finally in December 2014, France was the first country to have announced the signature of a letter of intent of commitment to the construction of the ESS in Lund; the LLB teams will be strongly involved in the construction of the most performing scientific instruments as well as their scientific operation. The first instruments in which the LLB will participate were approved by the Steering Committee of the ESS and collaboration plans with the ESS and our German partners are under discussion.

The educative role of the LLB was particularly important in 2014: we welcomed 110 students for practical classes on our spectrometers via different schools and European Masters.



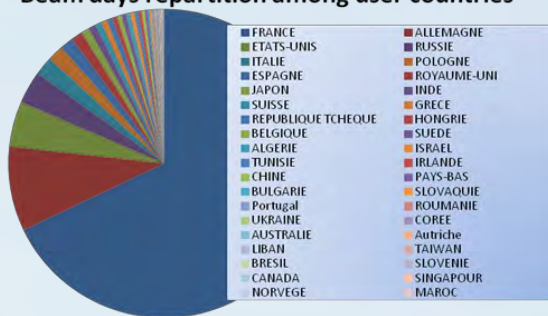
UPPSALA
UNIVERSITET

In addition **hundred PhD students below 30 years, defending their own proposals, were helped and accompanied in all the stages of their experiment; among them, 36% were young women (85 young men and 48 young women).**



Visit of Swedish students
in June 2014

Beam days repartition among user countries



The beam team access of the instrumentation is open to the French and worldwide International user community under the condition of scientific merit. The figures below illustrate the strong Interconnection of the scientific community applying for beam time and realizing their experiments at the LLB

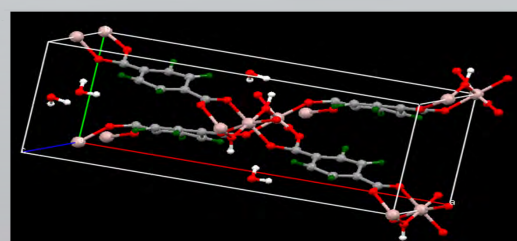
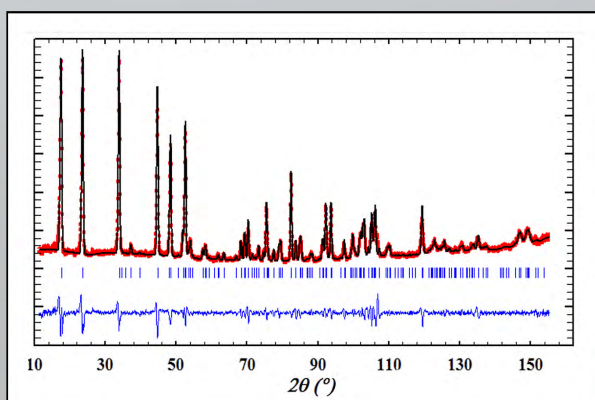
Origin of the French and European users coming at the LLB



LLB/Orphée covers 60% of the neutron scattering needs of the French research community in most of the neutron scattering methods.

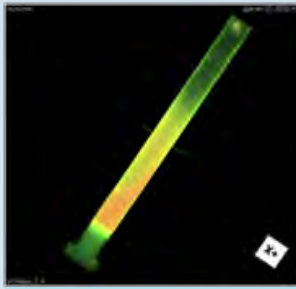
New instruments were open to users in 2014 :

The new cold, high resolution diffractometer G4.4, completes the existing suite of diffractometers with a high-performance, high-resolution, long-wavelength machine. The instrument fills a gap in the existing LLB capability, providing access to high-resolution studies of large unit cells, and will address a wide ranging science program. The instrument entered the user program this year and is operating very successfully.



Pattern matching of the closed hydrated phase of the MIL-53(Al)

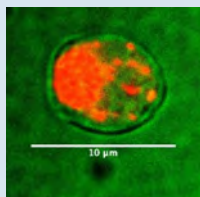
The New 3He Detector for the SANS instrument PAXY open to users in January 2014 : The observed gain in detector efficiency and measured intensities are by a factor of 6 at 4-6Å up to a factor of 10 at 10-12Å



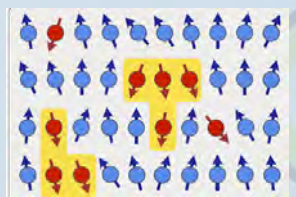
Hydrogen uptake in Zircalloy fuel elements

The instrument IMAGINE is a new imaging instrument that effectively extends the region of real space that can be measured at the facility and will attract a large range of industrial users provided its capabilities can be widely advertised. The instrument has been open to friendly users since April 2014 and is beginning to deliver interesting results on agro-food applications, cultural heritage and in operando experiments.

One can predict that the capability for in-bulk examination of parts will be a critical analysis tool for the additive manufacturing community.



In an effort to prepare future generations of French researchers in the use of multiple tools for research, and at the same time to increase the collaboration between LLB and Soleil the two facilities launched a joint program of PhD on selected subjects since 2012.



This highly successful program grants two or three PhD theses each year. The projects should include a third partner, typically a university research group, who is expected to provide half of the required PhD funding. Such a process favors external collaborations and provides visibility/awareness of both LLB and Soleil. It should be noted that the project selection is scheduled several months before the opening of most of the PhD grant calls and the project acceptance is known very soon.

This makes it easier for the third partner to find the additional funding and a very good and motivated candidate.



The Scientific and Instrumental Council of the LLB, (Chairman Ian Anderson, G. Gébel, J. Daillant, R. Pynn, R. McGreevy, C. Lecomte) evaluated **the effectiveness of building joint**



research programs with the synchrotron facility Soleil: all CSI members agreed on the excellent quality of the science as evidenced by the very clear and lively presentations across a large variety of scientific domains. In order to solve their scientific problems, the PhD students were expected to carry out both neutron and synchrotron experiments, and hence become familiar with these techniques in addition to the usual laboratory methods.





	2
EVENTS	0
AND	1
WORKSHOPS	4

ACTIONS FROM LLB

One member representing (SFN then) LLB in the national committee for IYCr in France: B. Gillon + (W. Paulus for SFN)

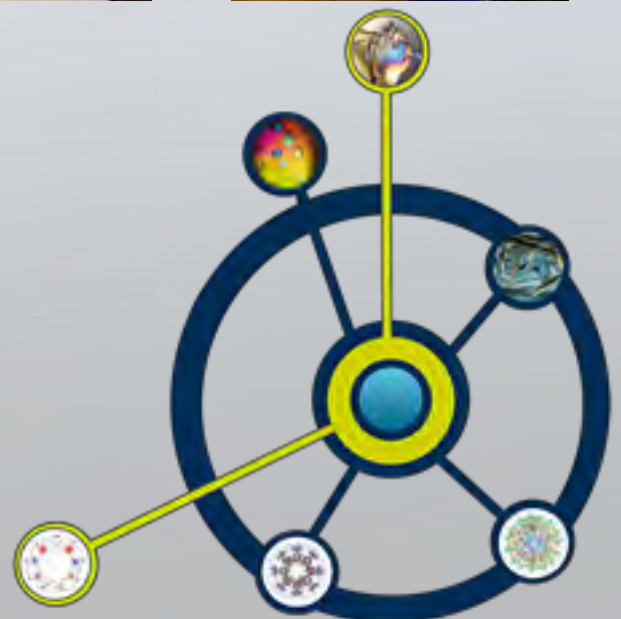
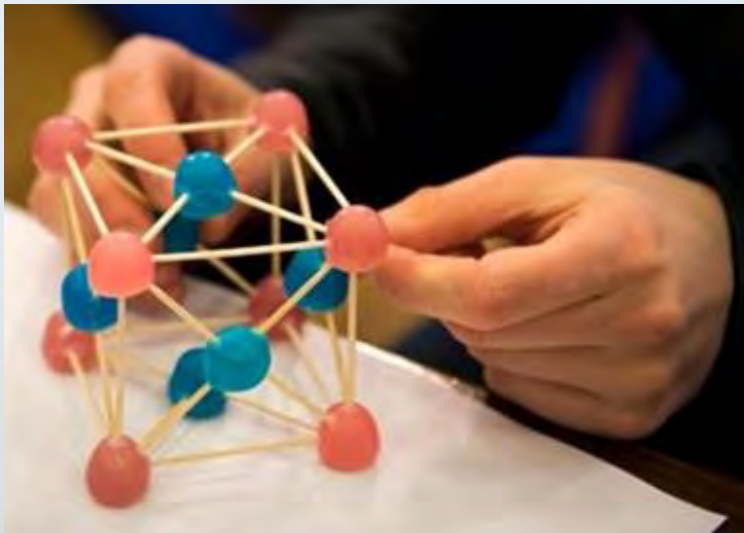
Participation to the construction of the website www.aicr2014.org

- contributions on neutron diffraction on the website (B. Gillon, F. Porcher)
- 2 exhibition panels about neutrons (B. Gillon + CA SFN)



Actions:

- Participation to the organization of international meetings on crystallography in France
- Actions towards public and children
- Publications



PARTICIPATION TO THE ORGANIZATION OF INTERNATIONAL MEETINGS

17-19th January 2014
Festival de la cristallographie
Les Cordeliers, Paris



Exhibition « Voyage dans le cristal »
Public presentation by F. Porcher (LLB)
Workshop with 15 presenters from the LLB

22nd January 2014
« Crystallography,
A key for knowledge »



International Conference

23th January 2014
9th Soleil User meeting



Session Soleil-LLB on Crystallography

29th April 2014
Forum « Faites de la science »



B. Gillon et F. Porcher

22-25th May 2014
15e Salon Culture et
Jeux mathématiques, Paris



Workshop with B. Gillon

27th May 2014
Remise des prix concours national
de croissance cristalline, Paris



C. Loupiac
« Nous sommes entourés de cristaux
Les cristaux sont partout »



6th July 2014
CNAM, Paris

- 3 LLB Workshops : C. Loupiac, S. Scussat, A. Bataille, F. Porcher, B. Gillon, L. Noirez
- Public Presentation « Des bonbons au chocolat: des cristaux à déguster » C. Loupiac
Film CNRS : <http://www.cnrs.fr/cristallo/spip.php?article189>

21-24th September 2014, Oléron Island, France
International school : « Crystallography and neutrons »

Organizers:
JM Kiat (ECP),
F. Porcher, B. Gillon (LLB)
MT Fernandez-Diaz (ILL)



13-17th October 2014 - 4e Ecole de Cristallographie

- Participation to the organization of courses on crystallography :
A. Bataille, F. Bourée, F. Damay, F. Porcher
- One member representing LLB in the scientist committee : A. Melle

VISITING COMMITTEE - JANUARY 30 - 31ST 2014



On behalf of AERES :

- Mr. Didier HOUSSIN, president
- Mr. Pierre GLAUDES, head of the evaluation of research units department

On behalf of the expert committee,

Mr. Winfried PETRY,
chair of the committee

The visit of the AERES committee took place from 30th to 31st January 2014 in the buildings of the LLB. An extensive visit of the instrumentation around ORPHÉE was part of the program. The evaluation has considered all the missions of the research infrastructure:

- Research on its own scientific programs.
- Promotion of the use of neutrons within the French academic and scientific community, dissemination of knowledge around the use of neutron radiation, academic education.
- Development, construction and operation of an international competitive instrument suite at ORPHÉE.
- Open access of the instrumentation of LLB to the French and international user community under the condition of scientific merit, and providing full support for external users with the ultimate aim of publication of the scientific results achieved.

And since 2013:

- Being the French bridgehead for the scientific exploitation of the upcoming European Spallation Source (ESS) at Lund, Sweden.

The committee has emphasized the strengths of the LLB: its neutron source ORPHÉE, its own research, the instrumental program and the open access.

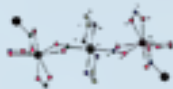
A few weaknesses have been observed: the age pyramid of the permanent staff, the perspective of a shutdown of Orphee in 2020, and an insufficient involvement of the French universities at LLB.

Recommendations concern: increase of relation with French universities and foreign partners using the opportunity of the creation of Paris-Saclay university, potential for further developments of industrial projects, full operation of ORPHEE until 2025, creation of a task force developing ideas for future French neutron source, and maintain the level of staffing.

The full report of the Committee can be found on the AERES Website : <http://www.aeres-evaluation.fr>



WORKSHOPS



International workshop "Magnetism single crystal diffractometer at the ESS" May 26-27th 2014, FIAP Jean Monnet, Paris.



It took place in Paris at the FIAP on May 26-27th 2014. It was organized by the Laboratoire Léon Brillouin and joined neutron experts and users of in order to evaluate the perspectives of single crystal diffraction at the ESS and uncover the most important scientific community needs in this field. LLB intends to propose the construction of a single crystal diffractometer dedicated to Magnetism at the ESS (Sweden) as an in-kind French contribution.

The meeting focused on recent results obtained by Single Crystal Neutron Diffraction (SCND) in the studies of multiferroics, frustrated and low-dimensional magnetic systems, molecular magnetism and new instrumental developments using polarized neutrons. 27 participants from the main European neutron centers attended the conference.



"Low Energy Electrodynamics in Solids" from June 29th to July 4th, 2014 - Villa Bellagio, France



The LEES'14 meeting was attended by almost 150 participants from 16 countries and 75 institutions. LEES'14 was also the occasion for Dr. Rainer Hillenbrand, to receive the Genzel Prize and to distinguish four Poster Prize winners.

The organizing committee: Alain Sacuto (Paris 7), Pascale Roy (Soleil), Ricardo Lobo (CNRS), Philippe Bourges (CEA), François Gervais (Univ. Tours).



"Neutrons and Food 3" from July 9th to 11th of July 2014 - Paris, France



"Neutrons and Food 3" was held inside Paris at "La Maison du Lait" from Wednesday 9th to Friday 11th of July 2014, and was co-organized by AgroSup Dijon and Laboratoire Léon Brillouin (F.Cousin).

An introduction to Neutron Scattering and a visit of the reactor Orphée was proposed during the conference.



Neutron imaging workshop 7-8th July 2014



The neutron imaging workshop was a satellite meeting of the main conference "neutrons and food 3". The main aim was to present the new neutron imaging station of the Laboratoire Léon Brillouin "IMAGINE" and to discuss possible application of neutron imaging to study complex materials. A common session of this neutron imaging workshop and "neutrons end food 3" included a visit of the reactor at Orphee.



**2
0
1
4**
YEAR
IN REVIEW

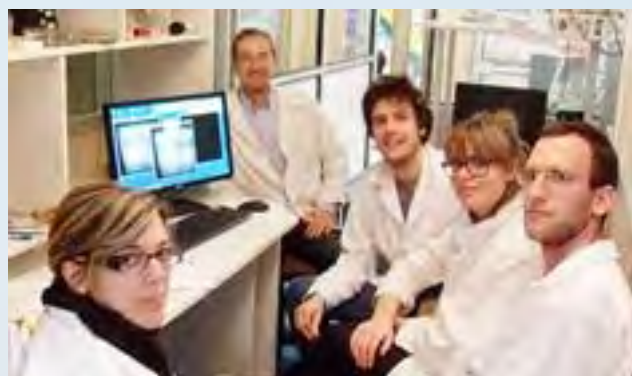


February 13th

General Meeting

**From February 23rd
to March 26th**

Hercules European School



June 20th

CEA Inter-services Relay Runner



June 26th

Day of the Young Researchers

July 08th

Workshop Imagery



September 30th

Lab Tour with the Deputy Scientific Director of the Physical Sciences Direction (DSM)

October 27th

Council for Science and Instrumentation



During the Year

Setting up of the PA20 spectrometer





2
0
1
4

SCIENTIFIC
HIGHLIGHTS

AXE 1

Strongly Correlated
Quantum Materials
and Magnetism.

AXE 2

Materials &
Nanosciences:
Fundamental
Studies
and Applications.

AXE 3

Soft Matter
& Biophysics.



AXE 1:

MAGNETISM AND SUPER CONDUCTIVITY

The scientific programs developed by condensed matter physicists at LLB cover a large number of research areas, at the forefront of science and technologies, ranging from strongly correlated electron systems and complex magnetic systems to modern functional magnetic materials. These programs involving the French and international research communities rely on the unique possibilities offered by neutron scattering techniques to explore a whole spectrum of physical phenomena occurring in condensed matter. The study of static and dynamical magnetic correlations through neutron scattering is essential to describe the microscopic state and understand the fundamental properties of these systems. Research areas investigated at LLB cover a broad range of subjects, among which unconventional superconductors, exotic ground states in 4f-electron systems, frustrated spin liquids or spin ices, quantum criticality and functional magnetic materials.

In this issue, we focus on modern functional magnetic materials with complex noncollinear spin structures. Since macroscopic functional responses are direct consequences of complex magnetic structures and of the fine tuning of magnetic interactions, the detailed knowledge of crystal and magnetic structures, and magnetic excitation spectra is mandatory. Both the Mn_2RhSn Heussler magnet and MnGe chiral magnet offer the possibility to tune spin textures, through temperature, pressure or magnetic field. In the frustrated $\text{Dy}_4\text{Ru}_3\text{Al}_{12}$ with distorted Kagome network, the noncollinear spin structure was solved in zero magnetic field, a first step in the understanding of its field induced transitions, which are accompanied with large magnetoresistance effects. In the BiFeO_3 multiferroic, whose magnetic domain structure is tuned by an electric field, the study of spin wave excitations leads to the appropriate modelling of the relevant magnetic interactions. Finally, in a Mn^{3+} spin-crossover molecular complex, the investigation of the crystal field transitions allowed one to determine the anisotropic energy terms on each side of its spin transition temperature.

- **Large Noncollinearity and Spin Reorientation in the Novel Mn_2RhSn Heussler Magnet**
O. Meshcheriakova, S. Chadov, A. K. Nayak, U. K. Rößler, J. Kübler, G. André, A. A. Tsirlin, J. Kiss, S. Hausdorf, A. Kalache, W. Schnelle, M. Nicklas, C. Felser
- **Stress induced magnetic textures in MnGe chiral magnet**
M. Deutsch, A. V. Tsvyashchenko, F. Porcher, I. Mirebeau
- **Electronic properties of a distorted kagome lattice antiferromagnet $\text{Dy}_3\text{Ru}_4\text{Al}_{12}$**
D.I. Gorbunov, M.S. Henriques, A.V. Andreev, A. Gukasov, V. Petříček, N.V. Baranof, Y. Skourski, V. Eigner, M. Paukov, J. Prokleška, A.P. Gonçalves
- **Temperature-Dependent Interplay of Dzyaloshinskii-Moriya Interaction and Single-Ion Anisotropy in Multiferroic BiFeO_3**
J. Jeong, M. D. Le, P. Bourges, S. Petit, S. Furukawa, S. A. Kim, S. Lee, S. W. Cheong, J. G. Park
- **Magnetic neutron spectroscopy of a spin-transition Mn^{3+} molecular complex**
K. Ridier, S. Petit, G. André, B. Gillon, G. Chaboussant, D. A. Safin, Y. Garcia

NON-COLLINEAR MAGNETISM IN Mn_2RhSn HEUSLER COMPOUND

O. Meshcheriakova^a, S. Chadov^a, A. K. Nayak^a, U. Rößler^b, J. Kübler^c,
G. André^d, A. A. Tsirlin^a, J. Kiss^a, W. Schnelle^a, M. Nicklas^a, C. Felser^a

a Max Planck Institute for Chemical Physics of Solids, Dresden, Germany

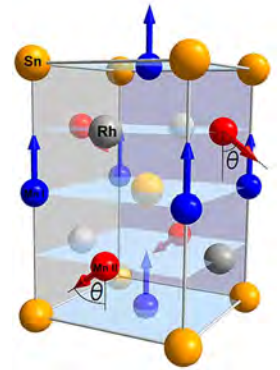
b Leibnitz Institute for Solid State and Materials Research, Dresden, Germany

c Institute for Solid State, Technical University Darmstadt, Germany

d Laboratoire Léon Brillouin, CEA-CNRS, CEA-Saclay, Gif-sur-Yvette, France

claudia.felser@cpfs.mpg.de

Non-collinear magnetic states can be used for the next generation memory technology. Heusler compounds are a large class of materials, whose industrial parameters are easy to tune: lattice constant, Curie temperature, spin polarization, magnetic moment, etc. Typically, these materials exhibit simple spin arrangements: such as ferro- or ferrimagnetism. Here we report a large canting between two Mn-sublattices in the Mn_2RhSn sample and the evolution of magnetic structure with temperature. An absence of inversion symmetry and a strong spin-orbit coupling enable the possibility of a skyrmion phase.



Heusler alloys¹ are ternary compounds (X_2YZ) having a main group element Z and two transition metals X, Y. In a regular Heusler structure X element occupies (1/4, 1/4, 1/4) Wyckoff position, Y and Z (1/2, 1/2, 1/2) and (0, 0, 0) respectively. In case Y element has a higher electronegativity than the X element, the structure inverts: X element becomes equally distributed between (1/2, 1/2, 1/2) and (3/4, 3/4, 3/4) Wyckoff sites. The Mn_2RhSn exhibits an inverse tetragonal $I-4m2$ Heusler structure (see Fig. 1), which onsets from the high-temperature cubic phase at about 570°C and preserves down to 50 K. Such structure has no inversion symmetry and therefore allows for the Dzyaloshinskii-Moriya interactions, which are responsible for the long-range magnetic modulations³.

Here, Rh and Sn carry almost no magnetic signal; the magnetism is mainly contributed by the two Mn atoms. The total magnetic moment of a bulk polycrystalline sample is $2 \mu_B$ per formula unit, which suggests that the octahedrally and tetrahedrally coordinated Mn sublattices align at least in the opposite directions. The magnetic order of Mn_2RhSn was found from the first-principles calculations and tested

experimentally by the neutron powder scattering. In the ground state the materials is a canted ferrimagnet with the angle of about $(180 \pm 55)^\circ$ theoretically and $(180 \pm 59)^\circ$ experimentally.

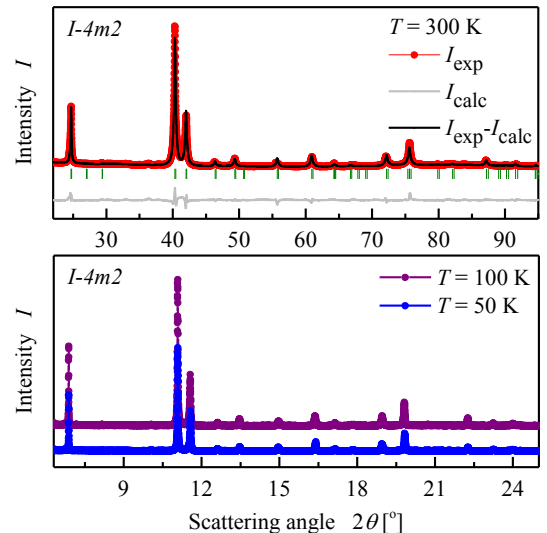


Figure 1 : Powder X-ray patterns obtained at room temperature (top) and 50 and 100 K (bottom). Incident light wavelengths of $\lambda = 1.5405 \text{ \AA}$ and 0.43046 \AA were used for the room- and low-temperature measurements, respectively.

The canting establishes as a result of the competing antiferromagnetic exchange interactions between the nearest and the

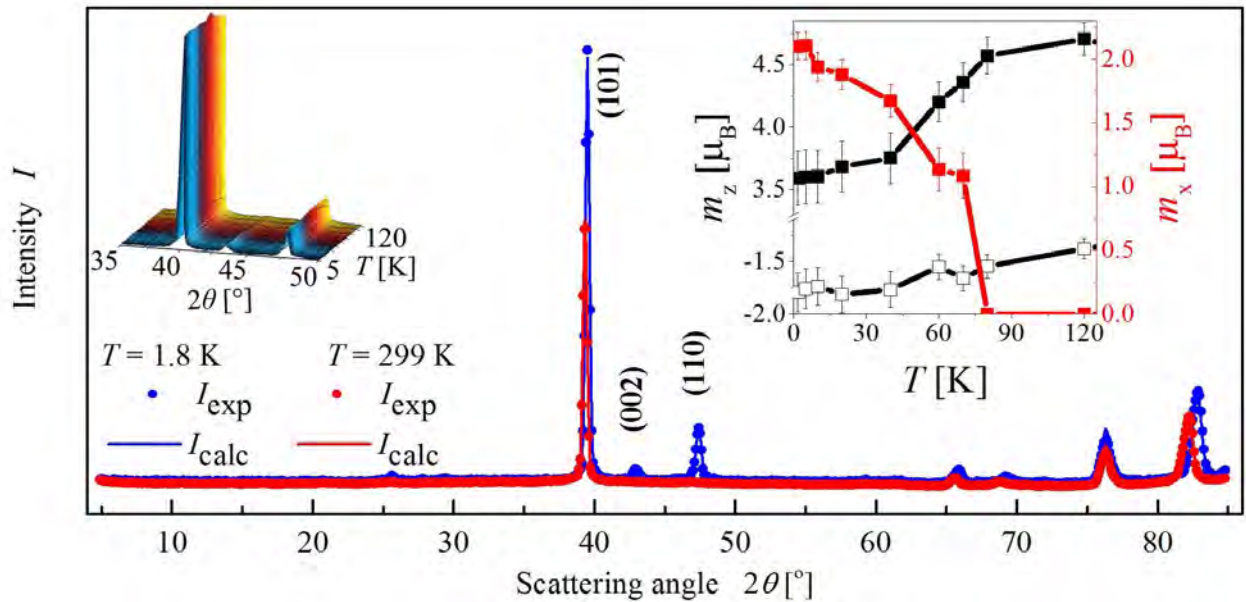


Figure 2 : Powder neutron scattering patterns obtained at 299 K (red) and 1.8 K (blue) using the wavelength of $\lambda=2.422 \text{ \AA}$. Main magnetic intensity is added to the (101), (002) and (110) peaks. Left inset: temperature-dependent neutron spectra, at the temperatures below 80 K the (002) peak gradually increases. Right inset: development of the in-plane magnetism (produced by $Mn_{ii}xy$ -component, closed red marks) suppresses the z-component of Mn_i (closed black marks), while the z-component of Mn_i evolves rather insignificantly (open black marks).

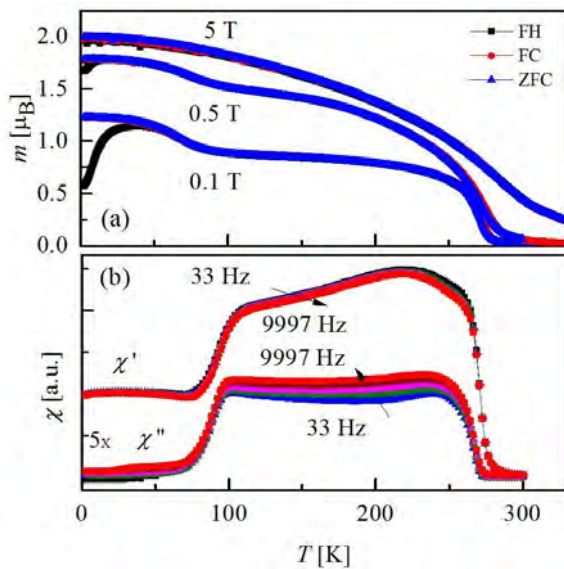


Figure 3 : (a) Zero-field cooled (ZFC), field-cooled (FC) and field-heated (FH) magnetization as a function of the temperature measured at different induction fields; two transitions are observed - at 270 K and in the range of 100–50 K. (b) Real (χ') and imaginary (χ'') parts of the ac-susceptibility are frequency-independent and show confirm the transitions by two pronounced steps: at 270 K and at about 80 K.

next-nearest planes; moments couple stronger between the planes than within them.

As the temperature rises, the magnetic structure evolves: the total magnetization decreases from 1.8 K to 80 K (see Fig. 3 (a)). This transition is observed in weak fields and smears by the stronger field of 5 T. The process is attributed to the gradual spin reorientation transition of the tetrahedrally coordinated Mn sublattice from canted to a collinear ferrimagnetic state; the in-plane magnetic component vanishes (see Fig. 2, right inset). The onset of a ferrimagnetic phase is accompanied by the step in ac-susceptibility data (see Fig. 3 (b)). This collinear regime provides perfect conditions for the skyrmion formation, which is a subject of future investigations.

References

1. F. Heusler, Verhandlungen der Deutschen Physikalischen Gesellschaft 12, 219, 1903 Silva, S. P.; Sabino, M. A.; Fernandes, E. M.; Correlo, V. M.; Boesel, L. F.; Reis, R. L., Int. Mater. Rev. 2005, 50, 345-365
2. O. Meshcheriakova, S. Chadov, A.K. Nayak, U.K. Röbler, J. Kübler, G. André, A.A. Tsirlin, J. Kiss, S. Hausdorf, A. Kalache, W. Schnelle, M. Nicklas, C. Felser, Phys. Rev. Lett. 113, 087203, 2014.
3. A.N. Bogdanov, U.K. Röbler, M. Wolf, K.-H. Müller, Phys. Rev. B 66, 214410, 2002.

STRESS INDUCED MAGNETIC TEXTURES IN MnGe CHIRAL MAGNET

M. Deutsch^a, A. V. Tsvyashchenko^b, F. Porcher^a, I. Mirebeau^a

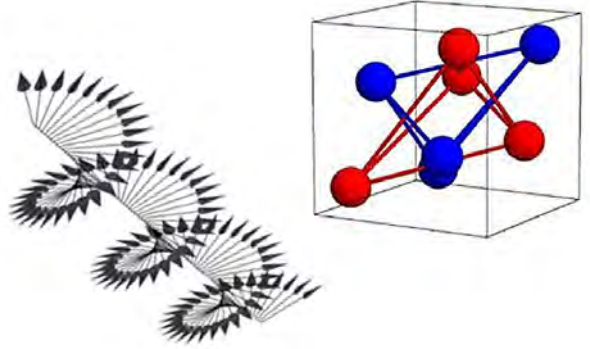
Chiral magnets show long period helical structures with potential use in spintronics. We have studied MnGe chiral magnet by neutron diffraction under anisotropic pressure. We observe a strong magnetic texture induced by the stress, where the helical axes reorient along the stress axis. We attributed this reorientation to the grown of helical domains in order to minimize the magnetoelastic energy. Our result suggest that the ambient pressure state at zero field and zero temperature is a multidomain state of helical domain

and not the complex skyrmionic texture previously postulated to explain the giant Topological Hall effect shown by MnGe.

a Laboratoire Léon Brillouin, CEA-CNRS, CEA-Saclay, Gif-sur-Yvette, France

b Institute for High Pressure Physics, Troitsk, Russia

isabelle.mirebeau@cea.fr



Chiral magnets of the B20 family (Top figure) attract increasing attention by their complex and highly tunable spin structures, potentially usable for applications in spintronics [1]. Within this family MnGe stands apart due to its peculiar properties. Cubic MnGe exists in metastable and powdered form and must be synthesized under high pressure and high temperature conditions. The strong spin orbit coupling results in the shortest helix pitch of the B20 family (29Å instead of 180Å in MnSi

and 700Å in FeGe). The helical order is shown by neutron scattering through the satellite of the (000) Bragg peak (Figure 1) which appears below $T_N=170\text{K}$ [2]. Under magnetic field MnGe exhibits giant topological Hall Effect and giant Nernst effect, which makes it promising for spintronic applications [4]. To explain these features, it was postulated that MnGe shows up a lattice of vortex like defects, also called “skyrmions”. This skyrmion lattice cannot be visualized directly due to the powder form of the sample, so its existence was inferred from resistivity [3] and small angle neutron scattering data in applied field. In contrast with other chiral magnets, this skyrmion lattice would persist even at $T=0$ and in zero magnetic field, realizing a complex pattern of skyrmions and antiskyrmions, with no net magnetization [4].

We have checked this model by applying an anisotropic pressure with uniaxial component or stress. We show that a small stress is sufficient to induce a strong magnetic texture, clearly visible on the 2D newly installed multidetector (Figure 2). The anisotropy of the spin distribution in the detector plane is readily interpreted by a reorientation of the helical axes along the axis of the pressure

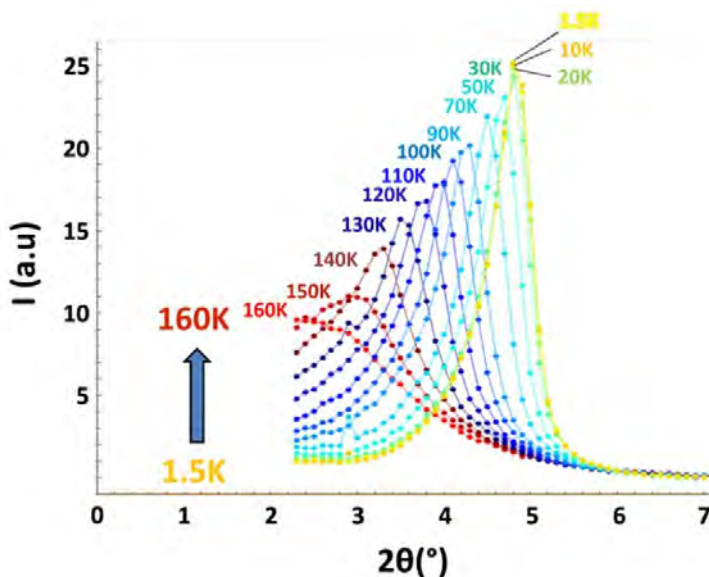


Figure 1 : Onset of the zero satellite below $T_N=170\text{K}$ at ambient pressure, measured on G4.1 at LLB.

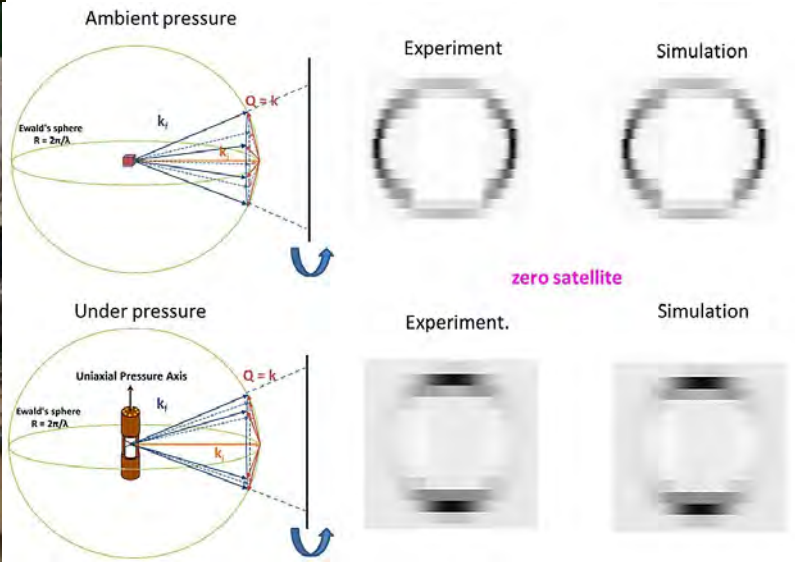


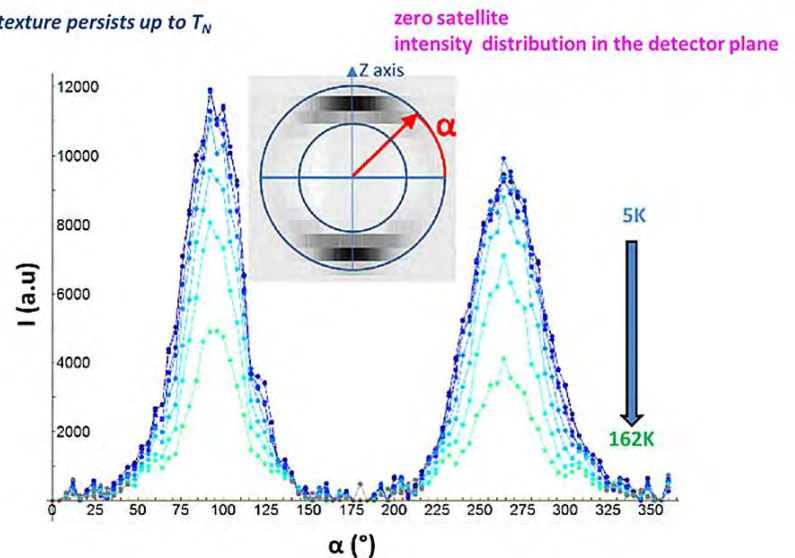
Figure 2 left: new 2D multidetector of G6.1 (LLB); right: scheme of the stress induced magnetic texture measured on G6.1

cell. Numerical simulations show that the great majority of the helices (typically above 95%) reorient along the pressure axis. This magnetic texture is independent on the value of the isotropic pressure and persists up to T_N .

zero temperature. However more complex spin structures, realizing a inhomogeneous fluctuating chiral phase [5] are clearly at play nearby T_N . They might play a role in the giant Topological Hall Effect, which changes sign with temperature.

The most natural explanation for the onset of this texture is the growth of magnetic helical domains within the ensemble of randomly oriented grains. Recalling that in MnGe the helical axes are oriented along $\langle 001 \rangle$ crystal axes, each grain can select the $[001]$ crystal axis as a preferential axis to minimize the magnetoelastic energy. This process is similar to the texture induced by a magnetic field, although in the heavily compressed sample the grain do not reorient. It frequently occurs in magnetic samples when a uniaxial pressure is applied below a magnetostructural transition.

The texture persists up to T_N



As a natural consequence our results [5] strongly suggest that the zero field zero pressure ground state is a multi-domain state, made of single-K helical domains, and not a complex multi-k structure made of skyrmion and anti-skyrmions lattices, where the selection of a single-K single domain would be energetically less favorable. Similarly in single crystals applying a uniaxial stress is a usual way to distinguish between single-k and multi-k spin structures.

Figure 3 : temperature dependence of the stress induced magnetic texture, measured on G6.1

This simple explanation may also account for the neutron scattering results under applied field, at least at

References

1. A. Fert *et al.* Nature Nanno. 8, 152, (2013)
2. O. Makarova *et al.* PRB 85, 205205, (2012)
3. N. Kanazawa *et al.* PRL 106, 156603 (2011)
4. N. Nagaosa and Y. Tokura, Nature Nanno 8, 899, (2013)
5. M. Deutsch *et al.* Phys. Rev. B 90, 144201, (2014)

ELECTRONIC PROPERTIES OF A DISTORTED KAGOME LATTICE ANTI-FERROMAGNET $Dy_3Ru_4Al_{12}$

D.I. Gorbunov^{a,b}, M.S. Henriques^{a,c}, A.V. Andreev^a, A. Gukasov^d, V. Petříček^a, N.V. Baranov^{e,f}, Y. Skourski^g, V. Eigner^a, M. Paukov^b, J. Prokleška^b, A.P. Gonçalves^c

a Institute of Physics - ASCR, Prague, Czech Republic

b Charles University in Prague, MFF, Department of Condensed Matter Physics, Prague, Czech Republic

c CCTN, IST/CFMUL, University of Lisbon, Lisbon, Portugal

d Laboratoire Léon Brillouin, CEA Saclay, DSM/IRAMIS, Gif-sur-Yvette, France

e Institute of Metal Physics - Ural Branch of Russian Academy of Sciences, Ekaterinburg, Russia

f Institute of Natural Science, Ural Federal University, Ekaterinburg, Russia

g Dresden High Magnetic Field Laboratory (HLD), Dresden, Germany

gorbunov@fzu.cz

Electronic properties of $Dy_3Ru_4Al_{12}$ (hexagonal crystal structure, Dy atoms form distorted kagome nets) are studied on a single crystal by means of magnetization, neutron diffraction, specific heat and resistivity measurements. The onset of a long-range magnetic order of Dy moments occurs at 7 K through a first-order phase transition. The compound has a non-collinear antiferromagnetic structure with a propagation vector $(1/2\ 0\ 1/2)$.

The configuration of the Dy moments is consistent with the monoclinic Shubnikov group C_2/c . In addition to the Dy contribution, spin fluctuations are induced in the 4d subsystem of Ru by the exchange field acting from the Dy 4f moments. In an applied magnetic field $Dy_3Ru_4Al_{12}$ displays magnetization jumps along all crystallographic directions.

A geometrical frustration often results in complex spin structures of solids due to the presence of conflicting interactions which separately favor different ground states. Recently, a $Dy_3Ru_4Al_{12}$ single crystal was grown the might display fingerprints of geometrical frustration. The compound crystallizes in the hexagonal crystal structure ($a = 8.774\ \text{\AA}$, $c = 9.530\ \text{\AA}$) of the $Gd_3Ru_4Al_{12}$ type (space group $P6_3/mmc$, two formula units per elementary cell) presented in Fig. 1a. Two types of layers perpendicular to the c axis can be distinguished. The layers containing Dy and Al atoms are planar, whereas those containing Ru and Al atoms are slightly puckered. The Dy atoms occupy one crystallographic site and form triangular nets parallel to the (ab) plane. The projection of the unit cell onto the (ab) plane shows that the Dy atoms are arranged in distorted kagome nets (Fig. 1b).

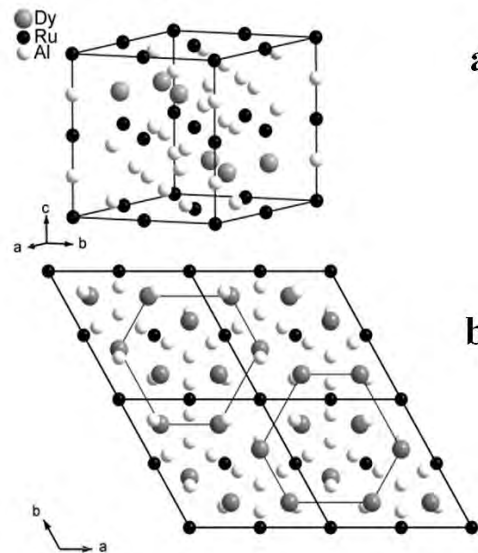


Figure 1 : Crystal structure of $Dy_3Ru_4Al_{12}$ (a) and its projection onto the (ab) plane (b).

a

b

$Dy_3Ru_4Al_{12}$ displays a long-range antiferromagnetic order below the Neel temperature, $T_N = 7\ \text{K}$ (inset in Fig. 2). A complex behavior of the magnetization was found in a magnetic field. Below 2 T along the c axis $Dy_3Ru_4Al_{12}$ displays two step-wise anomalies (Fig. 2a). Both field-induced magnetic transitions exhibit hysteresis and are of first order. The magnetization after the second transition, $\approx 22\ \mu_B/\text{f.u.}$, possibly reflects a non-collinear state of the magnetic moments.

This value is rather far from the forced ferromagnetic state (the magnetic moment of a Dy^{3+} ion is $10\ m_B$, which means that $Dy_3Ru_4Al_{12}$ should saturate at $30\ \mu_B/\text{f.u.}$). A hysteretic magnetization jump is observed along the basal plane of $Dy_3Ru_4Al_{12}$ as well (Fig. 2b). The different behavior of the magnetization along the basal plane and the c axis catches the strong magnetic anisotropy of $Dy_3Ru_4Al_{12}$.

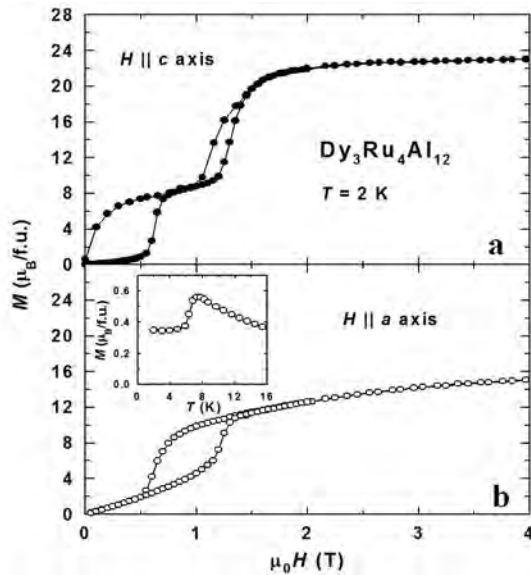


Figure 2 : Magnetization curves along the c (a) and a (b) axes of the $\text{Dy}_3\text{Ru}_4\text{Al}_{12}$ single crystal. The inset shows the temperature dependence of magnetization along the a axis in the vicinity of $T = T_N$.

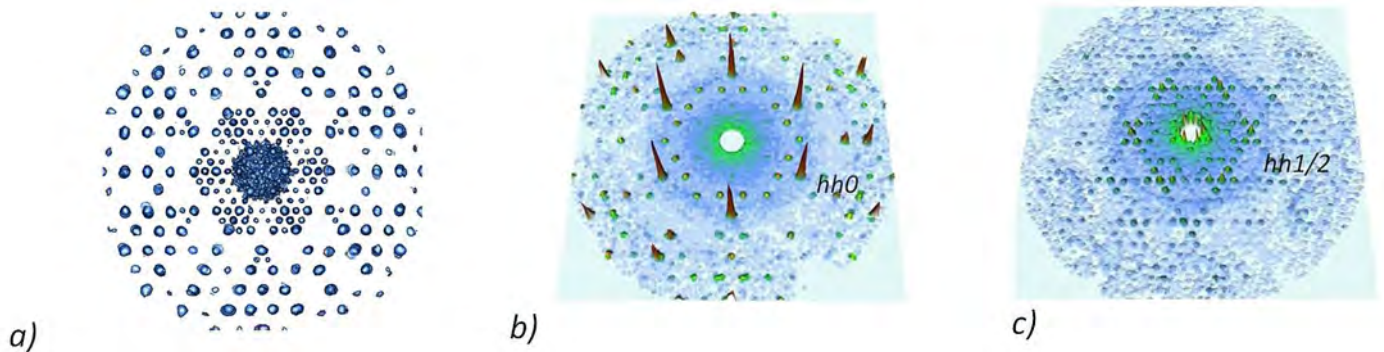


Figure 3 : (a) 3D equal intensity surfaces in the reciprocal space of $\text{Dy}_3\text{Ru}_4\text{Al}_{12}$ at $T = 1.5$ K. The reconstructed volume was completed with its symmetrically equivalent orientations employing the Laue symmetry of the structure. (b) Nuclear reflections in the $(hh0)$ plane and (c) magnetic satellites in the $(h h 1/2)$ plane $T = 1.5$ K

The field-induced magnetic transitions observed along the c axis and the basal plane reflect the intricate balance among the exchange interactions, magnetic anisotropy and Zeeman energy. In order to gain insight into the magnetic behavior of the compound, the knowledge of its magnetic structure in a zero field is essential. This prompted a single-crystal neutron-diffraction study of $\text{Dy}_3\text{Ru}_4\text{Al}_{12}$. A typical 3D representation of an equal scattering intensity surface at $T = 1.5$ K measured on **6T2** diffractometer is shown in Fig. 3a. From this pattern, a series of conventional 2D cuts (hhl) perpendicular to the $[001]$ axis were extracted, which showed the presence of magnetic satellites with propagation vector $\mathbf{k} = (1/2 0 1/2)$ and its equivalent ones. This can be seen from Figs. 3b and 3c, where the $(hh0)$ and $(h h 1/2)$ cuts are shown.

Thus, the study led to the determination of a non-collinear magnetic structure with a propagation vector $(1/2 0 1/2)$. The configuration of the Dy moments is consistent with the monoclinic Shubnikov group C_c2/c . The two corresponding magnetic space groups, C_c2/c and $C_c2/c+(0 0 1/4)$, differ in the origin position [1]. The resulting magnetic structure

models cannot be distinguished from the refinements as they give almost identical R-values. The two magnetic structures are compared in Fig. 4. For this figure we used an orthorhombic unit cell with parameters $a_0 = 8.740 \text{ \AA}$, $b_0 = 15.139 \text{ \AA}$ and $c_0 = 18.997 \text{ \AA}$ related to the original hexagonal basis by the equations $\mathbf{a}_0 = \mathbf{a}_H$, $\mathbf{b}_0 = \mathbf{a}_H + 2\mathbf{b}_H$, $\mathbf{c}_0 = 2\mathbf{c}_H$. In this setting the magnetic symmetries are alternatively described by the non-standard Shubnikov's symbols I_c2/c and $I_c2/c+(0 0 1/4)$. Each Dy atom carries an ordered magnetic moment M_{Dy} of about $10 \mu_B$ at $T = 1.5$ K. The largest component of M_{Dy} is projected onto the c axis. In the presented orthorhombic structure four layers of Dy atoms can be distinguished. To the left of Figs. 4a and b the net magnetic moments within each layer are shown. The total magnetic moment of the whole structure is zero, in accordance with the magnetization data indicating an antiferromagnetic ground state of $\text{Dy}_3\text{Ru}_4\text{Al}_{12}$ (Fig. 2).

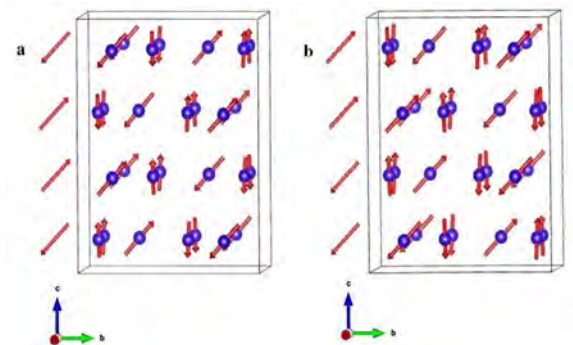


Figure 4 : Two possible magnetic structures of the $\text{Dy}_3\text{Ru}_4\text{Al}_{12}$ compound: (a) C_c2/c and (b) $C_c2/c+(0 0 1/4)$. For clarity only the Dy atoms are shown.

References

1. D.I. Gorbunov, M.S. Henriques, A.V. Andreev et al. Phys. Rev. B 90, 094405 (2014)

REVEALING MICROSCOPIC MAGNETIC INTERACTIONS IN BiFeO_3

J. Jeong^a, M. D. Le^a, P. Bourges^b, S. Petit^b, S. Furukawa^c,
S. A. Kim^d, S. Lee^d, S-W. Cheong^e, J. G. Park^a

^a Center for Correlated Electron Systems, Institute for Basic Science (IBS) and Department of Physics and Astronomy, Seoul National University, Seoul, Korea

^b Laboratoire Léon Brillouin, CEA-CNRS, CEA-Saclay, Gif-sur-Yvette, France

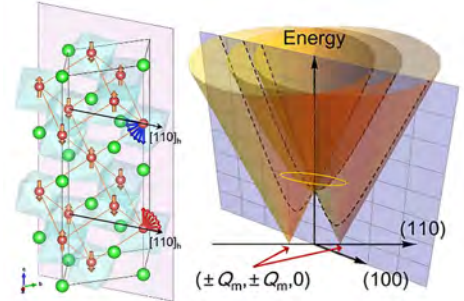
^c Department of Physics, University of Tokyo, Tokyo, Japan

^d Neutron Science Division, Korea Atomic Energy Research Institute, Daejeon, Korea

^e Rutgers Center for Emergent Materials and Department of Physics and Astronomy, Rutgers University, New Jersey, USA

hoho4@snu.ac.kr

Understanding the mechanism behind the indirect nature of the coupling between the magnetism and ferroelectricity in the room temperature multiferroic material BiFeO_3 demands a detailed knowledge of the microscopic interactions of each subsystem. In experiments at 4F2 at LLB we employed inelastic neutron scattering to determine the magnetic interactions from the low energy magnetic dynamics. Mapping these interactions as a function of temperature, and thus of changes in the atomic structure due to thermal expansion allows a qualitative un-



derstanding of how the structure modifies the magnetism, and hence a part of the magneto-electric coupling. Multiferroic materials combine separate but coupled order parameters in a single compound which offer the possibility to manipulate one order parameter with a 'force' that is usually associated with the other order parameter. For example, the magnetization (or

another magnetic property) of a magneto-electric multiferroic may, in principle, be altered by an applied electric field or voltage. This particular characteristic has attracted much attention due to the potential for applications in electronics. Moreover, the microscopic mechanism underlying this coupling between the two order parameters is also of fundamental interest.

While magnetoelectrics where an incommensurate magnetic structure breaks inversion symmetric and leads to ferroelectric ordering, called type II [1], show the strongest magneto-electric coupling, they have the disadvantage in that their ordering temperatures are in all cases far below the freezing point of nitrogen.

Type I multiferroics, such as BiFeO_3 , where the order parameters arise from unrelated mechanisms, have higher transition temperatures which in some cases are above room temperature. The drawback here is that the magneto-electric (ME) coupling is weak and indirect, but which has nonetheless been observed – for example in the switching of magnetic domains by an electric field [2], or in the enhancement of the electric polarisation below the magnetic ordering temperature [3].

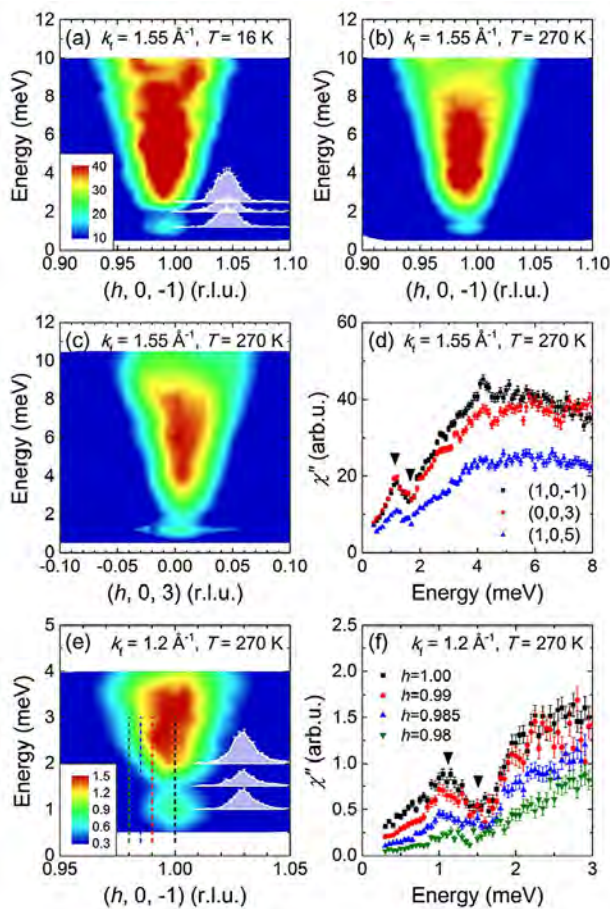


Figure 1 : Measured inelastic neutron scattering. There is an island of magnetic scattering centered at 1 meV which is indicative of competition between the DM interaction and single-ion anisotropy.

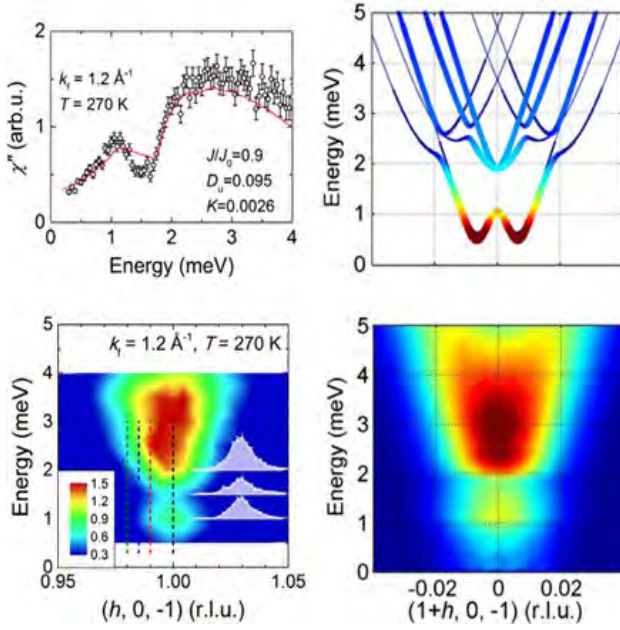


Figure 2 : Measured (left) and calculated (right) neutron inten-

In the recent work at LLB [4], we show that the low energy magnetic interactions, namely the Dzyaloshinskii-Moriya (DM) interaction and single-ion anisotropy (SIA), depend sensitively on the ionic positions, via their temperature dependence. One can thus expect that an electric field may also modify the ionic positions and hence alter the magnetic interactions and in this way affect the magnetic properties.

In detail, we observed an island of scattering centered at ≈ 1 meV at the magnetic zone center as shown in figures 1 and 2. This island is separated by a broader triangle of scattering at higher energies by a minimum in intensity (at ≈ 1.5 meV) which is due to a gap in the dispersion opened by the SIA. In particular, the inverted V-shaped peak and trough seen in the energy scan (fig 2) can only be explained by an easy-axis anisotropy term, as an easy-plane anisotropy produces a broader plateau with a smaller dip (see fig 2c of [4]).

This easy-axis SIA determines the energy difference between the peak and trough, whilst the DM interaction shifts both in energy, as it increases the splitting between formerly the degenerate phason and spin flip modes (see fig 3 of [4]). As the modes are close in energy and momentum transfer, they cannot be individually resolved by neutron spectroscopy but their convolution with the spectrometer's resolution function creates the island-like feature, and its evolution allows a determination of the DM interaction and SIA.

This is shown in figure 3 where we observed that the position of the island decreases slightly with increasing temperature, which implies a similarly slight decrease

of the DM interaction. This correlates well with the small observed change of the cycloid wavelength λ_{cycloid} measured by magnetic neutron diffraction. The dip shows a pronounced and non-monotonic change, from which we deduced that the SIA at first increases slightly before falling with increasing temperature. Finally, we found that the overall intensity of the scattering falls with temperature, which is mainly due to the reduction of the magnetic moment (fig. 3b, top) and does not reflect a change in the Heisenberg exchange.

The measurements thus show that both the SIA and DM interaction have strong effects on the low energy magnetic motions, and both depend sensitively on the ionic positions, which offers a mechanism for the ME coupling via the modification of the magnetic interactions due to shifts in the ionic positions caused by an applied magnetic field.

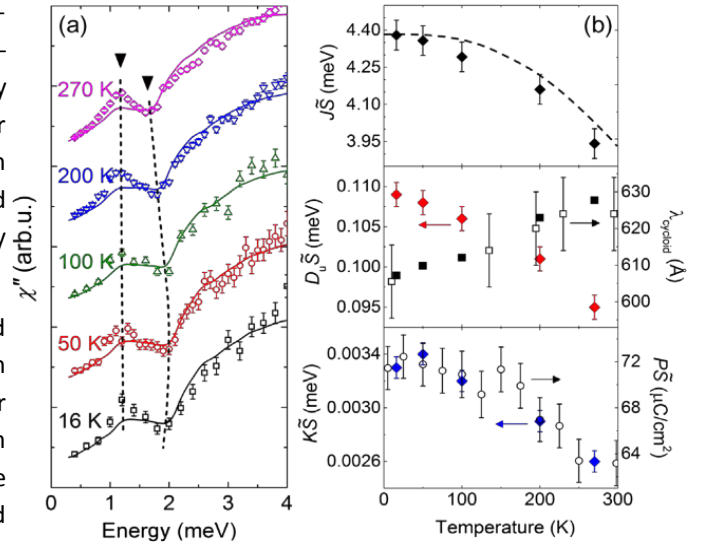


Figure 3 : Measured neutron energy scans as a function of temperature with the fitted χ'' (left) and the deduced temperature dependence (right) of the exchange, DM and SIA parameters together with related physical properties.

References

1. D. Khomskii, *Physics* 2, 20 (2009)
2. S. Lee *et al.*, *Phys. Rev. B* 78, 100101 (2008)
3. S. Lee *et al.*, *Phys. Rev. B* 88, 060103 (2013)
4. J. Jeong *et al.*, *Phys. Rev. Lett.* 113, 107202 (2014)

MAGNETIC NEUTRON SPECTROSCOPY OF A SPIN-TRANSITION Mn^{3+} MOLECULAR COMPLEX

K. Ridier^a, S. Petit^a, G. André^a, B. Gillon^a, G. Chaboussant^a, D. A. Safin^b, Y. Garcia^b

^a Laboratoire Léon Brillouin, UMR12 CEA-CNRS, F-91191 Gif-sur-Yvette, France

^b Institute of Condensed Matter and Nanosciences, Molecules, Solids, and Reactivity, Université Catholique de Louvain, Belgium

gregory.chaboussant@cea.fr

The mononuclear complex $[Mn^{3+}(pyrol)_3(tren)]$ both spin states provide a unique insight on the relationships between the zero-field split ground states and the local structural distortions

In molecular clusters containing transition-metal ions with $3d^4$ - $3d^7$ configurations in quasi-octahedral coordination, the application of an external stimulus (temperature, light, pressure, or magnetic field) may trigger a so-called spin transition (ST) between a low-spin (LS) and a high-spin (HS) state. If the right conditions (abruptness, presence of hysteresis, suitable temperature range) are met, this effect could be exploited for applications in the spintronics devices, molecular switches, and sensors. Indeed, along with the magnetic ground-state change, the ST is often accompanied by a change of volume through bond lengths variation, which has important effects in the optical, dielectric, structural, and even

local distortions of the coordination sphere induced by ST. This coupling determines to a large part the level of cooperativity and therefore the dynamics of the ST itself.

We report by zero-field inelastic neutron scattering (INS) a full insight of the magnetic ground states in both HS and LS states, of $[Mn^{3+}(pyrol)_3(tren)]$. More precisely, the HS and LS states' anisotropy parameters are determined at zero field and their relationships with local structural distortions away from purely octahedral geometry are discussed. We have taken advantage of magnetic neutron spectroscopy to address the relationships between the zero-field split ground states (both in LS and HS states) and the local structural distortions. We find that the HS state is indeed anisotropic, with a negative axial term, reflecting the spatial and temporal averaging of the Jahn-Teller trigonal distortions, and that the LS state is characterized by a strong positive axial anisotropy driven by an important trigonal compression.

Powder neutron diffraction was performed on the G4.1 diffractometer. Diffraction data also show the existence of a strong trigonal compression of the Mn^{3+} coordination environment, in both phases, along the C_3 axis. In Figure 1, we observe a sudden change of the powder neutron-diffraction pattern between 46 and 48 K. The sudden shift of Bragg peaks toward low Q upon warming indicates an increase of the lattice parameters and clearly signals the occurrence of an abrupt ST from the LS to the HS state. This shift, and the fact that no line broadening could be observed, show that the transition

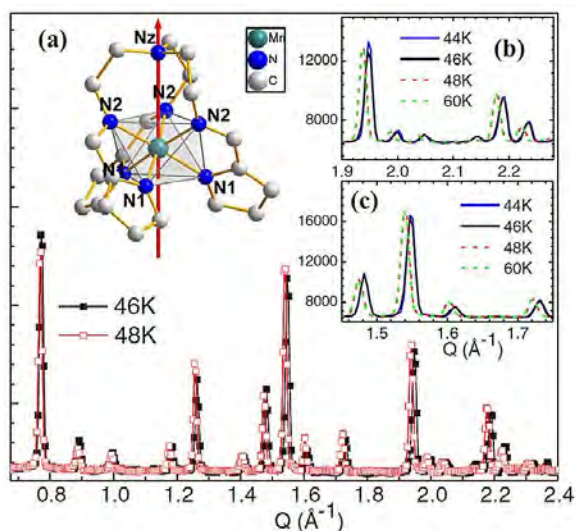


Figure 1 : Powder neutron diffraction ($\lambda = 2.4226 \text{ \AA}$, G4.1) across the ST at 46 and 48K and representation of the molecular unit. N atoms are labeled Nz , $N1$, and $N2$ depending on their coordination type. The red arrow represents the threefold axis of the molecule which also corresponds to a remarkable compression direction of the coordination octahedron.

mechanical properties. Spin transition is usually observed in octahedrally coordinated molecular complexes of Co^{2+} , Fe^{2+} , Fe^{3+} , and, more rarely, d^4 ions like Mn^{3+} and Cr^{2+} . The ST in $3d$ ions is governed by the competition between (a) the ligand field which splits the $3d$ levels into a lower t_{2g} triplet and an upper e_g doublet, enforcing electron pairing, and (b) the electronic intra-atomic Coulomb repulsion which promotes a HS ground state. Beyond this competition, the spin transition may also be influenced by a subtle interplay between intermolecular effects and

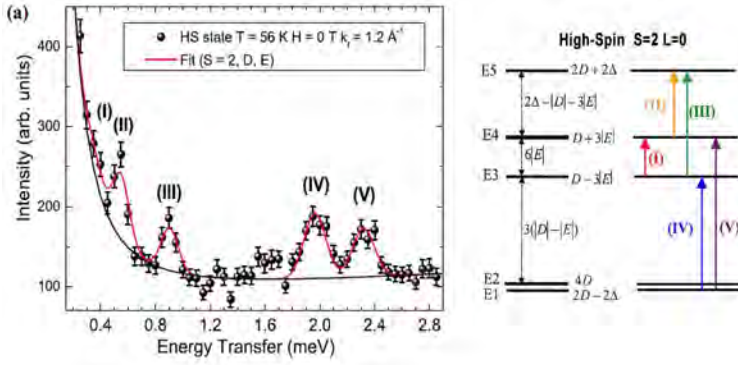


Figure 2 : (a) INS spectra of $[\text{Mn}^{3+}(\text{pyrol})_3(\text{tren})]$ obtained in the HS state ($S = 2$) at 56 K. Best fits to the data are represented as solid lines. (b) Energy diagram derived from the zero-field spin Hamiltonian (see Equation below) with $S=2$ and $D < 0$. The best agreement is obtained for $D = -0.711$ meV and $|E| = +0.059$ meV. Here : $D = (D^2 + 3E^2)^{1/2}$. The five observed transitions are shown in the far right panel.

is quasi complete (at least within the accuracy of neutron diffraction) and compatible with a highly cooperative process.

Figure 2 shows the magnetic excitation spectrum at 56 K in the HS state. Four transitions can clearly be observed between 0.5 and 2.5 meV, labeled II to V. The solid line is a global fit. The peak at 0.37 meV, labeled I, is merged into the elastic line and is therefore difficult to simulate, but it is fully accounted for in our simulations. In our model, the HS 5E ($L=0, S=2$) ground state is described using a spin-only Hamiltonian since no first-order orbital moment is operative:

$$\hat{H} = \hat{H}_{ZFS} + \hat{H}_{Ze} = D\hat{S}_z^2 + E(\hat{S}_x^2 - \hat{S}_y^2) + g\mu_B\vec{S}\vec{B}$$

where D and E are the axial and rhombic terms of the zero-field splitting (ZFS) and g is the Landé factor. The corresponding energy levels for $S = 2$ and $D < 0$ are schematically displayed in Figure 2. Best fits to the five INS peaks lead to $D = -0.711$ meV and $|E| = 0.059$ meV.

The INS data in the LS state are presented in Figure 3. There is only one single magnetic peak in the LS state situated at energy of about 4.87 meV. This is the only peak which disappears on crossing the LS-HS transition. The theoretical description of the LS 3T_1 state is more complex than for the HS 5E state due to the existence of an unquenched first-order orbital moment $L=1$ (see Ref [1]). The interplay of spin-orbit coupling and trigonal compression leads to an effective $S=1$ spin Hamiltonian split by a large positive single-ion anisotropy $D=+4.87$ meV (39cm^{-1}), in good agreement with both INS and susceptibility data.

If spectroscopic characterizations of the HS state have already been reported in various Mn^{3+} compounds, the observation and modeling of the LS 3T_1 state using a spectroscopic technique like INS have rarely been reported. The strong and positive trigonal ligand-field parameter D found in $[\text{Mn}^{3+}(\text{pyrol})_3(\text{tren})]$ in its LS state naturally leads to highly anisotropic magnetic properties, but further studies using polarized neutron diffraction will be most helpful to deepen our understanding of this material.

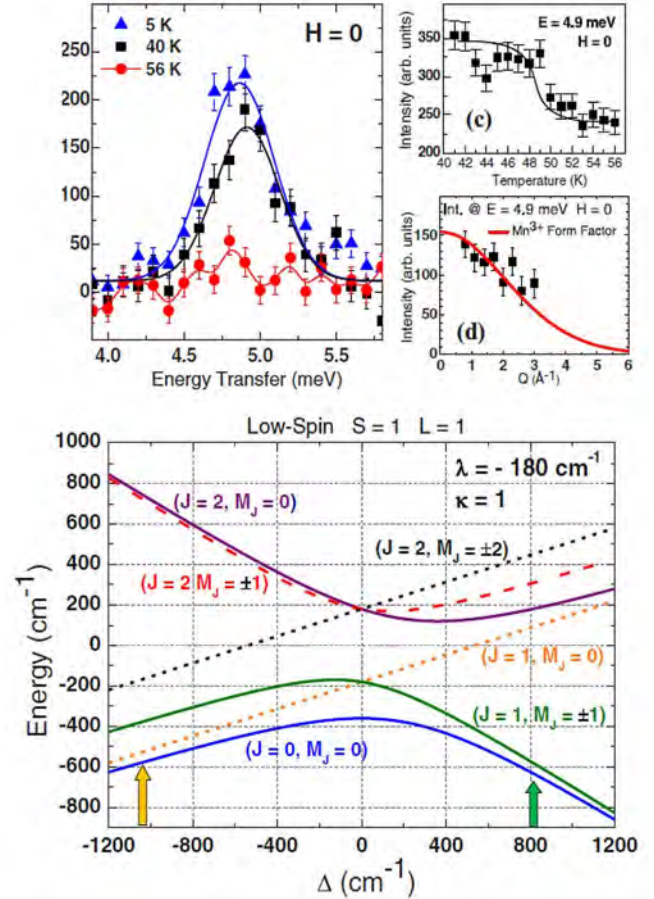


Figure 3 : Top: Temperature evolution of the LS magnetic peak [at 5 and 40 K] at zero field and compared to HS signal at 56 K. Bottom: Magnetic states energy diagram in the LS state ($S = 1$, $L = 1$) as a function of the trigonal distortion parameter D with orbital reduction factor $\kappa = 1$ and the SO coupling parameter $\lambda = -22.32$ meV (-180cm^{-1}) [1]. Arrows represent the two possible D values for which the energy of the first excitation matches the energy of the observed magnetic peak (C) at 4.87 meV (39cm^{-1}).

References

1. K. Ridier, S. Petit, B. Gillon, G. Chaboussant, D. A. Safin and Y. Garcia, Phys. Rev. B 90, 104407 (2014)

AXE 2:

Material and Nanosciences, Fundamental Studies and Applications

This scientific axis covers the activities related to the research in materials science and more generally in hetero-systems (i.e., interfaces, alloys, composite materials, and confined systems). The topics cover the study of the detailed structure of nano-objects, the interactions between nano-objects, the role of nanostructures in composite materials and the behavior of amorphous and glassy materials. LLB nanoscience research benefits from a variety of available neutron scattering techniques: SANS (Small Angle Neutron Scattering) - for studying the structure and organization of nanoparticles, Reflectivity - to study thin film structures (polymers, magnetic films, liquid surfaces), Diffraction - to study the crystalline or the magnetic order of nanostructures.

- **Ordered arrays of magnetic nanowires investigated by polarized small-angle neutron scattering**
T. Maurer, S. Gautrot, F. Ott, G. Chaboussant, F. Zighem, L. Cagnon, O. Fruchart
- **Influence of sulfur content on the Cube texture formation in FeNi alloys**
Y. Ateba Betanda, A. L. Helbert, F. Brisset, M. Wehbi, M.H. Mathon, T. Waeckerlé, T. Baudin
- ***Tuning of optical properties of cellulose nanofibril-based multilayered thin films through the Ionic-Strength controlled process of the architecture building***
F. Azzam, C. Moreau, F. Cousin, A. Menelle, H. Bizot, B. Cathala
- **Cations mobility within the porosity of faujasite-type zeolites: a combined in situ neutron diffraction and theoretical study**
W. Louisfrema, J.-L. Paillaud, P. Massiani, G. André, F. Porcher, B. Rotenberg, A. Boutin
- **The cork viewed from the inside**
A. Lagorce-Tachon, T. Karbowiak, C. Loupiac, A. Gaudry, F. Ott, C. Alba-Simionesco, R. D. Gougeon, V. Alcantara, D. Mannes, A. Kaestner, E. Lehmann, J. P. Bellat

ORDERED ARRAYS OF MAGNETIC NANOWIRES INVESTIGATED BY POLARIZED SMALL-ANGLE NEUTRON SCATTERING

T. Maurer^a, S. Gautrot^b, F. Ott^b and G. Chaboussant^b, F. Zighem^c, L. Cagnon^d

Polarized small-angle neutron scattering (PSANS) were performed on arrays of ferromagnetic Co nanowires ($\varphi \approx 13$ nm) embedded in self-organized alumina (Al_2O_3) porous matrices are reported. The triangular array of aligned nanowires is investigated as a function of the external magnetic field with a view to determine experimentally the real space magnetization $M(r)$ distribution inside the material during the magnetic hysteresis cycle. The observation of field-dependent SANS intensities allows us to characterize the influence of magnetostatic fields. The PSANS experimental data are compared to magnetostatic simulations. These results evidence that PSANS is a technique able to address real-space magnetization distributions in nanostructured magnetic systems. We show that beyond structural information (shape of the objects, two-dimensional organization) already accessible with non-polarized SANS, using polarized neutrons as the incident beam provides information on the magnetic form factor and stray fields $\mu_0 H_d$ distribution in between nanowires.

a Laboratoire de Nanotechnologie et d'Instrumentation Optique, Institut Technologique de Troyes.

b Laboratoire Léon Brillouin, CEA-CNRS, CEA-Saclay, Gif-sur-Yvette, France

c LSPM, Institut Galilée, CNRS et Université Paris-13, 93430 Villetaneuse, France

d Institut Néel, CNRS et Université Joseph Fourier, BP166, F-38042 Cedex 9 Grenoble, France

The structural, magnetic, and optical properties of nano-objects organized in periodic arrays have been intensively studied in recent years. Several converging lines of effort have greatly improved our knowledge of magnetic nano-objects over the last years. It started with the development of a wide range of systems, from dots to wires, with well controlled structural and magnetic features, and foreseen applications in medicine and magnetoelectronics. In this respect, "elongated" magnetic nano-objects in the form of nanowires (or nanorods) with very high aspect ratio (length/radius) have

emerged as some of the most promising materials due to several factors. First, synthesis improvements based on self-organization principles have made it possible to produce arrays of very high quality with narrow size distribution and two-dimensional (2D) organization in matrices. Second, the magnetic properties of ferromagnetic (FM) nanowires are essentially governed by their shape anisotropy, leading to large magnetic coercivity, and hence potential for electronic devices or high-density storage, and even high temperature permanent magnets.

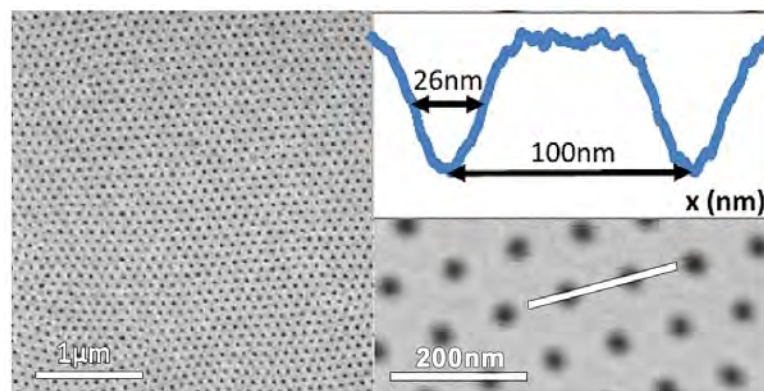


Fig. 1: SEM images of the porous alumina membrane used to produce the Co nanowires, and extraction by contrast image treatment of the depth profile of the pores as seen by SEM. The apparent average diameter is estimated to be around 26 nm, but the "surface" diameter is closer to 50 nm, reflecting both a potential conical shape of the pores and also a bias due to the techniques employed to extract the size (image contrast).

We have performed polarized small-angle neutron scattering (PSANS) on ordered arrays of Co magnetic nanowires. PSANS is a powerful but emerging technique which has only recently been used to investigate the magnetic configuration of nanoparticles. For instance, PSANS revealed chemically uniform, but magnetically distinct, core and canted shell in 9 nm magnetite particles.

Here, we show that PSANS is a tool to characterize, both structurally and magnetically, anisotropic magnetic nano-objects. With unpolarized neutrons, it is possible to disentangle the structure factor of the array and the nuclear form factor of a single wire. In previous studies, focused on Co and Ni nanowires ordered in Al₂O₃ membranes but with the external magnetic field applied perpendicular to the wire long axis, the variation of the SANS intensity depending on the applied magnetic field reveals that stray fields have to be taken into account in the magnetic form factor derivation.

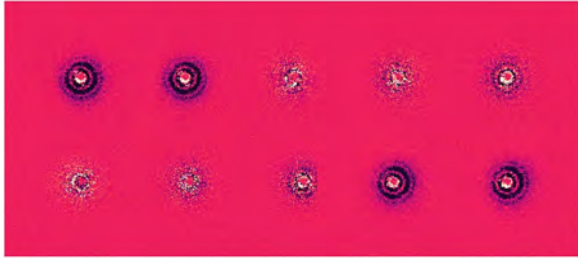


Fig. 2: 2D detector maps representing $I(q) = I+(q) - I-(q) \propto FM(q)$ at 200 K and for several magnetic fields $H_{parallel}$ to the long axis of the cobalt nanowires and to the incident beam direction.

In the polarized-neutrons case, we show that it is possible to derive directly from experiment the magnetic form factor, and therefore the magnetization distribution in the sample. We argue that it necessi-

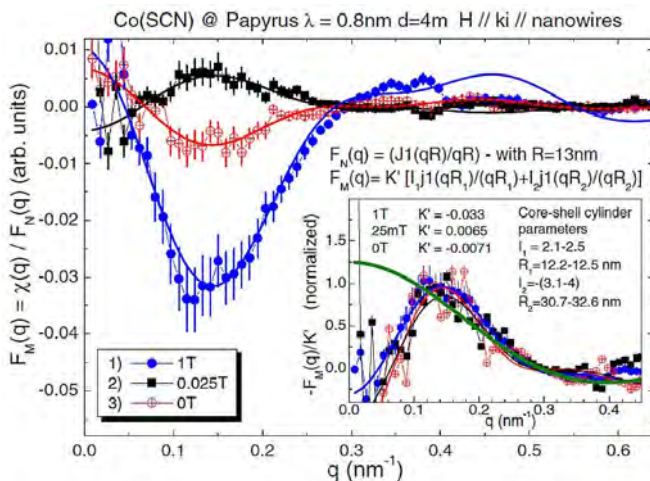


Fig. 3: Magnetic form factor $FM(q)$ of ferromagnetic Co nanowires for different longitudinal magnetic field fields: In chronological order (1) 1 T, (2) 25 mT, and (3) 0 T.

Solid lines are best fits using a core-shell cylinder model with the parameters $I_1 = 2.3 \pm 0.2$, $R_1 = 12.35 \pm 0.15$ nm, $I_2 = -3.6 \pm 0.5$, and $R_2 = 31.6 \pm 0.9$. Inset: $FM(q)$ normalized to unity (divided by K). The scaling parameter K' for each magnetic field is indicated. The green continuous line in the inset panel represents the expected magnetic form factor in the absence of a dipolar shell (i.e., with $I_2 = 0$).

tates the introduction of significant magnetostatic fields in between nanowires, whose effects are modeled using a straightforward core-shell model comprising (1) a core magnetic radius of induction close to the Co value and equal to the structural radius, and (2) a “dipolar shell” induction of constant but opposite amplitude surrounding the core induction. The evolution of these fields as a function of external magnetic field is also reported. Subtle inversion effects at very low fields due to the interplay of internal and external fields have been evidenced. We show that a magnetization “mapping” in such types of nano-objects is indeed possible using PSANS techniques and may easily be extended to further deposited nano-objects (dots, wires, etc.). Such type of studies indicates that PSANS is a promising technique able to provide information about complex magnetization in nano-objects.

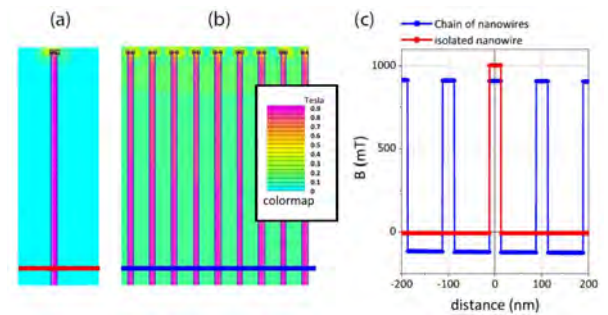


Fig. 4: (a) Dipolar fields generated by an individual nanowire with a diameter of 25 nm and a length of 5 μm .

(b) Dipolar fields generated for an assembly of nanowires and internanowire distance, center to center, of 100 nm.

(c) Profile of the induction for both situations, indicating that the dipolar fields are sizable in magnitude (with reversed sign) relative to the core induction. In the 2D triangular situation the effect is further enhanced.

References

1. T. Maurer, S. Gautrot, F. Ott, G. Chaboussant, F. Zighem, L. Cagnon and O. Fruchart, Phys. Rev. B 89, 184423, 2014

INFLUENCE OF SULFUR CONTENT ON THE CUBE TEXTURE FORMATION IN FeNi ALLOYS

Y. Ateba Betanda^a, A. L. Helbert^b, F. Brisset^a, M. Wehbi^a, M. H. Mathon^b, T. Waeckerlé^c, T. Baudin^a

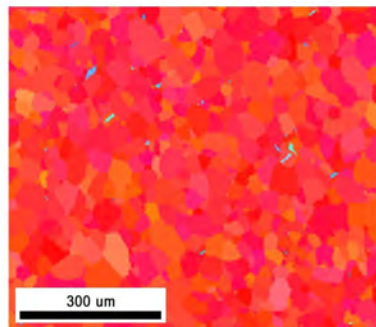
a ICMMO, Université Paris-Sud, Orsay, France

b Laboratoire Léon Brillouin, CEA-CNRS, CEA-Saclay, Gif-sur-Yvette, France

c Aperam alloys Imphy, Imphy, France

yanick.ateba-betanda@u-psud.fr

Hyper textured substrate tapes were prepared by cold rolling and annealing of a Fe48%Ni alloy in order to obtain Cube oriented substrates. The effect of sulfur content on the sharp Cube texture formation has been investigated. Results show that it is favored by the addition of sulfur. In order to explain this result, the stored energy has been measured from neutron diffraction peak broadening measurements on the cold-rolled states. The obtained values were compared to those determined from EBSD analysis (Dillamore and KAM approaches). It was shown that the stored energy calculated by both Dillamore and KAM approaches is underestimated compared to that calculated from neutron diffraction. To conclude, it appears that MnS precipitates are at the origin of hardening that increases the stored energy gap between the Cube orientation and the other ones when the sulfur content increases. This difference favors the Cube development.



High growths in the superconductor cable market allow opportunities to develop the research on metallic substrates with high Cube texture. The production of the superconductor wires needs epitaxial growth of YBCO superconductor on hyper textured Cube substrate [1]. Previous researches showed that Ni5%W is a good candidate for the substrate applications [2]. In order to obtain high critical current density in superconductor wire, it is necessary to produce up to 100% of Cube grains with low misorientation [3].

In order to reach this goal, Fe48%Ni alloys, which have the same mechanisms of Cube texture formation as Ni5%W alloys, have been used as model alloys. In the present work, the sulfur content (Table 1) effect on the Cube texture was studied [4].

Samples	S (ppm)
S-0	0
S-20	20
S-40	40
S-60	60

Table 1: Chemical composition of the studied samples

The Fe48%Ni alloys were prepared at Aperam alloys Imphy. After melting and bar casting, the alloys were hot-rolled to obtain 5mm thick tapes. After hot-rolling, the tapes were cold-rolled down to 50 μ m (thickness reduction of about 99%). The specimens were then annealed in vacuum atmosphere at 1000°C.

After cold rolling, the texture consists in a typical copper cold-rolled texture which main components are B {110} <112>, C {112}<111> and S {123}<634> ones. At this state, the Cube component acuity is very low.

After complete recrystallization, the volume fraction of Cube component was calculated from EBSD measurements. The fraction of grains having a deviation less than 10° from the exact Cube orientation {100}<001> increases as a function of sulfur content (Figure 1).



Figure 1: Fraction of Cube grains as a function of the sulfur content.

It is well known that the formation of Cube grains is favored by high stored energy difference between Cube grains and their neighbors: C, S and B grains [5]. Then, in order to obtain the stored energy of the main texture components after deformation, neutron diffraction measurements have been performed in the Laboratoire Léon Brillouin on the four circles diffractometer 6T1. For that, a pile up of sheet pieces was realized to obtain 1 cm³ cubic specimen.

The stored energy of cold-rolling components increases more or less when the sulfur content increases, except for the Cube component (Figure 2). The MnS formed in the presence of sulfur interact with dislocations and allow their multiplication. Then, the stored energy increases with high accumulation of dislocations in the presence of MnS.

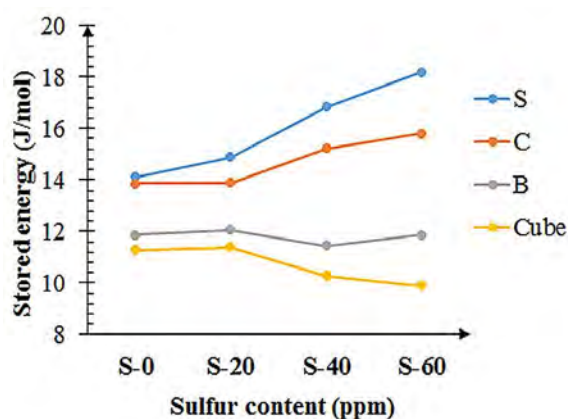


Figure 2: Stored energy (J/mol) associated to B, C, S and Cube orientations as a function of sulfur content.

Let us note that the stored energy of Cube grains remains quasi constant whatever the S amount. It seems that the effect of MnS is negligible on the hardening of this component whereas it hardens the other ones. This may be due to the lower number of slip systems activated in the Cube orientation. Then, the increase of stored energy difference between the Cube orientation and the other components when adding sulfur promotes the Cube texture development.

This stored energy evolution estimated from neutron diffraction measurements based on the peak broadening was also compared to those estimated from EBSD measurements i.e. the Kernel Average misorientation (KAM) and the Dillamore methods both based on the misorientation and dislocation cell size estimation [6]. The results were compared with each other and it was demonstrated that the stored energy calculated by both KAM and Dillamore approaches is underestimated compared to that one calculated from neutron diffraction peak broadening (Figure 3). This is because Dilla-

more approach considers only the GND (Geometrically Necessary Dislocations), blocked in the cell walls, the KAM method takes into account only the GND in all of the microstructure (cells and walls) and the neutron diffraction method takes into consideration all types of dislocations (SSD (Statistically Stored Dislocations) and GND) within the microstructure.

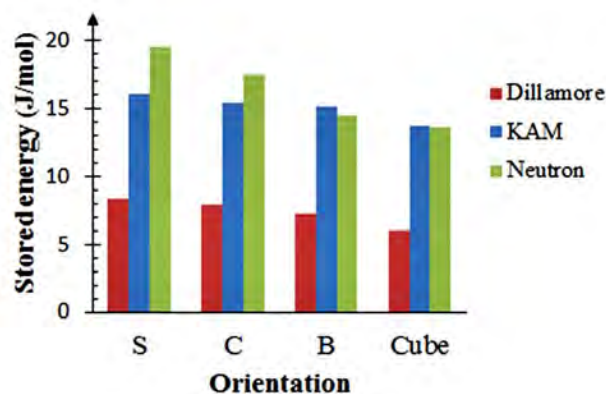


Figure 3: Comparison of stored energy of S, C, B and Cube components in the deformed state of the S-40 sample, calculated by the three approaches.

To conclude, the effect of sulfur on the formation of Cube texture in the Fe48%Ni alloys has been investigated. It appears that the MnS precipitates favor the accumulation of dislocations by an Orowan strengthening mechanism and lead to an enhanced stored energy in the samples. The stored energy gap between the Cube orientation and the other texture components, increases with the sulfur content and promotes the Cube nucleation and growth during primary recrystallization [4].

References

1. F. A. List, A. Goyal, M. Paranthaman, D. P. Norton, E. D. Specht, D. F. Lee, D. Kroeger, *Physica C* 302 (1998) 87-92
2. A.O Ijaduola, J.R. Thompson, A. Goyal C.L.H. Thieme, K. Marken, *Physica C* 403 (2004) 163-171
3. S. I. Kim, D. M. Feldmann, D. T. Verebelyi, C. Thieme, X. Li, A. A. Polyanskii, D. C. Larbalestier, *Phys. Rev. B* 71, 104501 (2005) 1-9
4. Y. Ateba Betanda, A.L. Helbert, F. Brisset, M. Wehbi, M.H. Mathon, T. Waeckerlé and T. Baudin, *Advanced Engineering Materials*, 16 (2014) 933-939
5. A.L. Etter, M.-H. Mathon, V. Branger, T. Baudin, R. Penelle, *Scripta Mater*, 46 (2002) 311-317
6. Y. Ateba Betanda, A.L. Helbert, F. Brisset, M.H. Mathon, T. Waeckerlé and T. Baudin, *Materials Science and Engineering A*, 614 (2014) 193-198

TUNING OF OPTICAL PROPERTIES OF CELLULOSE NANOFIBRIL-BASED MULTILAYERED THIN FILMS THROUGH THE IONIC-STRENGTH CONTROLLED PROCESS OF THE ARCHITECTURE BUILDING

F. Azzam^a, C. Moreau^a, F. Cousin^b, A. Menelle^b, H. Bizot^a, B. Cathala^a

Cellulose nanofibrils (CNF) and synthetic poly(allylamine) hydrochloride (PAH) were used to build multilayered thin films via the dipping-assisted layer-by-layer technique. We used the ionic strength, in both CNF suspension and PAH solution, as a key parameter to control the inner structure of the films, which was derived by neutron reflectivity. Distinct architectures were obtained, with various porosity and swelling ratios. In turn, this control of the inner architecture enabled to tune the optical properties and, in particular, their antireflective character.

^a UR1268 Biopolymères Interactions Assemblages, INRA, 44316 Nantes, France

^b Laboratoire Léon Brillouin, CEA-CNRS, CEA-Saclay, Gif-sur-Yvette, France

firas.azzam@nantes.inra.fr
bernard.cathala@nantes.inra.fr

Owing to the current environmental concerns, new strategies in materials science are underway for the design of new innovative materials based on natural and renewable bioresource-based objects. In this context, cellulose nanofibers (CNF), i.e. crystalline wires with a nanometric section, are very attractive building blocks to produce high performance nanomaterials with bottom-up approaches because they have amazing properties such as low density, high aspect ratio and very high Young modulus [1]. In the past decade, they have been increasingly used for the design of nanostructured thin film via the so-called layer-by-layer (LbL) approach [2]. This technique involves depositing alternating layers of two nano-objects that present attractive interactions on a substrate (by processes such as dipping, spraying, spin-coating..), each layer enabling to anchor the

following one in order to form the whole thin film. Originally developed with nano-objects interacting through electrostatic interactions, the LbL concept has been extended so system interacting through hydrogen bonding, hydrophobic interactions, covalent linkages, etc... the strength and/or nature of interactions enabling to tune the architecture in the thin films.

Aiming at obtaining CNF-based thin film with tuneable optical properties, we have used the LbL concept with dipping to make films of negatively charged CNF (of cross section of 3–4 nm and a length of approximately 0.5–1 μm) “glued” by positively charged objects, namely flexible polyelectrolyte chains of poly(allylamine hydrochloride) (PAH) [3]. As the driving force for complexation is electrostatics, the main lever to tune interaction is the ionic strength of the mother stock solutions of both objects to be dipped. We have thus compared three situations: (i) films made without added salt (called (PAH 0 M–CNF 0 mM) n where n is the number of cycles of dipping one layer of and one layer of CNF), (ii) films made with 1M salt within the PAH solution (called (PAH 1 M–CNF 0 mM) n and iii) films made with salt within the CNF solution (called (PAH 0 M–CNF i mM) n) where i is the ionic strength of the PAH solution).

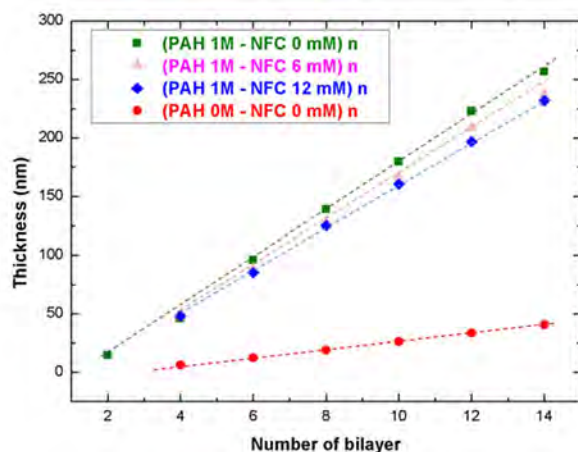


Figure 1 : Thickness of thin films measured by ellipsometry vs number of bilayers deposited.

The first step was to follow the thickness of the thin layer versus the number of desposition cycles by ellipsometry. As

shown by Figure 1, the growth of thin films was linear in all cases, but the thicknesses were much smaller in absence of salt, demonstrating immediately the central role played by salt in the deposition process.

In order to go further on the understanding of the deposition process, the refined inner architecture of thin films was determined by neutron reflectometry thanks to measurements done both at the air/solid interface (Fig 2.a) and at the solid/water interface (Fig 2.b). This enabled to determine the thickness and swelling properties of the layers, and more interestingly the porosity of the layer thanks to an original method detailed in ref [3]. Finally, the SLD profiles revealed very different structures of the

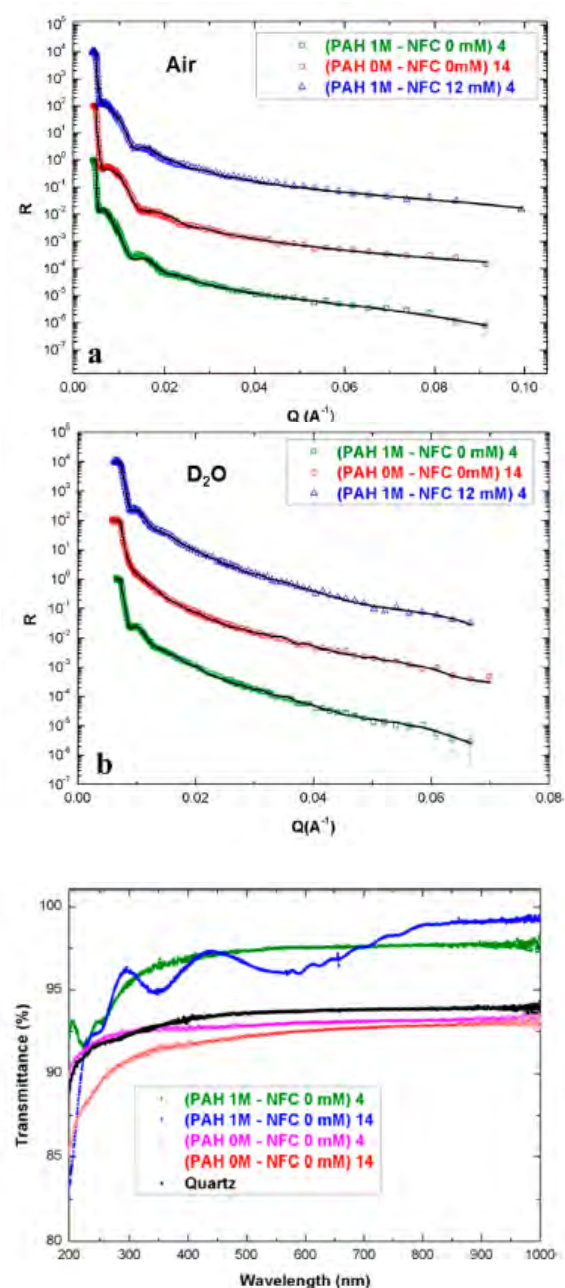


Figure 2 : (a) NR measurements at the air/solid interface; (b) NR measurements as the air/D₂O interface; (c) UV-vis light transmittance measurements

layers despite overall very close thickness, as depicted in Figure 3, which are mainly driven by the PAH conformation in the deposit solution.

Indeed, with salt-free PAH solution where chains have extended conformation, the resulting films have lower porosity and higher swelling ratios, compared to the ones made using high ionic strength (1 M) PAH solution, where chains have a coiled conformation.

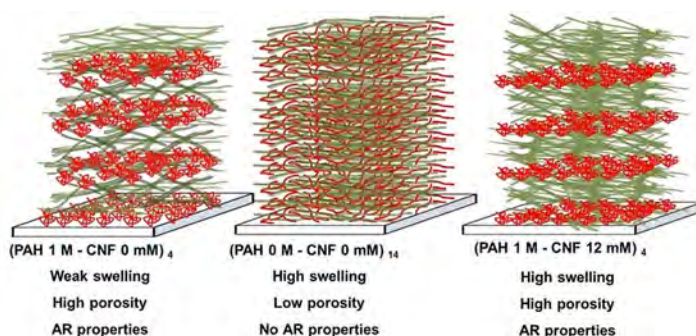


Figure 3 : Illustration of the different (PAH-CNF) film architectures, as derived from NR measurements.

Finally, the porosity and respective ratio of cellulose to PAH in the final structure, which in turn change the optical refractive indexes of the layers. This ultimately enables to tune the antireflective properties of the thin layer, as films made devoid of salt show antireflective properties, while films made with added salt, either in the PAH solution or in the CNF solution do show antireflective properties, as shown on UV-vis light transmittance measurements (Figure 2.c).

References

1. Y.Habibi, L. A.Lucia,; O. J. Rojas, Chem. Rev. 2010, 110, 3479–3500.
2. G. Decher, Science 1997, 277, 1232–1237
3. F. Azzam, C. Moreau, F. Cousin, A. Menelle, H. Bizot, B. Cathala, Langmuir, 2014, 30(27), 8091-8100

CATIONS MOBILITY WITHIN THE POROSITY OF FAUJASITE-TYPE ZEOLITES: A COMBINED IN SITU NEUTRON DIFFRACTION AND THEORETICAL STUDY

W. Louisfrema^{a,b}, J.-L. Paillaud^c, P. Massiani^d, G. André^e, F. Porcher^e, B. Rotenberg^b, A. Boutin^a

a Pasteur, UMR 8640 CNRS, Paris, France

b Phenix, UMR 8234 CNRS, Paris, France

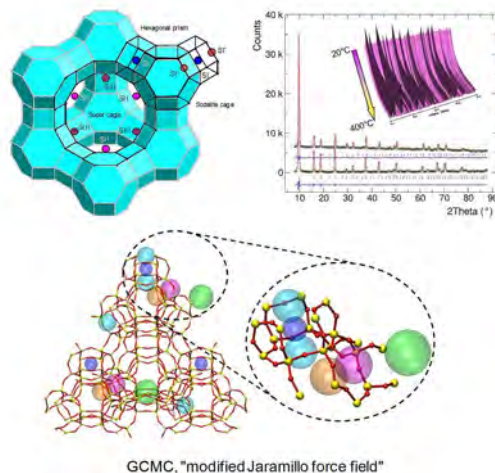
c IS2M, UMR 7361 CNRS, Mulhouse, France

d LRS, UMR 7197 CNRS, Paris, France

e Laboratoire Léon Brillouin, CEA-CNRS, CEA-Saclay, Gif-sur-Yvette, France

wilfried.louisfrema@ens.fr

The distribution and mobility of Na⁺ cations inside the pores of a Y faujasite zeolite (Si/Al molar ratio of 2.31, 58 Na⁺ per unit cell) has been followed upon dehydration by in situ powder neutron diffraction (PND). The experimental results are compared to those given by a new theoretical approach. The predicted cation distribution is excellent at high temperature but some differences are observed below 150°C. Molecular simulations show that these differences discrepancies owe to the presence of water molecules rather than to the temperature and adsorption-induced deformation of the mineral framework.



represented in Fig. 1a. Under normal conditions of temperature and pressure, faujasites are able to adsorb up to 30 weight % of water, i.e. about 250 molecules per unit cell. These water molecules coordinate the cations and induce their displacements in the voids.

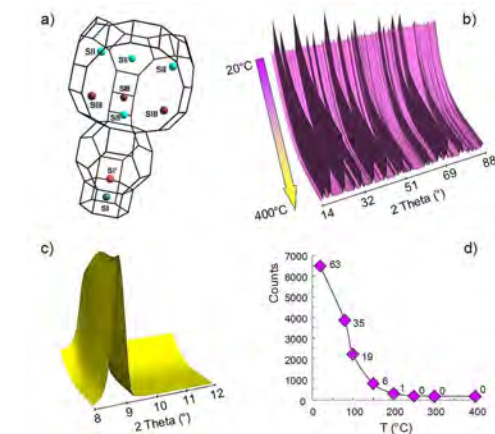


Fig. 1: a) Extra-framework cationic sites in faujasite-type zeolite (bridging oxygen atoms have been omitted for clarity). Evolution as a function of temperature of b) PND patterns of Na₅₈Y collected under vacuum on the G4.1 diffractometer ($\lambda=2.423$ Å) and c) 111 line profile and d) incoherent signal intensity decrease (at each point, the number of water molecules per U.C. determined from TGA is also indicated).

Zeolites are crystalline microporous aluminosilicates which are important materials in industry, especially in gas adsorption or separation and in catalytic processes. In order to counterbalance the negative charge of the frameworks, zeolites contain compensating cations in their pores. Since the location of these extra-framework cations plays an essential role in adsorption properties, the precise determination of cation location has been the subject of many experimental and theoretical studies [1]. In the specific case of cubic faujasite structures, the cations are placed on the four “standard” crystallographic sites called I, I', II and III [1] schematically

Neutron powder patterns of highly crystalline Na₅₈Y faujasite were recorded during heating under vacuum on the G4.1 diffractometer (Fig. 1b). These latter clearly show an increase of the intensity of the 111 diffraction line, sensitive to disordered extra-framework species (Fig. 1c) together with a lattice expansion upon heating, the a lattice parameter varying from 24.679(1) Å at 20°C to 24.834(1) Å at 400°C.

The changes in peak intensities are concomitant with water molecules removal (dehydration process) as can be deduced from the progressive decrease in the intensity of the incoherent signal (3D representa-

tion, Fig. 1b) caused by the ^1H atoms of the hydration water molecules present in the sample (Fig. 1c). This decrease allows us to quantify the water content, and its thermal evolution which is in good agreement with estimates obtained from thermogravimetric analysis (TGA, numbers reported in Fig. 1d). After an initial partial dehydration, the initial water content is 8 wt. %, or ~ 63 water molecules per unit cell (U.C.), i.e. about 1 molecule per cation. Next, dehydration in vacuum takes place regularly between RT and 150°C and is almost complete at 200°C (Fig. 1d). The residual amount of water per U.C. at 150°C is 0.8 wt. %, i.e. about 1 water molecules.

Rietveld refinements (Fig. 2) allowed us to locate the

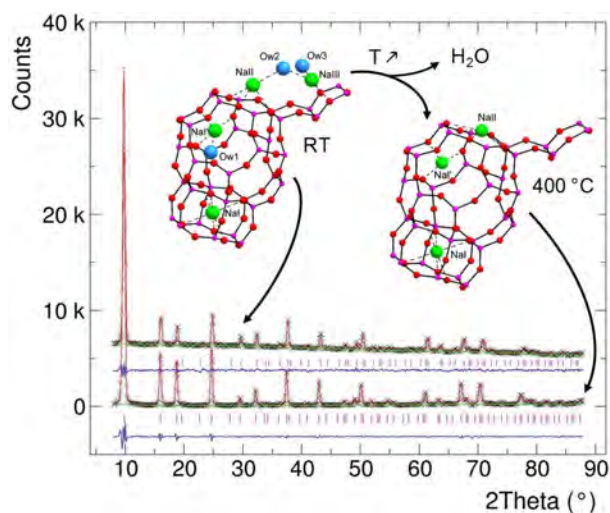


Fig. 2: Rietveld plots of Na_{58}Y before and after dehydration at 400°C under vacuum, experimental (x), calculated (solid red lines) and background (solid green lines). Vertical magenta ticks are the positions of theoretical reflections for $\text{Fd}3\text{m}$ space group. Solid blue lines are the difference plots. The insets show perspective views of the corresponding structures.

water molecules and cations over the entire temperature range, i.e. along dehydration steps. As expected for this zeolite structure, four distinct crystallographic extra framework cationic sites are found with positions consistent with published studies on faujasite with similar Si/Al ratios [1].

Fig. 3 presents the evolution of cationic site occupancies versus temperature. After evacuation at room temperature, sites III are predominantly occupied (Fig. 2). During the successive heating steps from RT until 150°C , a continuous migration of sodium cations from predominantly sites III toward sites II occurs (Fig. 2). At this temperature, i.e. after an almost complete removal of the water molecules, the site distribution stays constant with a full occupancy of site II, i.e. 32 Na^+ per U.C.

In order to investigate the cationic migration from a molecular point of view, we also performed Monte Carlo simulations. To that end, we introduced a new localization procedure, allowing for the assignment of each cation to a specific type of site from its local environment that is characterized by different types of framework oxygen atoms. This new procedure does not require the knowledge of the atomic coordinates of the sites and is particularly well suited to account for flexible or rigid frameworks [3].

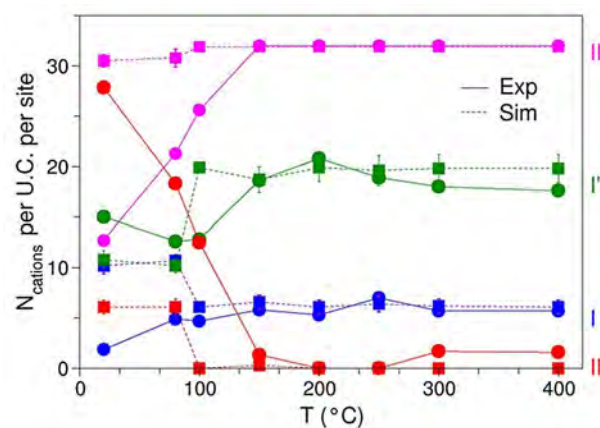


Fig. 3: Number of sodium cations per U.C. in each cationic site type (I, I', II and III) versus temperature. Experimental data are compared to Monte Carlo simulations.

While a quantitative agreement with experiments for high temperatures is found, when the water content is low, some important differences are observed for temperatures lower than 100°C when the amount of adsorbed water molecules increases. In particular the simulations predict a migration from sites I' to III. Simulations using a modified Jaramillo force field [4] with increased cation-water interactions provide results in better agreement with the experiments. Finally, the present study suggests that the development of refined force fields, better taking into account the balance between ion-water and ion-framework interactions as well as framework plasticity, is highly attractive [3].

References

1. Frising T., Leflaive P., *Microporous Mesoporous Mater.* 114, 27–63, (2008)
2. Noack M. *et al.*, *Microporous Mesoporous Mater.* 117, 10–21, (2009)
3. Louisfremea W. *et al.*, *Mol. Simul.* doi: 10.1080/08927022.2015.1027889. (2015)
4. Jaramillo E., Auerbach S.M., *J. Phys. Chem. B* 103, 9589–9594, (1999)

WL acknowledges financial support from Région Ile-de-France and the DIM OXYMORE

THE CORK VIEWED FROM THE INSIDE

A. Lagorce-Tachon^{a,b}, T. Karbowiak^a, C. Loupiac^{a,e}, A. Gaudry^e, F. Ott^e, C. Alba-Simionesco^e,
R. D. Gougeon^{a,b}, V. Alcantara^d, D. Mannes^d, A. Kaestner^d, E. Lehmann^d, J.-P. Bellat^b

a Univ Bourgogne, AgroSup
Dijon, PAM, Equipe PAPC,
UMR A 02 102,
21078 Dijon, France

b Univ Bourgogne, Inst Univ
Vigne & Vin,
21078 Dijon, France

c IS2M, UMR 7361 CNRS,
Mulhouse, France

d Paul Scherrer Inst,
5232 Villigen, Switzerland

e Laboratoire Léon Brillouin,
CEA-CNRS, CEA-Saclay, Gif-sur-
Yvette, France

thomas.karbowiak@u-bourgogne.fr

Cork is the natural material stripped from the outer bark of cork oak. It is still the most used stopper to seal wine bottles and to preserve wine during storage. Cork stoppers are sorted in different classes according to apparent defects, named lenticels, which can be related to the cork macroporosity. The more lenticels there are, the worst cork quality is. The present work aims at investigating defects analysis of cork stoppers from two classes by comparing images recorded by digital photography and neutron imaging.

Cork was one of the first materials put under the microscope. The first depiction dates back to the years 1660, when Robert Hooke drew the scheme of its very characteristic cellular organization, giving the term cell to the basic biological unit (Hooke, 1664). More recently, Gibson et al. (1981) described the geometry of cork cells in three different sections: axial, radial and tangential (Fig. 1).

Cork is generally sorted visually by hand or by optical analysis as a function of its overall outside general aspect, considering the defects viewed from the outside are a good estimation of the inside. Some other technics such as X-ray or Terahertz imaging were recently used to get a better understanding of the inner structure of cork samples or to perform 3D reconstructed images by tomogra-

phy. Neutron imaging is another non-destructive and non-invasive method which allows characterizing materials structure and defects at the microscopic length scale. Whereas light can only probe the inside of transparent materials, neutrons penetrate most materials to depths of several centimeters. The hydrogen nucleus scatters neutrons strongly.

Cork stoppers are graded in different classes. Generally there are 7 or 8 qualities, but there is no well-defined standard. Class 0 represents the best quality while 6 or 7 (depending on the classification used) is the poorest. The aim of this study is to identify and quantify defects present in different classes of cork stoppers with two techniques: digital photography and neutron imaging (radiography and tomography).

The neutron radiography experiments were performed on the new cold neutron imaging station (IMAGINE) at the Laboratoire Léon Brillouin. Exposure time was 7s by image and an average of 32 images was performed to increase the quality of the image. The image size was 2048x2048 pixels.

The neutron tomography experiments were performed on the thermal neutron imaging station NEUTRA at the Paul Scherrer Institute.

Two pictures of cork wafers from class 4 and 0 are shown in Fig. 2a and d. In this axial view of cork, lenticels appear as vertical lines, being most often of around 1 mm thick. The selected samples presented here

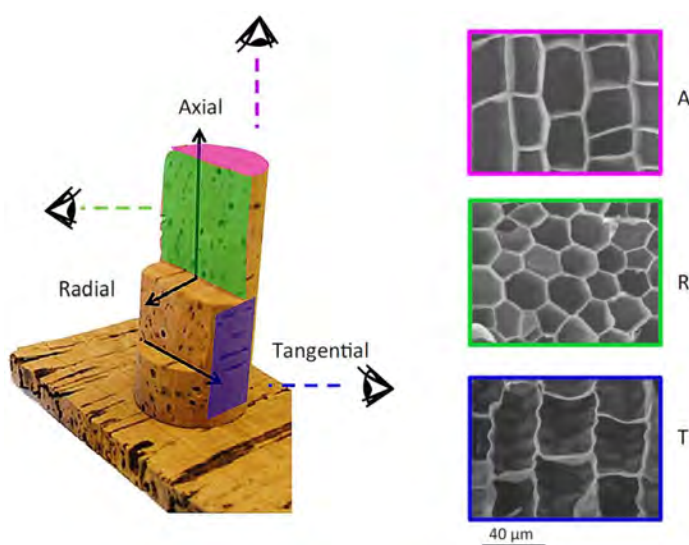


Fig. 1: Cork seen from the three directions, with the three corresponding scanning electronic microscopy pictures of the axial (A), radial (R) and tangential (T) sections.

in Fig. 2 have 3.5% and 6.8% surface defects for class 0 and class 4, respectively, which corresponds to mean values observed for these two classes. The surface image analysis was applied to all of the cork stoppers chosen for this study: the 12 wafers from 12 different stoppers and the 12 wafers from a single stopper, for each of the two classes 0 and 4, so in total four different series.

Neutron radiographs of two different cork wafers are shown in Fig. 2, with the corresponding photographs. Neutron radiographies are greyscale images. Sample attenuation is almost directly proportional to the quantity of hydrogenated matter in which neutrons went through. The denser is the material, the higher is the grey value. As a consequence, denser parts of the material appear darker on the radiograph and, obviously, holes are brighter. Two parameters influence the neutron attenuation absorption by the sample: on the one side the chemical composition and, on the other side,

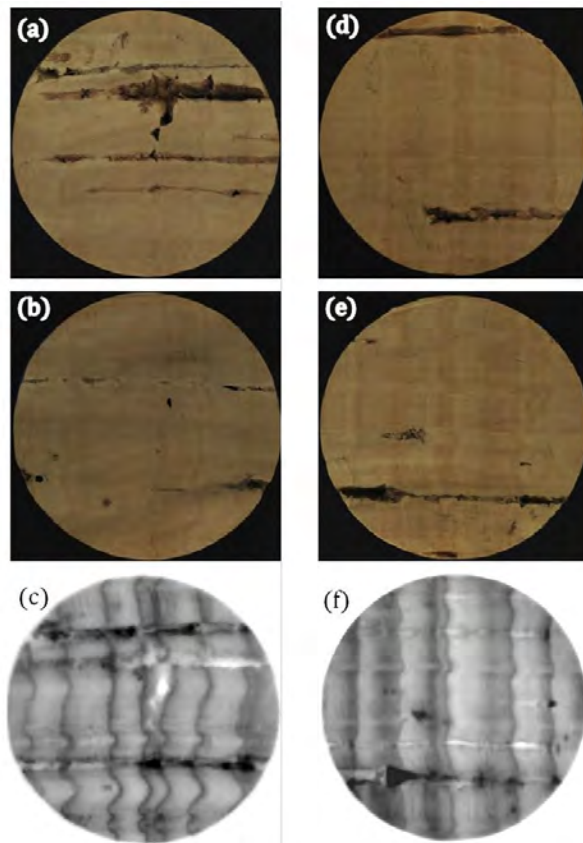


Fig. 2: Neutron radiographs of 3 mm cork wafers of 24 mm diameter (c and f) with the corresponding pictures viewed from both sides (a & b and d & e, respectively). a & b: both sides of a class 0 (3.5% and 3.1% surface defects, respectively); c: neutron radiograph of the same class 0 (2.7% volume defects); d & e: both sides of a class 4 (6.8% and 1.4%, surface defects, respectively); f: neutron radiograph of the same class 4 (2.6% volume defects).

the thickness of the sample. In our case, the thickness is the same along the whole wafer (except if considering defects as voids), so the chemical composition is the main factor which affects the neutron attenuation. Fig. 2f shows different attenuation levels depending on the type of defect. As an example, the lenticel visible in Fig. 4e at the bottom left, appears on the radiography as a darker and thus denser area (Fig. 2f). Also, in Fig. 4d, there is a lenticel on the right side, which appears as a bright tube on the corresponding radiograph (Fig. 2f). It is moreover noticeable that there is a denser area in the material at the edge of lenticels. Noteworthy is the number of lenticels in this radiograph: around 6 lenticels can be seen on it whereas only 2 are visible on the photograph. This clearly shows that all these defects cannot be revealed by a simple analysis with digital photography even if the sample is as thin as 3 mm.

In most of cases, the neutron radiography or the neutron tomography take more defects into account than the photography analysis. Comparing the two qualities of stoppers, photography analysis and neutron tomography permit to differentiate these classes: around 4.1% and 5.9% of defects for class 0 stoppers, and 6.7% and 7.5% for class 4 stoppers, respectively. A more detailed statistical analysis of the data can be found in reference (A. Lagorce-Tachon, 2015). Furthermore, tomography also allowed observing defects distribution along the whole stopper and possible interconnectivity. Lenticels in a cork stopper are in a great majority not interconnected. It is also worthy to note that the inter-individual variability from stoppers to stoppers is as important as the intra variability within a single stopper. The next step to this work will consist in bridging the gap between structure investigated by imaging and functional properties of cork.

References

1. "The cork viewed from the inside"
Aurélie Lagorce-Tachon, Thomas Karbowiak, Camille Loupiac, Alexandre Gaudry, Frédéric Ott, Christiane Alba-Simionesco, Régis D. Gougeon, Valentin Alcantara, David Mannes, Anders Kaestner, Eberhard Lehmann, Jean-Pierre Bellat
Journal of Food Engineering, 149 (2015,) 214.

AXE 3 :

Soft Matter and Biophysics.

The third axis “Soft Matter and Biophysics” deals with systems made of individual building blocks (colloidal nanoparticles, polymers, surfactants, proteins and phospholipids) whose characteristic sizes lay in the 0.1–10 nm range. In such systems, the delicate balance of interactions (of the order of $k_B T$) can lead to the formation of large self-assembled complex architectures showing specific dynamics, kinetics or lifetime. Understanding the underlying mechanisms of their self-assembly and dynamics is then the key to control and tune the very specific properties of inert, functional or biological matter at the nanometer scale (1-100 nm). In this framework, the neutron scattering techniques combined with H/D isotopic labeling are a unique tool to characterize the systems at the relevant spatial and temporal scales of the systems. In particular, they make it possible to get a refined picture of the behavior of either the building blocks in specific physicochemical conditions such as polyelectrolytes in the high concentration regime (Lorchat et al), bare charged nanoparticles stabilized in ionic liquid (Mamusa et al), biopolymers chains in presence of divalent cations (Assifaoui et al), or to evidence the formation of original self-assembled architectures such as nanoribbons in green biosurfactants systems (Cuvier et al) or nanodomains in hybrid polymer/lipid vesicles (Tuyen Dao et al).

- **Orientation order in polyelectrolyte solutions**

P. Lorchat, I. Konko, J. Combet, J. Jestin, A. Johner, A. Laschewski, S. Obukhov, M. Rawiso

- **Phase separation and nanodomains formation in hybrid polymer/lipid vesicles**

T. P. Tuyen Dao, F. Fernandes, M. Er-Rafik, R. Salva, M. Schmutz, A. Brûlet, M. Prieto, O. Sandre, J.-F. Le Meinsa

- **pH-triggered formation of nanoribbons from yeast-derived glycolipid biosurfactants**

A-S. Cuvier, J. Berton, C. Stevens, G. C. Fadda, F. Babonneau, I. N. A. Van Bogaert, W. Soetaer, G. Pehau-Arnaudet, N. Baccile

- **Tuning the colloidal stability in ionic liquids by controlling the nanoparticles/liquid interface**

M. Mamusa, J. Siriex-Plénet, F. Cousin, E. Dubois, V. Peyre

- **Gelation of pectin in presence of divalent cations: a revisited mechanism**

A. Assifaoui, A. Lerbret, H. T. D. Uyen, F. Neiers, O. Chambin, C. Loupiac, F. Cousin

ORIENTATION ORDER IN POLYELECTROLYTE SOLUTIONS

P. Lorchat^{a,b}, I. Konko^a, J. Combet^a, J. Jestin^c, A. Johner^a, A. Laschewski^d, S. Obukhov^e, M. Rawiso^a

a Institut Charles Sadron (CNRS-UdS), Strasbourg, France

b University of North Carolina at Chapel Hill, Chapel Hill, NC, USA

c Laboratoire Léon Brillouin, CEA-CNRS, CEA-Saclay, Gif-sur-Yvette, France

d Fraunhofer Institut für Angewandte Polymerforschung, Postam, Germany

e Department of physics, University of Florida, Gainesville, FL, USA

michel.rawiso@ics-cnrs.unistra.fr

The question was raised if an orientation order could be observed in semi-flexible polyelectrolyte solutions¹⁻³. Small angle X-ray and neutron scattering experiments recently performed on dense solutions of highly charged polyelectrolytes allow replying to this issue. Specifically, they reveal the existence of a nematic local order at high concentration⁴ preceded by a new regime⁵, both depending on the intrinsic stiffness of the macroion and the ionic strength of the solution.

We combined small angle X-ray and neutron scattering (SAXS and SANS) techniques for investigating the structure of dense polyelectrolyte solutions. The main idea was that the intrinsic stiffness of polyelectrolyte should play a role. A major experimental result is that the scattered intensity from a salt-free polyelectrolyte solution displays a broad maximum for some scattering vector q^* depending on concentration c ⁶. The shift with concentration of this polyelectrolyte peak is the signature of the various concentration regimes^{1,7}. In the framework of the isotropic model, we have for highly charged polyelectrolytes in good solvent: $q^* \sim c^{1/3}$ in the dilute regime; $q^* \sim c^{1/2}$ in the semidilute regime; $q^* \sim c^{1/4}$ in the concentrated regime. This sequence of scaling laws [$c^{1/3}$; $c^{1/2}$; $c^{1/4}$] was observed from SAXS experiments on salt-free aqueous solutions of sodium poly(styrene sulfonate) (NaPSS)⁸. At higher concentration ($c > 4$ M), a peak of another nature, strongly shifted with respect to that of the concentrated regime and not related to the electrostatic interaction, was also revealed. Its position does no longer vary with concentration ($q^* \sim c^0$) suggesting an "ionomer" regime compatible with the existence of some clusters resulting from attractive interaction between dipoles. Indeed, a decrease in the dielectric constant is expected close to the bulk state. None translational or rotational order was observed in the salt-free aqueous so-

lutions of NaPSS. That is not surprising since NaPSS is a flexible polyelectrolyte with a small non-electrostatic persistence length ($l_p = 10\text{\AA}$). It was therefore natural to look for an Onsager transition to a nematic phase⁴ by considering polyelectrolytes of higher intrinsic stiffness, like poly(diallyldimethyl ammonium chloride) (PDADMAC, $l_p = 30\text{\AA}$) and sodium hyaluronate (HA, $l_p = 70\text{\AA}$) of different Mw. SAXS (ICS Strasbourg) and SANS experiments (PAXE) from the salt-free aqueous solutions of these semi-flexible polyelectrolytes lead to a new sequence of scaling laws: [$c^{1/2}$; $c^{1/4}$; c^1 ; $c^{1/2}$] and to new regimes, with exponents 1 and $1/2$, at high concentration⁵.

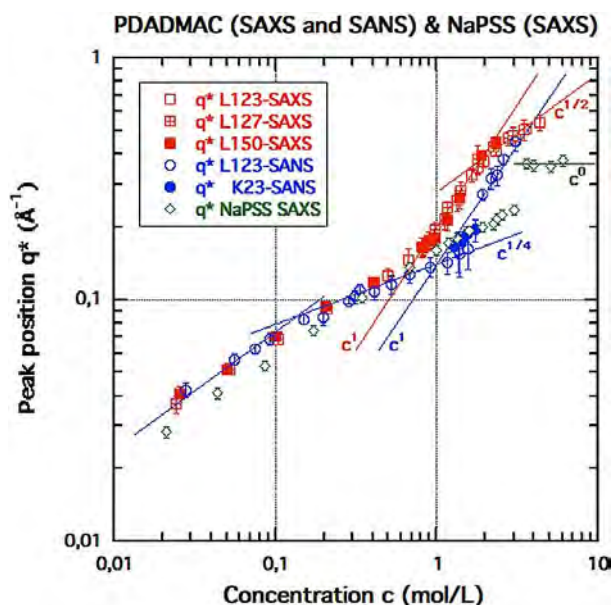


Figure 1: q^* versus c from both SAXS measurements on salt-free aqueous solutions of PDADMAC (L123, L127 and L150, which have distinct molecular weights) or NaPSS and SANS measurements on salt-free aqueous solutions of PDADMAC

For highly charged PE solutions, the scattered intensity $I(q)$ (cm^{-1}) containing all the structural information involves three partial scattering functions:

$$I(q) = K_m^2 S_{mm}(q) + K_c^2 S_{cc}(q) + 2K_m K_c S_{mc}(q)$$

In this relation, m refers to the monomers of the macroions; c , to the counterions; K_m and K_c , to their respective contrast lengths with respect to the solvent (H_2O or D_2O). For HA, all the counterions are free in the solution, as the effective charge fraction (according to the Manning-Oosawa counterion condensation process ($f_{\text{eff}} = 1$) and, whatever the incident radiation, the scattered intensity is reduced to $K_m^2 S_{mm}(q)$. For NaPSS and PDADMAC ($f_{\text{eff}} = 0.33$ and 0.66), $I(q)$ corresponds mainly to $K_m^2 S_{mm}(q)$ for SANS because the counterions (Na^+ and Cl^-) are hydrophilic but the three partial functions have to be taken into account for SAXS. All the scattered intensities $I(q)$ show a broad maximum at scattering vector q^* that shifts to higher q values as concentration increases. The indexations of the maxima (q^* versus c), as obtained from SAXS or SANS for NaPSS or PDADMAC, are shown in Figure 1.

The existence of a linear relationship for the c -dependences of q^* ($q^* \sim c$) from SANS and SAXS experiments performed with PDADMAC in a concentration range beyond 1 M is remarkable. This regime is not expected from the existing theory and already performed experiments. Moreover, it is not observed with NaPSS, as already shown⁸. However, it is confirmed

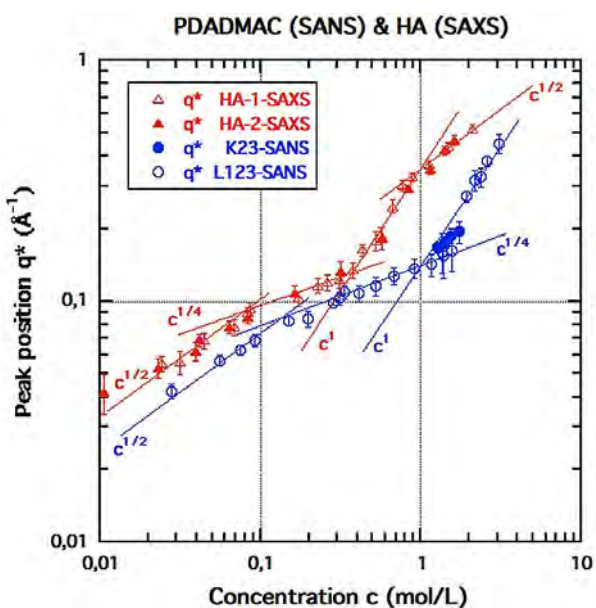


Figure 2: q^* versus c from both SANS measurements on salt-free aqueous solutions of PDADMAC and SAXS measurements on salt-free aqueous solutions of HA. In both cases, q^* corresponds to the maximum of the scattering function of macroions.

with HA, another semi-flexible macroion with a higher intrinsic persistence length (Figure 2).

Thus, the new regime appears in dense polyelectrolyte solutions, above the so-called concentrated regime, only for polyelectrolytes with intermediate intrinsic stiffness ($l_p \sim 30\text{--}90 \text{ \AA}$). The next regime, associated with the scaling law $q^* \sim c^{1/2}$, is ascribed to a nematic local order predicted by theory^{2,3}, as for rigid polyelectrolytes. It is specifically favored at the expense of the new one as the presence of added salt increases the ionic strength. The new concentration regime, observed for dense salt-free aqueous solutions of various polyelectrolytes, is quite original. It is provided by the large enough intrinsic stiffness of macroions and corresponds to a jammed random close packing of equivalent solid rods with a length comparable to the intrinsic persistence length⁵. In Figure 2, the difference in q^* for PDADMA and HA is thus comparable to the one in the non-electrostatic persistence length. However, the new regime is absent for aqueous solutions of short rigid polyelectrolytes as DNA strands that only display an Onsager (first order) transition between isotropic and nematic phases.

In Figure 1, we note the difference between SANS and SAXS data in the new regime. Such unusual influence of the contrast on intermolecular correlations actually is resulted from the change in the excluded volume, or correlation hole, when we are going from macroions to condensed counterions. The excluded volume is reduced for condensed counterions, which are more mobile than macroions. The related q^* values are therefore higher for the same concentration when the contribution of counterions to the scattered intensity is increased. That is the case for SAXS.

References

- 1 P.-G. de Gennes *et al.*, *J. Phys. (France)* 37, 1461 (1976)
- 2 I. A. Nyrkova *et al.*, *Macromol. Theory Simul.* 6, 965 (1997)
- 3 G. A. Carri *et al.*, *J. Chem. Phys.* 111, 1765 (1999); K. Gosh *et al.* *J. Chem. Phys.* 116, 5299 (2002)
- 4 L. Onsager, *ANN. N.Y. Acad. Sci.* 51, 637 (1949)
- 5 P. Lorchat *et al.*, *EPL* 106, 28003 (2014)
- 6 J.-P. Cotton *et al.*, *J. Phys. Lett.* 37, L-75 (1976); M. Nierlich *et al.*, *J. Phys. (France)* 40, 701 (1979)
- 7 J.-L. Barrat, J.-F. Joanny, *Adv. Chem. Phys.* 100, 909 (1996); V. Dobrynin, M. Rubinstein, *Prog. Polym. Sci.* 30, 1049 (2005)
- 8 K. Kaji *et al.*, 49, 993 (1988); K. Nishida *et al.*, *J. Chem. Phys.* 114, 8671 (2001)

PHASE SEPARATION AND NANODOMAINS FORMATION IN HYBRID POLYMER/LIPID VESICLES

T. P. Tuyen Dao^{ab}, F. Fernandes^b, M. Er-Rafik^c, R. Salva^a, M. Schmutz^c, A. Brûlet^d, M. Prieto^b, O. Sandre^a, J.-F. Le Meins^a

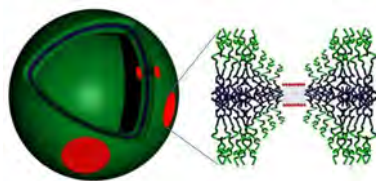
a LCPO, Pessac, France

b CQF IST, Lisbonne, Portugal

c ICS, Strasbourg, France

d Laboratoire Léon Brillouin, CEA-CNRS, CEA-Saclay, Gif-sur-Yvette, France

lemeins@enscbp.fr



Hybrid polymer/lipid large unilamellar vesicles (LUVs) were studied by Small Angle Neutron Scattering. Evidence of nanometric phase separation in hybrid vesicles was demonstrated for the first time using appropriate D₂O/H₂O mixture of solvents in order to separate the contributions to the scattering of lipids and of copolymers. These results were supported by data of other techniques like time-resolved Förster resonance energy transfer and cryo-transmission electron microscopy.¹

Hybrid vesicles resulting from the combined self-assembly of amphiphilic copolymers and lipids have attracted particular interest of chemists and (bio)physicists over the last five years.² Such assemblies are viewed as advanced vesicular structures compared to their liposome and polymeric forerunners, as the advantages of the two compounds can be integrated in single hybrid vesicles. Hybrid giant unilamellar vesicles (GUVs) with different degrees of membrane structuration (heterogeneous membrane presenting lipid nano- or micro-domains) were obtained by adjusting the lipid fluidity (T_m) with copolymers of membrane thickness close to the one of liposomes. Here, we show that stable hybrid LUVs can be obtained with stable nanodomains enriched either in lipid or in polymer. Although biophysical mechanisms that prevent ripening of small lipid domains in a membrane involve several parameters and are not yet completely understood, we decided to minimize the line tension, which naturally arises from the thickness mismatch between the lipid domains and the surrounding polymer membrane. Indeed, this parameter has been shown to play a role in the membrane structuration of giant hybrid vesicles.^{3,4} So, we first selected a close to matching system. We have used a commercial grafted copolymer with a flexible poly-(dimethylsiloxane) backbone and two poly(ethylene oxide) pendant moieties (PDMS-*g*-PEO)₂ of $M_w = 3000$ g/mol. This copolymer is well-known to form vesicles and the membrane thickness (~ 5 nm⁵) is close to that of liposomes (~ 3 – 4 nm).

It was mixed with deuterated 1,2-dipalmitoyl-sn-glycero-3-phosphocholine DPPC_{d62} at about 80/20 in polymer/lipid weight ratio. For the same composition in giant unilamellar vesicles, phase-

separation with micrometer-size lipid domains was observed by fluorescence microscopy.³ The present study was performed with lipid either in a fluid state (46°C) or in the gel state (20°C).

The hybrid samples were prepared by film rehydration in D₂O/H₂O mixtures, with subsequent filter extrusion at 100 nm pore size. A mixture at 0.09/0.91 D₂O/H₂O (volume ratio) was used to match the scattering length density (SLD) of PDMS and detect only the deuterated lipid phase, at a concentration of 5 mg/mL of DPPC_{d62}. Using a sufficient weight concentration (5 mg/mL) of deuterated lipid (thus 19 mg/mL of polymer), the lipid signal went well above the incoherent background of the mixture of solvent. A mixture of D₂O/H₂O at volume ratio 0.81/0.19 was used to observe only the polymer phase, at 5 mg/mL of PDMS-*g*-(PEO)₂. Pure D₂O was used to observe similar sample made with PDMS-*g*-(PEO)₂/DPPC in the non matching condition. Prior Light Scattering measurements have shown that the scattering objects had a narrow size distribution and a hydrodynamic radius in agreement with the extrusion process as illustrated in figure 1. The hybrid character of the vesicles was shown by Flow cytometry and Zeta potential measurements (results not shown here).

The SANS experiments were carried out on the PACE and PAXY spectrometers. Three configurations were used to cover a broad q range from 2.4×10^{-3} to 0.37 \AA^{-1} , well suited to the determination of LUVs dimensions. In the figure 2 are represented the

curves for the polymer matching (lipid phase visible) and no matching conditions (signal of whole vesicle) at 20°C and 46°C.

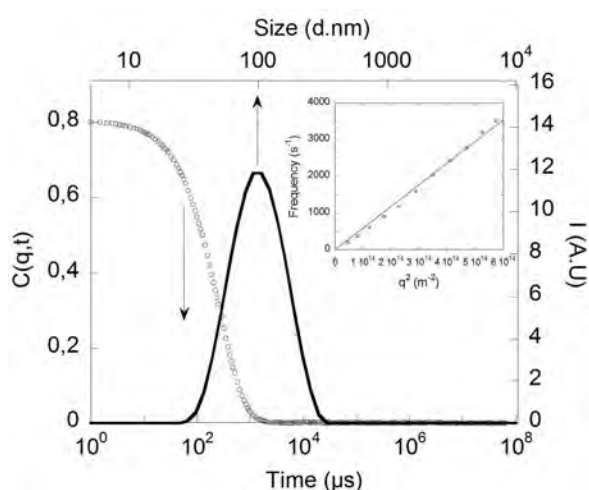


Figure 1: Light scattering autocorrelation function at 90° and time distribution function by CONTIN analysis (multi-modal relaxation) for PDMS-g-(PEO)₂/DPPC (80/20 wt.) vesicles. Inset: Relaxation rate vs q^2 .

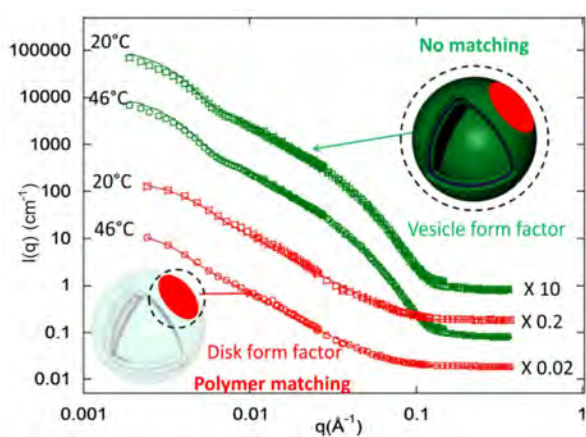


Figure 2: SANS data of PDMS-g-(PEO)₂/DPPC₆₆₂ (80/20 wt. ratio) hybrid vesicles in polymer matching condition and of PDMS-g-(PEO)₂/DPPC in no matching condition at 20°C and 46°C. Solid lines: fitting curves with disk or vesicle form factors.

Interestingly, the curves obtained in polymer matching condition could not be fitted with the vesicle form factor commonly used to model pure lipid or pure polymer vesicles, but they were well fitted with a polydisperse flat cylinder (disk-like) form factor. Conversely, the curves measured in the no matching condition could be fitted with a vesicle form factor, attesting the vesicular structure of hybrid objects.

The fitting values of radius (R_{cyl}) and height (L_{cyl}) reported in Table 1 suggest that lipid phase presents disk-like shapes, both at 20°C and 46°C, whose thicknesses ~3.3nm well correspond to the one of a pure lipid bilayer. Radius of gyration (R_g) and membrane thicknesses (δ) were also estimated using Guinier and Kratky–Porod plots ($\ln(q^2 I(q))$ versus q^2), respectively.

Disk radii calculated from the independently measured values of R_g and δ through the equation $R_g^2 = R_{cyl}^2/2 + \delta^2/12$ are in good agreement with disk radii obtained using the disk form factor fit. It is interesting to note that the lipid/polymer volume ratio estimated geometrically is $(\pi R_{cyl}^2 \times L_{cyl}) / (4\pi R_g^2 \times \delta) = 0.18$ at 20°C and 0.28 at 46°C, thus, not too different from the experimental mass ratio (0.20). In lipid matching condition, (not shown here) data could not be precisely fitted with either a cylinder or a vesicle form factor: this again was proving the hybrid character of copolymer/lipid vesicles.

In this first work on hybrid lipid/polymer vesicles¹, we have proven the existence of domains of lipids inside the hybrid polymer/lipid vesicular structure resulting from a phase separation inside the membrane. These nanodomains are stable in opposition to hybrid GUVs of same composition which were unstable and susceptible to fissions. This difference is suggesting the peculiar role of the curvature on the stabilization of these nanodomains.

	$R_{cyl} \pm \sigma_R$, or $R_{ves} \pm \sigma_R$ (nm)	R_g (nm Guinier plot)	Cylinder $L_{cyl} \pm \sigma_L$ or shell thickness δ (nm)	Membrane thickness (nm Kratky – Porod plot)
Polymer matching 20°C	54±9	35	3.4±0.7	3.4
Polymer matching 46°C	73±7	43	3.1±0.9	3.3
No matching 20°C	30±17	52	5.1±1.2	5.8
No matching 46°C	37±14	54	5.1±1.2	5.6

Table 1: Characteristic parameters of PDMS-g-(PEO)₂/DPPC hybrid vesicles in polymer matching and no matching conditions at 20°C and 46°C.

A more systematic study is currently under progress to assess the effects of composition, of lipid fluidity, of molar mass and of the architecture of copolymer on the membrane structuration of hybrid LUVs. We are developing a holey shell form factor to fit the scattering curves and better characterize the number and the sizes of nanodomains in these hybrid vesicles.

References

- 1 T.P. Tuyen Dao *et al.*, ACS Macro Lett. **2015**, 4(1) 182.
- 2 J-F. Le Meins *et al.*, Mat. Today **2013**, 16(10) 397.
- 3 M. Chemin *et al.*, Soft Matter **2012**, 8(10) 2867.
- 4 M. Schultz *et al.*, Soft Matter **2014**, 10, 831.
- 5 R. Salva *et al.*, ACS Nano **2013**, 7, 9298.

PH-TRIGGERED FORMATION OF NANORIBBONS FROM YEAST-DERIVED GLYCOLIPID BIOSURFACTANTS

A-S.Cuvier^{a,b,c}, J. Berton^d, C. Stevens^d, G.C. Fadda^e, F. Babonneau^{a,b,c}, I.N.A. Van Bogaert^f, W. Soetaer^f, G. Pehau-Arnaudet^g, N. Baccile^{a,b,c}

a UPMC Univ Paris 06, UMR 7574, Chimie de la Matière Condensée de Paris, F-75005, Paris, France.

b CNRS, UMR 7574, Chimie de la Matière Condensée de Paris, F-75005, Paris, France

c Collège de France, UMR 7574, Chimie de la Matière Condensée de Paris, F-75005, Paris, France

d SynBioC Research Group, Departement of Sustainable Organic Chemistry and Technology, Faculty of Bioscience Engineering, Ghent University, Coupure links 653, B-9000 Gent, Belgium

e Laboratoire Léon Brillouin, CEA Saclay, F-91191 Gif-sur-Yvette Cedex, France

f InBio, Department of Biochemical and Microbial Technology, Faculty of Bioscience Engineering, Ghent University, Coupure Links 653, 9000, Ghent, Belgium

g Institut Pasteur, UMR3528, 28 Rue du Docteur Roux, F-75015, Paris, France

niki.baccile@upmc.fr

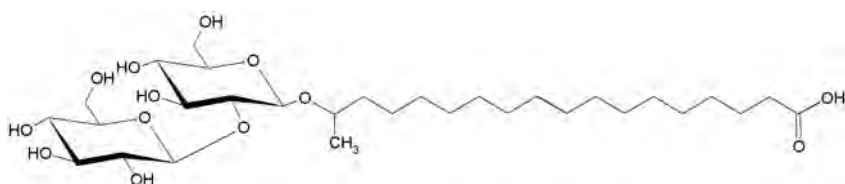


Figure 1 : Saturated C18:0 sophorolipids (SL).

Supramolecular chirality is still poorly understood and difficult to predict although it is very interesting for applications like hydrogelation, templates for mineral supports for enantiomeric separations and tissue engineering. We studied this phenomenon for the saturated form of sophorolipids unexpectedly forming chiral nanofibers only under neutral and acidic pH conditions. We illustrate that this phenomenon derives from a subtle cooperative effect of molecular chirality, hydrogen bonding, van der Waals forces and steric hindrance.

Supramolecular self-assembly of natural and synthetic amphiphiles is an important topic in nanoscience, as it constitutes a promising tool to build complex 1D to 3D nanoscale objects.¹ In particular, the effect of chirality on supramolecular self-assembly is at the origin of life (DNA), of tissue and bone engineering (collagen), of human diseases (amyloid fibrillation) but also structural protection of microorganisms (capsid formation in viruses). Chirality-induced structural strength, mechanical rigidity and functionality² strongly impact the properties and role of self-assembled soft systems (proteins, lipids, nucleic acids) in natural processes³.

Glycolipids constitute an important class of amphiphiles and are gaining more and more interest because of their biocompatibility, biodegradability and low toxicity. In particular, the use of sugars is of specific interest because of their biologically-relevant functionality occurring in cell-cell agglutination mechanisms. Among this class of compounds, sophorolipids (SL) are natural bolaform glycolipids that can be obtained from the fermentation process of the yeast *Starmerella bombicola*.

In the present work, we present the first example of the pH-triggered formation of self-assembled fibers with nanoscale chirality using a saturated SL (C18:0 SL, Fig.1) thus contributing to the development of interesting pH-responsive bio-based chiral materials.

We highlight the fact that acidic C18:0 SL contains all those chemical elements (ether bond junction, headgroups asymmetry) that have shown to provide the least chiral activity.⁴

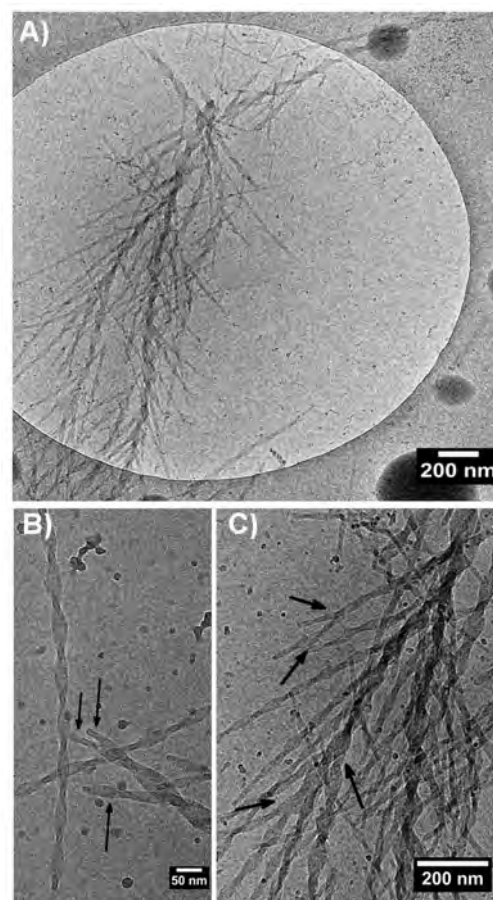


Figure 2 – (A-C) Cryo-TEM images of self-assembled C18:0 SL structures at 5 mg/mL, pH 6.

pH-driven self-assembly. The C18:0 SL are studied here at concentrations as high as 5 mg/mL after a previous solubilization step at pH= 11. To study the morphology of the self-assembled species formed at acidic pH, cryo-TEM was performed (Fig. 2). The images in Fig. 2B and C illustrate the presence of chirality from single fibrils up to associations of fibrils into thicker fibers, as highlighted by the arrows. Fig. 2A shows a typical example of a large bundle composed of many individual fibrils.

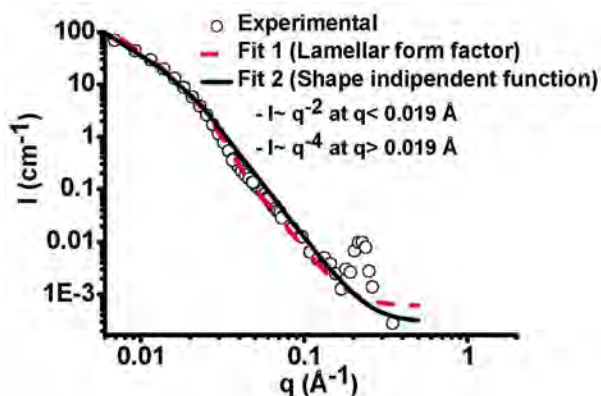


Figure 3 SANS data for C18:0 SL, 5 mg/mL, pH 6. Fit of the SANS curve using a lamellar form factor or a model-independent two-power law ($I \sim q^{-2}q^{-4}$) function implemented in the software SANS View are also presented.

These results were confirmed by SANS experiments at the PACE spectrometer (LLB). Full circles in Fig. 3 identify the SANS spectra for C18:0 SL at 5 mg/mL and pH 6.

Similar results are observed at pH 2 (not shown). We can distinguish at least three different regimes: at $q < 0.01 \text{ \AA}^{-1}$, the intensity $I(q) \sim q^{-2}$; at $q > 0.01 \text{ \AA}^{-1}$, the spectrum shows an inflection point with a slope close to q^{-4} ; at $q=0.237 \text{ \AA}^{-1}$ an intense peak appears corresponding to a periodic distance $d= 2.65 \text{ nm}$. We could nicely fit SANS spectrum using a lamellar form factor or a model independent (two-power law) function, where both functions display a $I(q) \sim q^{-2}q^{-4}$ dependence, thus representing a good qualitative model for chiral ribbons^{5,6}, confirming the cryo-TEM experiments and suggesting that the sample is mostly composed of nanoscale ribbons with supramolecular chirality.

This structure, at such scales, has not been observed before for any other SL. Supramolecular chirality is often induced by local stereo centers.⁷ In the C18:0 SL, the subterminal (C_{17}) is always in the S-enantiomeric form, probably playing an important

role in the formation of the nanoscale ribbons. However, additional driving forces must contribute to this process: hydrogen-bonding (proven by pH-titration, DLS and solid state NMR), for instance. But hydrophobic interactions also play a role, as demonstrated by the fact that C18:1-*cis* SL do not show the formation of any chiral supramolecular structure under comparable conditions⁸. The combination of hydrogen bonding, hydrophobic interactions and presence of a stereocenter located on C_{17} could justify the formation of supramolecular chirality to release local tensions.

Conclusion. This work shows how supramolecular nanoscale chirality can be obtained from yeast-derived asymmetric bola-glycolipids and how such a phenomenon is strongly related to the coexistence of several “chirality triggers”: stereocenters, hydrogen bonding, hydrophobic interactions and, above all, pH. This work also illustrates that such behavior is still difficult to predict, at least for bolaform glycolipids, and needs to be studied in a systematic way as it has been done for aminoacid and peptide-based amphiphiles. For more pieces of information, please refer to the original work published in *Soft Matter*, 2014,10, 3950-3959.

References

- 1 D. Philp *et al.*, *Angew. Chem. Int. Ed. Engl.*, 1996, **35**, 1154.
- 2 M. R. Falvo *et al.*, *Biophys. J.*, 1997, **72**, 1396.
- 3 M. R. Sawaya *et al.*, *Nature*, 2007, **447**, 453.
- 4 G. John *et al.*, *Adv. Mater.*, 2001, **13**, 715.
- 5 I. W. Hamley, *Macromolecules*, 2008, **41**, 8948.
- 6 J. E. Goldberger *et al.*, *Angew. Chem. Int. Ed. Engl.*, 2011, **50**, 6292.
- 7 L. Ziserman *et al.*, *Phys. Rev. Lett.*, 2011, **106**, 238105
- 8 N. Baccile *et al.*, *ACS Nano*, 2012, **6**, 4763.

TUNING THE COLLOIDAL STABILITY IN IONIC LIQUIDS BY CONTROLLING THE NANOPARTICLES/LIQUID INTERFACE

M. Mamusa^a, J. Siriex-Plénet^a, F. Cousin^b, E. Dubois^a, V. Peyre^a

^a Université Pierre et Marie Curie - Paris 6 - PHENIX UMR CNRS 8234, Paris, France

^b Laboratoire Léon Brillouin, CEA-CNRS, CEA-Saclay, Gif-sur-Yvette, France

veronique.peyre@upmc.fr

To shed light on the origin of colloidal stability in ionic liquids, we focus on a model colloidal system (maghemite nanoparticles) in which surface charge and counterion nature can be controlled at will. We thus evidence the crucial role of interfacial features on dispersion quality in a standard ionic liquid, ethylammonium nitrate.

Ionic liquids (ILs) are a class of tunable solvents composed exclusively of ions and liquid below 100 °C. ILs owe their fame as 'green' compounds to some interesting properties, such as nonflammability, negligible vapour tension and high thermal stability, thanks to which they have been considered as replacements of classical and more dangerous organic solvents over the last few decades. Potential uses are as reaction media for organic and inorganic synthesis, and for the reparation of magneto-rheological fluids, lubricants and electrochemical devices [1]. Initially used for chemical synthesis and electrochemistry, they are now used as solvent carriers in colloidal suspensions, either as perfect dispersions or as gels, with various applications such as heterogeneous catalysis, heat-transfer fluids, dye-sensitized solar cells or gas sensors. Colloidal stability was sometimes ensured by steric repulsions provided by polymers or surfactants at the surfaces of the nanoparticles (NPs), but stable dispersions were also obtained on pristine NPs without any added molecules. In this last case, the mechanisms ensuring the colloidal stability remain basically ill-understood. Indeed, the celebrated DLVO theory that is classically used to describe colloidal stability in polar solvents cannot be invoked with ILs, given that each solvent molecule is an ion.

The aim of our study was then to probe the role of the surface state of NPs on a model system for which the interface between the solid NPs and the solvent can be modified, by tuning either the charge of the NPs or the nature of their counterions.

This model system is based on a well-known aqueous dispersion of iron oxide magnetic nanoparticles of gFe_2O_3 of ~ 10 nm, which are further transferred to ethylammonium nitrate (EAN), an IL considered as rather similar to water. The key point was that initial colloidal stability can be tuned in water prior to their transfer either by playing on pH, to change the surface charge of the NP, or by changing the nature of the counterion in water. Furthermore, the PZC of the NPs (initially at 7.2) can be shifted by the adsorption of citrate molecules, providing negative charges to the NPs at neutral pH.

The first step was to check if stable colloidal suspensions can be obtained in EAN with various conditions of NPs surface. Exchange was achieved by mixing EAN to the initial aqueous colloidal suspensions, water being subsequently removed by freeze-drying. As shown by visual inspection (Figure 1), the step of mixing water and EAN leads to the formation of NP aggregates which disappear completely, in part or not at all, after water removal, depending on the conditions. Without citrate, suspensions are completely floc-

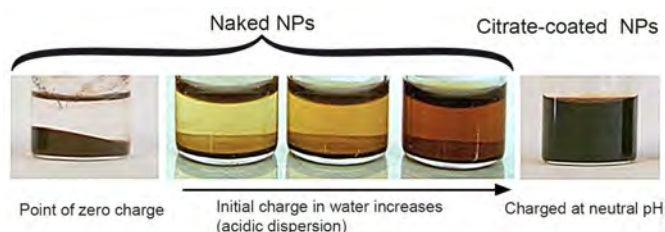


Figure 1 : Pictures of the vials containing the colloidal suspensions in EAN. Due to the strong absorption of visible light by maghemite nanoparticles, the suspensions are red (brownish when turbid).

culated at PZC while partial dispersion can be reached in acidic conditions when NPs are positively charged. Conversely, stable suspensions can be obtained with citrate ligands when NPs are negatively charged. Thus, uncharged particles cannot be dispersed in EAN.

In order to probe the possible influence of the initial counterion of the NPs in water, transfer was achieved for the citrate-coated nanoparticles (that give stable dispersions with standard Na^+ counterion) with several types of positive counterions. Using the alkaline series (Li^+ , K^+ and Cs^+) and various ammonium derivatives (NH_4^+ , ethylammonium EtA^+ , and tetramethylammonium TMA^+) allowed probing the influence of the cation size and polarizability, whereas the influence of valence was investigated using the divalent Ca^{2+} counterion. NPs appear macroscopically successfully redispersed in EAN with all monovalent counterions, except for Li^+ . Indeed, in this case, upon transfer to the IL the sample is initially flocculated; the supernatant progressively darkens over a few days, indicating slow redispersion of the particles. Similar behavior is observed with divalent Ca^{2+} ions.

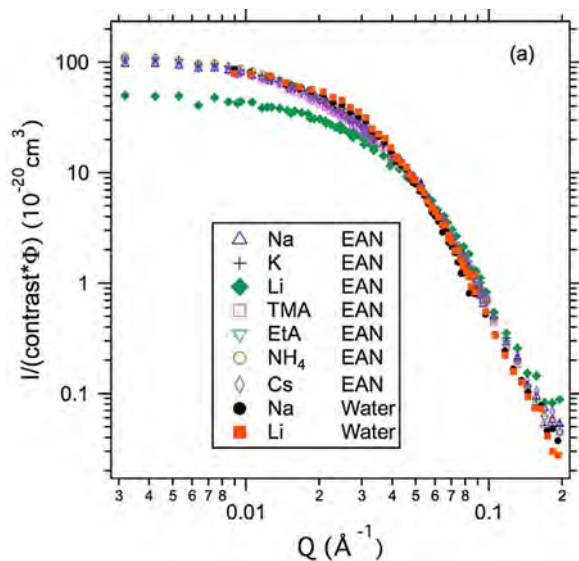


Figure 2: SANS curves of citrate-coated NPs.

In order to obtain more detailed information about the exact role of NP charge and counterion nature for monovalent species, we probed the colloidal suspensions in EAN at local scale by SANS on dilute suspensions (around $\Phi_{\text{NPs}} \sim 1\%$). Results are shown in Figure 2, where they are compared with the initial dispersions in water.

All curves look like pure form factors and can be fitted with a form factor of spheres with a lognormal distribution of the diameters. Thus, a stable dispersed state of the colloids is obtained in all cases and interparticle interactions were undetectable, as evidenced by the

lack of an apparent structure factor. This dispersion of individual particles nevertheless demonstrates that interparticle repulsion exist, the magnitude of which is of the order as the of sum of Van der Waals attractions and dipolar magnetic interactions (attractive on average). All scattering curves in EAN superimpose except for the Li^+ , and are very close to the ones in water, the diameters obtained being very slightly smaller in NEA ($d_0 = 5.2 \text{ nm}$, $s = 0.43$) than in water ($d_0 = 5.6 \text{ nm}$, $s = 0.44$). In contrast, the NPs are much smaller in EAN with Li^+ ($d_0 = 4.6 \text{ nm}$, $s = 0.40$). Such results clearly prove that, upon transfer from water to EAN, in the case of Li^+ , the smaller particles are more easily dispersed than larger ones (that remain in the flocculated fraction). Such an effect is also detectable, although weaker, for the other counterions in EAN. Furthermore, the nature of the counterion clearly affects the solid/liquid interface in EAN. Indeed, if the initial counterion of citrate had been fully replaced by EtA^+ (*i.e.*, the cation of EAN), which is present in large excess, all systems would display similar behaviour and structure. Consequently, the differences observed in the specific case of Li^+ prove that the counterions of the initial aqueous system (at least in the case of this ion) remain close to the solid surface in EAN. This experimental evidence is consistent with the most commonly accepted idea nowadays that interparticle repulsions involve a layered organization of the IL at the nanoparticle/IL, laying between 2-8 ion pairs. Indeed, the counterion can only play a role if it stays at the vicinity of the NP within this structured layer. Moreover, it has already be reported in literature [2] that Li^+ has a strong influence on the structuration of the interface, which may explain the peculiar behavior we observed for such counterion.

This first study [3] demonstrated that it was possible to obtain ferrofluids (colloidal suspensions of magnetic NPs) in ionic liquids, at low Φ (around 1%). Ongoing work concerns the extension to much larger volume fractions and we have already obtain stable concentrated suspensions that show the spectacular Rosensweig's peak instability of ferrofluids.

References

- 1 T. Torimoto, T. Tsuda, K. Okazaki and S. Kuwabata, *Adv. Mater.*, 2010, 22, 1196–1221.
- 2 J. Nordström, L. Aguilera and A. Matic, *Langmuir*, 2012, 28, 4080–4085.
- 3 M. Mamusa, J. Sirieix-Plenet, F. Cousin, E. Dubois, V. Peyre, *Soft Matter*, 2014, 10, 1097–1101.

GELATION OF PECTIN IN PRESENCE OF DIVALENT CATIONS : A REVISITED MECHANISM

A. Assifaoui^{ad}, A. Lerbret^a, H. T. D. Uyen^a, F. Neiers^b, O. Chambin^{ad}, C. Loupiac^{ac}, F. Cousin^c

a UMR PAM, AgroSup Dijon - Université de Bourgogne, Dijon, France.

b CSGA, INRA-CNRS-Université de Bourgogne, Bd Sully, Dijon, France

c Laboratoire Léon Brillouin, CEA-CNRS, CEA-Saclay, Gif-sur-Yvette, France

d Department of Pharmaceutical Technology, School of Pharmacy, Université de Bourgogne, Bd Jeanne d'Arc, Dijon, France

ali.assifaoui@u-bourgogne.fr;

adrien.lerbret@u-bourgogne.fr

[u-bourgogne.fr](mailto:ali.assifaoui@u-bourgogne.fr)

Pectin is an anionic polysaccharide of vegetal origin which is widely used in food and pharmaceutical industries as a gelling, stabilizing and/or encapsulating agent because gelation occurs when pectin interacts with divalent cations. The present work focuses on the gelation process, whether pectin interact with either Ca^{2+} or Zn^{2+} in semi-dilute solutions. Intrinsic viscosity and turbidity measurements reveal that pectin-calcium solutions are more viscous, but yet less turbid, than pectin-zinc ones. This occurs because calcium cations induce the formation of a more homogeneous network of pectin than zinc cations do, as shown by SANS experiments. MD simulation suggest that this difference originates from the way the two cations bind to the galacturonate unit (Gal), the main component of pectin: zinc interacts with both carboxylate and hydroxyl groups of Gal, in a similar way to that described in the so-called egg-box model, whereas calcium only interacts with carboxylate groups.

Pectin is an anionic polysaccharide present in the cell wall of various plants, which has been widely used in food and pharmaceutical industries as a gelling, stabilizing and/or encapsulating agent. It is well known that gelation occurs when pectin is in contact with divalent cations. This gelling property has made pectin a suitable delivery system to escort active compounds from the mouth to the colon. Such gelation mechanism is commonly depicted by the famous *egg-box model* where the chain association is driven by ionic interactions between galacturonate unit (Gal) groups, *i.e.* the elementary unit of the backbone of the pectin macromolecule, mediated by divalent cation bridges. When about 10 consecutive Gal groups are bound, a stable cross-link structure between two chains is formed by dimerization, which corresponds to long chain segments where the cations are sandwiched within the dimers [1].

However, the validity of the egg-box, originally proposed for the calcium-alginate complex, has not yet been established for pectin. In particular, Assifaoui et al. [2] showed that the drug release in pectin-based dosage forms prepared with Ca^{2+} is faster than those prepared with Zn^{2+} because they have a larger swelling ability, revealing that the structure of the gels formed in aqueous

solution before being dried are probably different from one cation to another.

This prompts us to probe the differences between the binding processes of either Ca^{2+} or Zn^{2+} to pectin in semi-dilute solution both at the molecular scale, by coupling isothermal titration calorimetry (ITC) to molecular dynamics (MD) simulations, and at different length scales by coupling small angle neutron scattering (SANS), turbidity and viscosity measurements.

Surprisingly, macroscopic behaviors were opposite for the two divalent cations: viscosity steeply increases above a given $\text{Ca}^{2+}/\text{Gal}$

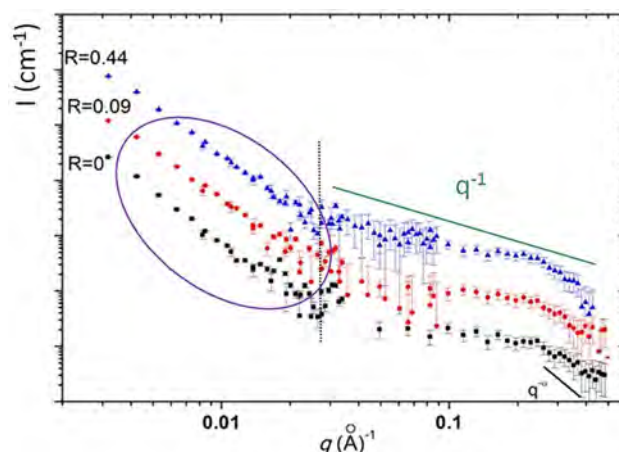


Figure 1 : Typical SANS features of pectin solutions in presence of a cation. R is the cation/Gal ratio. Curves are shifted in intensity for clarity. The low q region of the scattering curve enables to value the concentration fluctuations within the sample. The q^{-1} comes from the rod-like behavior of pectin at local scale and enables the persistence length measurement.

threshold without any noticeable increase of turbidity, while turbidity strongly increases at around the same Zn^{2+}/Gal threshold without any increase of viscosity. These differences can be understood in light of SANS experiments: There are much larger concentration fluctuations at the scales probed by neutrons (up to ~ 100 nm) in the samples containing Zn^{2+} compared to the ones containing Ca^{2+} (Figure 1). The system is thus heterogeneous with Zn^{2+} while it is homogenous with Ca^{2+} .

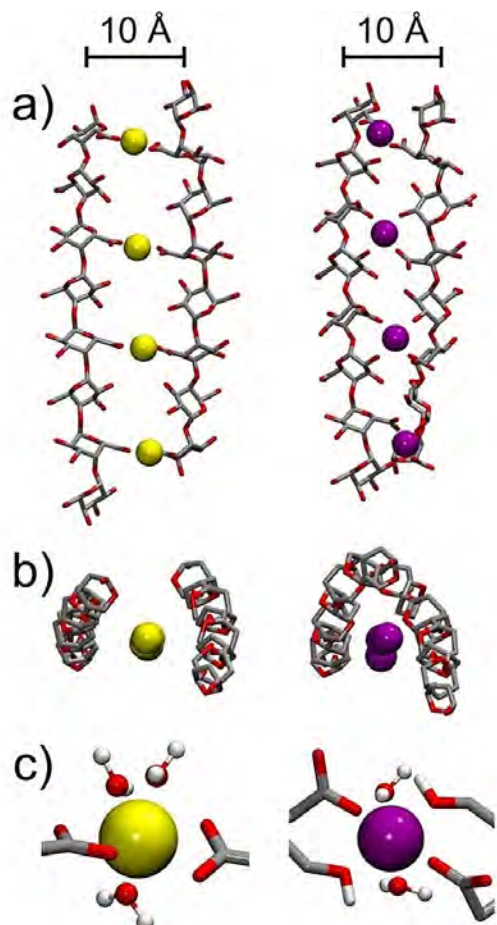


Figure 2 : Time-Averaged structures formed by two galacturonic acid chains in the presence of either calcium (left panels) or zinc (right panels) cations : (a) side view and (b) top view). (c) Examples of configurations of calcium and zinc interacting with galacturonic chains

These behavior differences were due to the local mechanism of complexation of Gal to cation, as revealed by molecular study. Thermodynamics measurements show that it is entropically driven for both cations, due to the entropy gain associated to the desolvation of species. The value of the desolvation energy barrier is larger for Zn^{2+} , than Ca^{2+} . This latter effect is explained by the way the cations interact with Gal, as derived from MD simulations: While Zn^{2+} interact both with COO^- and OH groups of the Gal unit, as expected

in the egg-box model, Ca^{2+} only interact with COO^- (Figure 2.c). The egg-box is thus not valid in case of Ca^{2+} .

Such interaction process authorizes the formation of dimers in case of Ca^{2+} , which ultimately leads to the formation of a rather homogeneous network when such cation cross-links pectin chains to form a gel. On the reverse, only monocomplexation can be achieved with, and the resulting cross-linked network is very heterogeneous [3].

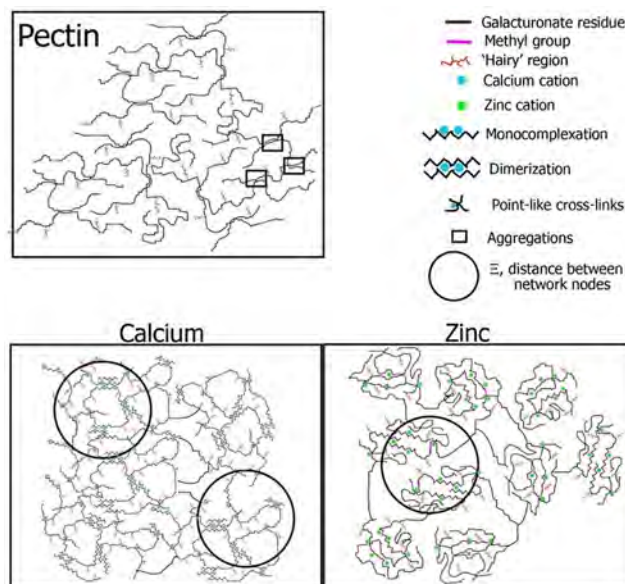


Figure 3 : Suggested scheme for the network of calcium and zinc pectin complexes.

References

- 1 T. Torimoto, T. Tsuda, K. Okazaki and S. Kuwabata, *Adv. Mater.*, 2010, 22, 1196–1221.
- 2 J. Nordström, L. Aguilera and A. Matic, *Langmuir*, 2012, 28, 4080–4085.
- 3 M. Mamusa, J. Sirieix-Plenet, F. Cousin, E. Dubois, V. Peyre, *Soft Matter*, 2014, 10, 1097–1101.



**2
0
1
4**

PUBLICATIONS

- 1 Abel, J., Lamirand-Majimel, M., Majimel, J., Belliere-Baca, V., Harte, V., **Andre, G.**, Prestipino, C., Figueroa, S., Durand, E. & Demourgues, A. Oxygen non-stoichiometry phenomena in $\text{Pr}_{1-x}\text{Zr}_x\text{O}_{2-y}$ compounds ($0.02 < x < 0.5$). *Dalton Transactions* **43**, 15183-15191, (2014).
- 2 Alekseev, P. A., Nemkovski, K. S., Kozlenko, D. P., Menushenkov, A. P., Yaroslavtsev, A. A., Gribanov, A. V., Clementyev, E. S., **Pantalei, C.**, Klobes, B. & Hermann, R. P. Coexistence of long range magnetic order and intervalent state of Eu in $\text{EuCu}_2(\text{Si}_x\text{Ge}_{1-x})_2$: Evidence from neutron diffraction and spectroscopic studies. *Jetp Letters* **99**, 164-168, (2014).
- 3 Alekseev, P. A., Nemkovski, K. S., **Mignot, J. M.**, Clementyev, E. S., Ivanov, A. S., Rols, S., Bewley, R. I., Filipov, V. B. & Shitsevalova, N. Y. Possible undercompensation effect in the Kondo insulator $(\text{Yb,Tm})\text{B}_{12}$. *Physical Review B* **89**, 115121, (2014).
- 4 Anissimova, S., Parshall, D., Gu, G. D., Marty, K., Lumsden, M. D., Chi, S. X., Fernandez-Baca, J. A., Abernathy, D. L., **Lamago, D.**, Tranquada, J. M. & Reznik, D. Direct observation of dynamic charge stripes in $\text{La}_{2-x}\text{Sr}_x\text{NiO}_4$. *Nature Communications* **5**, 3467, (2014).
- 5 Audouard, A., Drigo, L., Duc, F., **Fabreges, X.**, Bosseaux, L. & Toulemonde, P. Tunnel diode oscillator measurements of the upper critical magnetic field of $\text{FeTe}_{0.5}\text{Se}_{0.5}$. *Journal of Physics-Condensed Matter* **26**, 185701, (2014).
- 6 Azzam, F., Moreau, C., **Cousin, F.**, **Menelle, A.**, Bizot, H. & Cathala, B. Cellulose Nanofibril-Based Multilayered Thin Films: Effect of Ionic Strength on Porosity, Swelling, and Optical Properties. *Langmuir* **30**, 8091-8100, (2014).
- 7 Azzam, F., Moreau, C., Marquis, M., Bizot, H., **Cousin, F.** & Cathala, B. Tuning optical properties of cellulose nanofibrils-based multilayered thin films. *Abstracts Of Papers Of The American Chemical Society* **247**, 277-CELL, (2014).
- 8 Baczmanski, A., Gadalinska, E., Wronski, S., Le Joncour, L., Panicaud, B., Francois, M., Braham, C., **Klosek, V.** & Paradowska, A. in *International Conference On Residual Stresses 9 (Icrs 9)* Vol. 768-769 *Materials Science Forum* 289-295 (2014).
- 9 Balima, F., Le Floch, S., San-Miguel, A., Lindner, P., **Brulet, A.**, Duclaux, L. & Pischedda, V. Shear effects on expanded graphite under uniaxial pressure: An in situ small angle neutron scattering study. *Carbon* **74**, 54-62, (2014).
- 10 Barbera, G., Barone, G., Crupi, V., Longo, F., Maisano, G., Majolino, D., Mazzoleni, P., Raneri, S., **Teixeira, J.** & Venuti, V. A multi-technique approach for the determination of the porous structure of building stone. *European Journal of Mineralogy* **26**, 189-198, (2014).
- 11 Barone, G., Crupi, V., Longo, F., Majolino, D., Mazzoleni, P., Raneri, S., **Teixeira, J.** & Venuti, V. Neutron radiography for the characterization of porous structure in degraded building stones. *Journal of Instrumentation* **9**, C05024, (2014).
- 12 **Baroni, P.** & **Noirez, L.** Using light to see neutrons and accessing the 2D high resolution: Barotron: a new pulse for neutron scattering. *American Journal of Applied Sciences* **11**, 1558-1565, (2014).
- 13 Bazin, D., Daudon, M., **Andre, G.**, Weil, R., Veron, E. & Matzen, G. Therapy modifies cystine kidney stones at the macroscopic scale. Do such alterations exist at the mesoscopic and nanometre scale? *Journal of Applied Crystallography* **47**, 719-725, (2014).
- 14 Bedouret, L., **Judeinstein, P.**, Ollivier, J., Combet, J. & Desmedt, A. Proton Diffusion in the Hexafluorophosphoric Acid Clathrate Hydrate. *Journal Of Physical Chemistry B* **118**, 13357-13364, (2014).
- 15 Bernardina, S. D., Alabarse, F., Kalinko, A., Roy, P., Chappuis, M., Vita, N., Hienerwadel, R., Berthomieu, C., **Judeinstein, P.**, **Zanotti, J. M.**, Bantignies, J. L., Haines, J., Catafesta, J., Creff, G., Manceron, L. & Brubach, J. B. New experimental set-ups for studying nanoconfined water on the AILES beamline at SOLEIL. *Vibrational Spectroscopy* **75**, 154-161, (2014).
- 16 Besnard, L., Protat, M., Malloggi, F., Daillant, J., **Cousin, F.**, Pantoustier, N., Guenoun, P. & Perrin, P. Breaking of the Bancroft rule for multiple emulsions stabilized by a single stimuable polymer. *Soft Matter* **10**, 7073-7087, (2014).
- 17 Betanda, Y. A., Helbert, A. L., Brisset, F., **Mathon, M. H.**, Waeckerle, T. & Baudin, T. Measurement of stored energy in Fe-48%Ni alloys strongly cold-rolled using three approaches: Neutron diffraction, Dillamore and KAM approaches. *Materials Science and Engineering a-Structural Materials Properties Microstructure and Processing* **614**, 193-198, (2014).
- 18 Betanda, Y. A., Helbert, A. L., Brisset, F., Wehbi, M., **Mathon, M. H.**, Waeckerle, T. & Baudin, T. Influence of Sulfur on the Recrystallization and $\{100\} < 001 >$ Cube Texture Formation in Fe48%Ni Alloys Tapes. *Advanced Engineering Materials* **16**, 933-939, (2014).
- 19 **Bhowmik, D.**, **Malikova, N.**, Meriguet, G., Bernard, O., **Teixeira, J.** & Turq, P. Aqueous solutions of tetraalkylammonium halides: ion hydration, dynamics and ion-ion interactions in light of steric effects. *Physical Chemistry Chemical Physics* **16**, 13447-13457, (2014).
- 20 Bonville, P., **Gukasov, A.**, **Mirebeau, I.** & **Petit, S.** Towards a model of a dynamical Jahn-Teller coupling at very low temperatures in $\text{Tb}_2\text{Ti}_2\text{O}_7$. *Physical Review B* **89**, 085115 (2014).
- 21 Boulnat, X., Perez, M., Fabregue, D., Douillard, T., **Mathon, M. H.** & De Carlan, Y. Microstructure Evolution in Nano-reinforced Ferritic Steel Processed By Mechanical Alloying and Spark Plasma Sintering. *Metallurgical and Materials Transactions a-Physical Metallurgy and Materials Science* **45A**, 1485-1497, (2014).
- 22 **Bouty, A.**, Petitjean, L., Degrandcourt, C., Gummel, J., Kwasniewski, P., Meneau, F., **Boue, F.**, Couty, M. & **Jestin, J.** Nanofiller Structure and Reinforcement in Model Silica/Rubber Composites: A Quantitative Correlation Driven by Interfacial Agents. *Macromolecules* **47**, 5365-5378, (2014).

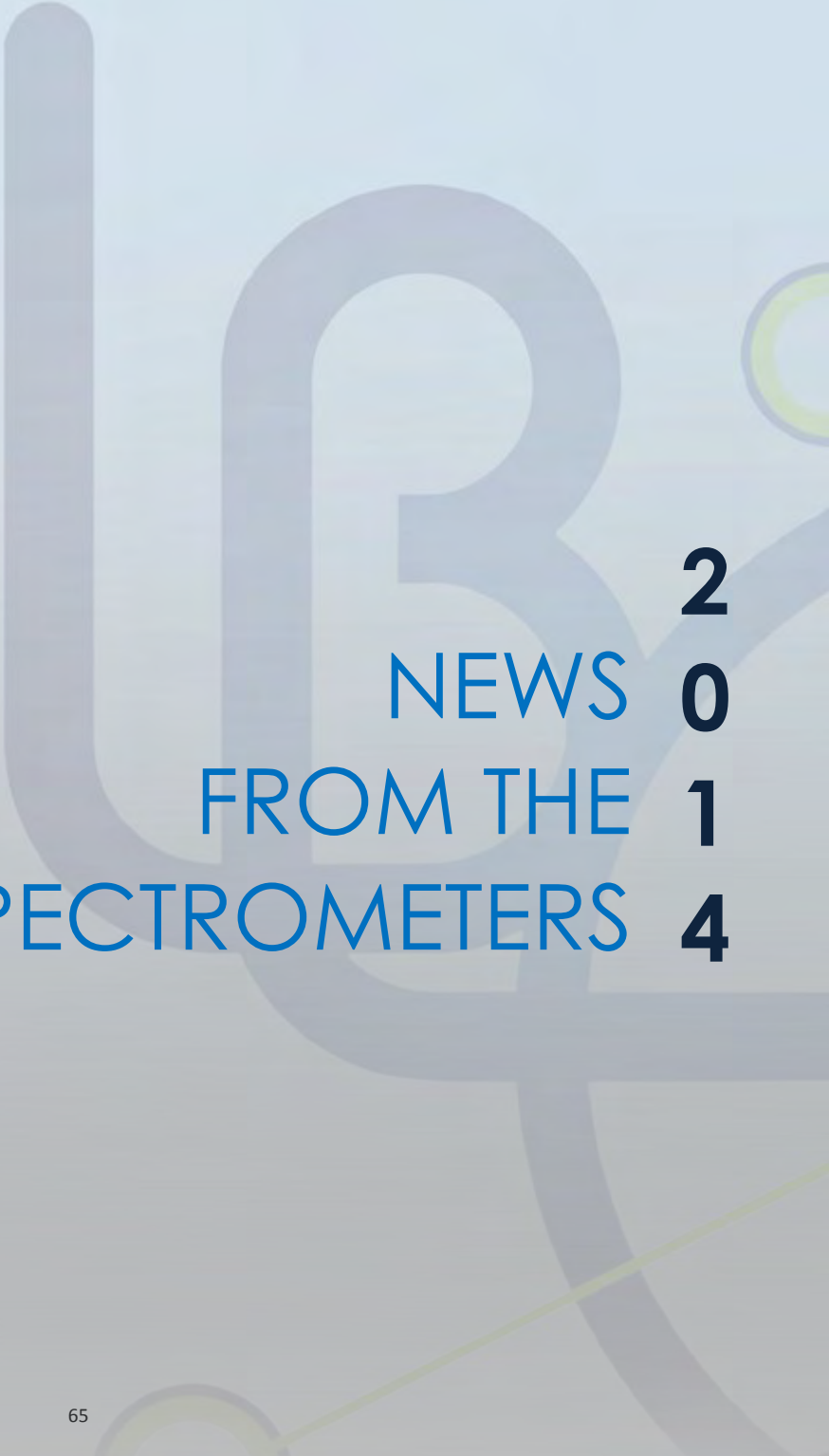
- 23 Bouty, O., Delaye, J. M., **Beuneu, B.** & Charpentier, T. Modelling borosilicate glasses of nuclear interest with the help of RMC, WAXS, neutron diffraction and B-11 NMR. *Journal of Non-Crystalline Solids* **401**, 27-31, (2014).
- 24 Cech, G. M., Pakula, B., Kamrowska, D., Wegrzyn, G., **Arлуison, V.** & Szalewska-Palasz, A. Hfq protein deficiency in Escherichia coli affects ColE1-like but not lambda plasmid DNA replication. *Plasmid* **73**, 10-15, (2014).
- 25 Chaix, L., de Brion, S., **Petit, S.**, Ballou, R., Regnault, L. P., Ollivier, J., Brubach, J. B., Roy, P., Debray, J., Lejay, P., Cano, A., Ressouche, E. & Simonet, V. Magneto- to Electroactive Transmutation of Spin Waves in ErMnO₃. *Physical Review Letters* **112**, 137201 (2014).
- 26 Clochard, M. C., El Jouad, M., Biziere, N., Do Chung, P., Drouhin, H. J., Balanzat, E., **Lairez, D.**, Viret, M. & Wegrowe, J. E. Magnetic nanoconstrictions made from nickel electrodeposition in polymeric bi-conical tracks: Magneto-transport behavior. *Radiation Physics and Chemistry* **94**, 66-71, (2014).
- 27 Crupi, V., Fontana, A., Giarola, M., **Longeville, S.**, Majolino, D., Mariotto, G., Mele, A., Paciaroni, A., Rossi, B., Trotta, F. & Venuti, V. Vibrational Density of States and Elastic Properties of Cross-Linked Polymers: Combining Inelastic Light and Neutron Scattering. *Journal of Physical Chemistry B* **118**, 624-633, (2014).
- 28 Cuvier, A. S., Berton, J., Stevens, C. V., **Fadda, G. C.**, Babonneau, F., Van Bogaert, I. N. A., Soetaert, W., Pehau-Arnaudet, G. & Baccile, N. pH-triggered formation of nanoribbons from yeast-derived glycolipid biosurfactants. *Soft Matter* **10**, 3950-3959, (2014).
- 29 Dalla Bernardina, S., Brubach, J. B., **Berrod, Q.**, Guillermo, A., **Judeinstein, P.**, Roy, P. & Lyonnard, S. Mechanism of Ionization, Hydration, and Intermolecular H-Bonding in Proton Conducting Nanostructured Ionomers. *Journal Of Physical Chemistry C* **118**, 25468-25479, (2014).
- 30 Dalmas, F., **Genevaz, N.**, Roth, M., **Jestin, J.** & Leroy, E. 3D Dispersion of Spherical Silica Nanoparticles in Polymer Nanocomposites: A Quantitative Study by Electron Tomography. *Macromolecules* **47**, 2044-2051, (2014).
- 31 Dammak, A., Moreau, C., Beury, N., Gouider, L., **Cousin, F.**, Jean, B., Bonnin, E., Quemener, B. & Cathala, B. Structurally colored nanometric thin films composed of plant cell wall polymers for enzymatic activities detection. *Abstracts Of Papers Of The American Chemical Society* **247**, 306-CELL, (2014).
- 32 Dejoie, C., Martinetto, P., Tamura, N., Kunz, M., **Porcher, F.**, Bordat, P., Brown, R., Dooryhee, E., Anne, M. & McCusker, L. B. Crystal Structure of an Indigo@Silicalite Hybrid Related to the Ancient Maya Blue Pigment. *Journal Of Physical Chemistry C* **118**, 28032-28042, (2014).
- 33 **Deutsch, M.**, Bonville, P., Tsvyashchenko, A. V., Fomicheva, L. N., **Porcher, F.**, **Damay, F.**, **Petit, S.** & **Mirebeau, I.** Stress-induced magnetic textures and fluctuating chiral phase in MnGe chiral magnet. *Physical Review B* **90**, 144201, (2014).
- 34 **Deutsch, M.**, **Gillon, B.**, Claiser, N., Gillet, J.-M., Lecomte, C. & Souhassou, M. First spin-resolved electron distributions in crystals from combined polarized neutron and X-ray diffraction experiments. *IUCrJ* **1**, 194-199, (2014).
- 35 **Deutsch, M.**, Makarova, O. L., Hansen, T. C., Fernandez-Diaz, M. T., Sidorov, V. A., Tsvyashchenko, A. V., Fomicheva, L. N., **Porcher, F.**, **Petit, S.**, Koepernik, K., Rossler, U. K. & **Mirebeau, I.** Two-step pressure-induced collapse of magnetic order in the MnGe chiral magnet. *Physical Review B* **89**, 180407, (2014).
- 36 Drees, Y., Li, Z. W., Ricci, A., Rotter, M., Schmidt, W., **Lamago, D.**, Sobolev, O., Rutt, U., Gutowski, O., Sprung, M., Piovano, A., **Castellan, J. P.** & Komarek, A. C. Hour-glass magnetic excitations induced by nanoscopic phase separation in cobalt oxides. *Nature Communications* **5**, 5731, (2014).
- 37 **Dubois, M.**, **Mathon, M. H.**, **Klosek, V.**, Benmarouane, A. & Lodini, A. Study of the Influence of Plastic Deformation on Metastable Phases of CuAlBe Shape Memory Alloy by Neutron Diffraction. *Advanced Materials Research* **922**, 114-119, (2014).
- 38 Duc, F., **Fabreges, X.**, Roth, T., Detlefs, C., Frings, P., Nardone, M., Billette, J., Lesourd, M., Zhang, L., Zitouni, A., Delescluse, P., Beard, J., Nicolin, J. P. & Rikken, G. A 31 T split-pair pulsed magnet for single crystal x-ray diffraction at low temperature. *Review of Scientific Instruments* **85**, 053905, (2014).
- 39 Elghazrani, K., Azougarh, A., **Oberdisse, J.** & Filali, M. Interactions between microemulsion droplets decorated with hydrophobically modified polymers: A small-angle neutron scattering study. *European Physical Journal E* **37**, 128, (2014).
- 40 Emuna, M., Mayo, M., Greenberg, Y., Caspi, E. N., **Beuneu, B.**, Yahel, E. & Makov, G. Liquid structure and temperature invariance of sound velocity in supercooled Bi melt. *Journal of Chemical Physics* **140**, 094502, (2014).
- 41 Essafi, W., Raissi, W., Abdelli, A. & **Boue, F.** Metastability of Large Aggregates and Viscosity, and Stability of The Pearl Necklace Conformation After Organic Solvent Treatment Of Aqueous Hydrophobic Polyelectrolyte Solutions. *Journal Of Physical Chemistry B* **118**, 12271-12281, (2014).
- 42 Fajari, L., **Papoular, R.**, Reig, M., Brillas, E., Jorda, J. L., Vallcorba, O., Rius, J., Velasco, D. & Julia, L. Charge Transfer States in Stable Neutral and Oxidized Radical Adducts from Carbazole Derivatives. *Journal of Organic Chemistry* **79**, 1771-1777, (2014).
- 43 Fameau, A.-L. & Zemb, T. Self-assembly of fatty acids in the presence of amines and cationic components. *Advances In Colloid And Interface Science* **207**, 43-64, (2014).
- 44 **Fang, W. Q.**, Panagiotopoulos, I., **Ott, F.**, **Boue, F.**, Ait-Atmane, K., Piquemal, J. Y., Viau, G. & Dalmas, F. Optimization of the magnetic properties of aligned Co nanowires/polymer composites for the fabrication of permanent magnets. *Journal of Nanoparticle Research* **16**, 2265, (2014).

- 45 Fathi, S., Bouazizi, S., Trabelsi, S., Gonzalez, M. A., Bahri, M., Nasr, S. & **Bellissent-Funel, M. C.** Structural investigation of liquid acetic acid by neutron scattering, DFT calculations and molecular dynamics simulations. Complementarity to x-ray scattering results. *Journal of Molecular Liquids* **196**, 69-76, (2014).
- 46 Favvas, E. P., Stefanopoulos, K. L., Nolan, J. W., Pappageorgiou, S. K., Mitropoulos, A. C. & **Lairez, D.** Mixed Matrix Hollow Fiber Membranes with enhanced gas permeation properties. *Separation and Purification Technology* **132**, 336-345, (2014).
- 47 Faye, R., Liu, H., **Kiat, J. M.**, Dkhil, B. & Janolin, P. E. Non-ergodicity and polar features of the transitional phase in lead zirconate. *Applied Physics Letters* **105**, 162909, (2014).
- 48 Finger, T., Binder, K., **Sidis, Y.**, Maljuk, A., Argyriou, D. N. & Braden, M. Magnetic order and electromagnon excitations in DyMnO₃ studied by neutron scattering experiments. *Physical Review B* **90**, 224418 (2014).
- 49 Geinguenaud, F., Gesson, M. & **Arluison, V.** Thermodynamic aspects of the self-assembly of DsrA, a small noncoding RNA from Escherichia coli. *Acta Biochimica Polonica* **61**, 179-184, (2014).
- 50 Gibrat, G., Hoa, G. H. B., Craescu, C. T., Assairi, L., Blouquit, Y., **Annighofer, B.**, May, R. P. & **Bellissent-Funel, M. C.** High-pressure SANS and fluorescence unfolding study of calmodulin. *Biochimica Et Biophysica Acta-Proteins and Proteomics* **1844**, 1560-1568, (2014).
- 51 Gorbunov, D. I., Henriques, M. S., Andreev, A. V., **Gukasov, A.**, Petricek, V., Baranov, N. V., Skourski, Y., Eigner, V., Paukov, M., Prokleska, J. & Goncalves, A. P. Electronic properties of a distorted kagome lattice antiferromagnet Dy₃Ru₄Al₁₂. *Physical Review B* **90**, 094405, (2014).
- 52 Gorobets, Y. N., Kaurova, I. A., Kuz'micheva, G. M., Shekhovtsov, A. N., Rybakov, V. B. & **Cousson, A.** Influence of the dopant type on point defects in PbMoO₄ crystals. *J. Synch. Investig.* **8**, 734-744, (2014).
- 53 Grigalaitis, R., Ivanov, M., Macutkevicius, J., Banys, J., Carreaud, J., Kiat, J. M., Laguta, V. V. & Zalar, B. Size effects in a relaxor: further insights into PMN. *Journal of Physics -Condensed Matter* **26**, 272201, (2014).
- 54 Hervieu, M., Guesdon, A., Bourgeois, J., Elkaim, E., Poiénar, M., **Damay, F.**, Rouquette, J., Maignan, A. & Martin, C. Oxygen storage capacity and structural flexibility of LuFe₂O_{4+x} (0 ≤ x ≤ 0.5). *Nature Materials* **13**, 74-80, (2014).
- 55 Hiraka, H., Ohoyama, K., Ogata, Y., Ogawa, T., Gallage, R., Kobayashi, N., Takahashi, M., **Gillon, B.**, **Gukasov, A.** & Yamada, K. Polarized-neutron-diffraction study of the microscopic magnetic structure in α''-Fe₁₆N₂ nanoparticles. *Physical Review B* **90**, 134427 (2014).
- 56 Hutanu, V., Sazonov, A. P., Meven, M., Roth, G., **Gukasov, A.**, Murakawa, H., Tokura, Y., Szaller, D., Bordacs, S., Kezsmarki, I., Guduru, V. K., Peters, L., Zeitler, U., Romhányi, J. & Nafradi, B. Evolution of two-dimensional antiferromagnetism with temperature and magnetic field in multiferroic Ba₂CoGe₂O₇. *Physical Review B* **89**, 064403 (2014).
- 57 Ito, K., Yoshida, K., **Bellissent-Funel, M. C.** & Yamaguchi, T. Dynamic Properties of Water Confined in Sephadex G15 Gel by Quasi-Elastic Neutron Scattering and Neutron Spin Echo Measurements. *Bulletin of the Chemical Society of Japan* **87**, 603-608, (2014).
- 58 Jaksch, S., Martin-Rodriguez, D., Ostermann, A., **Jestin, J.**, DuartePinto, S., Bouwman, W. G., Uher, J., Engels, R. & Frielinghaus, H. Concept for a time-of-flight Small Angle Neutron Scattering instrument at the European Spallation Source. *Nuclear Instruments & Methods in Physics Research Section a-Accelerators Spectrometers Detectors and Associated Equipment* **762**, 22-30, (2014).
- 59 Jeong, J., Le, M. D., **Bourges, P.**, **Petit, S.**, Furukawa, S., Kim, S. A., Lee, S., Cheong, S. W. & Park, J. G. Temperature-Dependent Interplay of Dzyaloshinskii-Moriya Interaction and Single-Ion Anisotropy in Multiferroic BiFeO₃. *Physical Review Letters* **113**, 107202, (2014).
- 60 Jlalila, I., Gallier, F., **Brodie-Linder, N.**, Uziel, J., Auge, J. & Lubin-Germain, N. Copper(II) SBA-15: A reusable catalyst for azide-alkyne cycloaddition. *Journal of Molecular Catalysis a-Chemical* **393**, 56-61, (2014).
- 61 Josse, M., Heijboer, P., Albino, M., Molinari, F., **Porcher, F.**, Decourt, R., Michau, D., Lebraud, E., Veber, P., Velazquez, M. & Maglione, M. Original Crystal-Chemical Behaviors in (Ba,Sr)₂Ln(Fe,Nb,Ta)₅O₁₅ Tetragonal Tungsten Bronze: Anion-Driven Properties Evidenced by Cationic Substitutions. *Crystal Growth & Design* **14**, 5428-5435, (2014).
- 62 Jouault, N., Dalmas, F., **Boue, F.** & **Jestin, J.** Nanoparticles reorganizations in polymer nanocomposites under large deformation. *Polymer* **55**, 2523-2534, (2014).
- 63 Jovari, P., Lucas, P., Yang, Z. Y., Bureau, B., Kaban, I., **Beuneu, B.** & Bednarcik, J. Short-Range Order in Ge-As-Te Glasses. *Journal of the American Ceramic Society* **97**, 1625-1632, (2014).
- 64 Kaban, I., Jovari, P., Waske, A., Stoica, M., Bednarcik, J., **Beuneu, B.**, Mattern, N. & Eckert, J. Atomic structure and magnetic properties of Fe-Nb-B metallic glasses. *Journal of Alloys and Compounds* **586**, S189-S193, (2014).
- 65 Kaurova, I. A., Kuz'micheva, G. M. & **Cousson, A.** Application of diffraction methods to the study of volume variations in the composition of a langatate single crystal. *J. Synch. Investig.* **8**, 623-631, (2014).
- 66 Kaurova, I. A., Kuz'micheva, G. M., Rybakov, V. B., **Cousson, A.** & Gayvoronsky, V. Y. Structural peculiarities and point defects of bulk-ZnO single crystals. *Journal Of Alloys And Compounds* **616**, 71-75, (2014).
- 67 Kempa, M., Ondrejovic, P., **Bourges, P.**, Marton, P. & Hlinka, J. Lattice dynamics of NaI studied by inelastic neutron scattering: Absence of thermally induced discrete breathers. *Physical Review B* **89**, 054308 (2014).

- 68 Knizek, K., Jirak, Z., Hejtmanek, J., Veverka, M., Kaman, O., Marysko, M., Santava, E. & **Andre, G.** Effect of Ising-type Tb^{3+} ions on the low-temperature magnetism of La, Ca cobaltite. *Journal of Physics-Condensed Matter* **26**, 116003, (2014).
- 69 Kobayashi, R., Kaneko, K., Saito, K., **Mignot, J. M., Andre, G., Robert, J.**, Wakimoto, S., Matsuda, M., Chi, S. X., Haga, Y., Matsuda, T. D., Yamamoto, E., Nishioka, T., Matsumura, M., Tanida, H. & Sera, M. Influence of Electron Doping on Magnetic Order in $CeRu_2Al_{10}$. *Journal of the Physical Society of Japan* **83**, 104707, (2014).
- 70 Kozhevnikov, S. V., **Ott, F.**, Torrejon, J., Vazquez, M. & Thiaville, A. Application of a polarized neutron microbeam to the investigation of a magnetic microstructure. *Physics of the Solid State* **56**, 57-61, (2014).
- 71 Kul'velis, Y. V., Kononova, S. V., Romashkova, K. A. & Lebedev, V. T. Structure of phase-inversion membranes from small-angle neutron scattering data. *Physics of the Solid State* **56**, 86-90, (2014).
- 72 Kunkemoller, S., Nugroho, A. A., **Sidis, Y.** & Braden, M. Spin-density-wave ordering in $Ca_{0.5}Sr_{1.5}RuO_4$ studied by neutron scattering. *Physical Review B* **89**, 045119 (2014).
- 73 Lefort, R., Jean, F., **Noirez, L.**, Ndao, M., Cerclier, C. V. & Morineau, D. Smectic C chevrons in nanocylinders. *Applied Physics Letters* **105**, 203106, (2014).
- 74 **Lenertz, M.**, Dinia, A., Colis, S., Mentre, O., **Andre, G., Porcher, F.** & Suard, E. Magnetic Structure of Ground and Field Induced Ordered States of Low-Dimensional γ - CoV_2O_6 . *Journal of Physical Chemistry C* **118**, 13981-13987, (2014).
- 75 **Leroy, M. A., Bataille, A. M.**, Dkhil, B., **Porcher, F.**, Barbier, A., Jacques, V. L. R., Lu, Y., Bellouard, C., Hauet, T., Ravy, S., Herrero-Martin, J., Gatel, C., Bouzeshouane, K., **Gukasov, A.**, Andrieu, S. & Tiusan, C. Tunnel-mediated coupling between antiferromagnetic thin films. *Physical Review B* **90**, 035432 (2014).
- 76 Liakakos, N., Blon, T., Achkar, C., Vilar, V., Cormary, B., Tan, R. P., Benamara, O., **Chaboussant, G., Ott, F.**, Warot-Fonrose, B., Snoeck, E., Chaudret, B., Soulantica, K. & Respaud, M. Solution Epitaxial Growth of Cobalt Nanowires on Crystalline Substrates for Data Storage Densities beyond 1 Tbit/in². *Nano Letters* **14**, 3481-3486, (2014).
- 77 Livi, S., Bugatti, V., Soares, B. G. & Duchet-Rumeau, J. Structuration of ionic liquids in a poly(butylene-adipate-co-terephthalate) matrix: its influence on the water vapour permeability and mechanical properties. *Green Chemistry* **16**, 3758-3762, (2014).
- 78 Lorchat, P., Konko, I., Combet, J., **Jestin, J.**, Johner, A., Laschewski, A., Obukhov, S. & Rawiso, M. New regime in polyelectrolyte solutions. *Epl* **106**, 28003, (2014).
- 79 Mahmoudi, N., Gaillard, C., Riaublanc, A., **Boue, F.** & Axelos, M. A. V. Transition from Fractal to Spherical Aggregates of Globular Proteins: Brownian-Like Activation and/or Hydrodynamic Stress? *Current Topics in Medicinal Chemistry* **14**, 630-639, (2014).
- 80 Mamusa, M., Sirieix-Plenet, J., **Cousin, F.**, Perzynski, R., Dubois, E. & Peyre, V. Microstructure of colloidal dispersions in the ionic liquid ethylammonium nitrate: influence of the nature of the nanoparticles' counterion. *Journal Of Physics-Condensed Matter* **26**, 284113, (2014).
- 81 Mamusa, M., Sirieix-Plenet, J., **Cousin, F.**, Dubois, E. & Peyre, V. Tuning the colloidal stability in ionic liquids by controlling the nanoparticles/liquid interface. *Soft Matter* **10**, 1097-1101, (2014).
- 82 **Mangin-Thro, L., Sidis, Y., Bourges, P.**, De Almeida-Didry, S., Giovannelli, F. & Laffez-Monot, I. Characterization of the intra-unit-cell magnetic order in $Bi_2Sr_2CaCu_2O_{8+6}$. *Physical Review B* **89**, 094523 (2014).
- 83 Matsumura, T., Kunimori, K., Kondo, A., Soejima, K., Tanida, H., **Mignot, J. M.**, Iga, F. & Sera, M. Appearance of Antiferromagnetic Dipole Order in $Ce_{0.5}La_{0.5}B_6$ with Pr Ion Doping. *Journal Of The Physical Society Of Japan* **83**, 094724, (2014).
- 84 Maurer, T., Gautrot, S., **Ott, F., Chaboussant, G.**, Zighem, F., Cagnon, L. & Fruchart, O. Ordered arrays of magnetic nanowires investigated by polarized small-angle neutron scattering. *Physical Review B* **89**, 184423 (2014).
- 85 Meher, K., Martin, C., Caignaert, V., **Damay, F.** & Maignan, A. Multiferroics and Magnetoelectrics: A Comparison between Some Chromites and Cobaltites. *Chemistry of Materials* **26**, 830-836, (2014).
- 86 Meshcheriakova, O., Chadov, S., Nayak, A. K., Rossler, U. K., Kubler, J., **Andre, G.**, Tsirlin, A. A., Kiss, J., Hausdorf, S., Kalache, A., Schnelle, W., Nicklas, M. & Felser, C. Large Noncollinearity and Spin Reorientation in the Novel Mn_2RhSn Heusler Magnet. *Physical Review Letters* **113**, 087203, (2014).
- 87 **Mignot, J. M.**, Alekseev, P. A., **Robert, J., Petit, S.**, Nishioka, T., Matsumura, M., Kobayashi, R., Tanida, H., Nohara, H. & Sera, M. Dispersive magnetic-resonance mode in the Kondo semiconductor $CeFe_2Al_{10}$. *Physical Review B* **89**, 161103, (2014).
- 88 **Mirebeau, I. & Petit, S.** Magnetic frustration probed by inelastic neutron scattering: Recent examples. *Journal of Magnetism and Magnetic Materials* **350**, 209-216, (2014).
- 89 Nabi, B., Helbert, A. L., Brisset, F., Batonnet, R., **Andre, G.**, Waeckerle, T. & Baudin, T. Effect of long range order on mechanical properties of partially recrystallized Fe49Co-2V alloy. *Materials Science and Engineering a-Structural Materials Properties Microstructure and Processing* **592**, 70-76, (2014).
- 90 Neuhaus, J., Leitner, M., Nicolaus, K., Petry, W., Hennion, B. & Hiess, A. Role of vibrational entropy in the stabilization of the high-temperature phases of iron. *Physical Review B* **89**, 184302 (2014).
- 91 Nguyen, R., Jouault, N., Zanirati, S., Rawiso, M., Allouche, L., Fuks, G., Buhler, E. & Giuseppone, N. Core-shell inversion by pH modulation in dynamic covalent micelles. *Soft Matter* **10**, 3926-3937, (2014).

- 92 Noirjean, C., Testard, F., **Jestin, J.**, Tache, O., Dejugnat, C. & Carriere, D. Quenched microemulsions: a new route to proton conductors. *Soft Matter* **10**, 5928-5935, (2014).
- 93 **Ott, F.** in *Jdn 20 - Neutrons Et Magnetisme* (eds V. Simonet *et al.*) 02005 (2014).
- 94 **Ott, F.** in *Jdn 20 - Neutrons Et Magnetisme* (eds V. Simonet *et al.*) 02004 (2014).
- 95 Ovsyanikov, A. K., Golosovsky, I. V., Zobkalo, I. A. & **Mirebeau, I.** Magnetic structure and phase transitions in the green phase $^{160}\text{Gd}_2\text{BaCuO}_5$: Neutron diffraction study. *Journal of Magnetism and Magnetic Materials* **353**, 71-75, (2014).
- 96 **Papoular, R. J.** & Papoular, R. Some optical properties of graphite from IR to millimetric wavelengths. *Monthly Notices Of The Royal Astronomical Society* **443**, 2974-2982, (2014).
- 97 Park, S. R., Fukuda, T., Hamann, A., **Lamago, D.**, Pintschovius, L., Fujita, M., Yamada, K. & Reznik, D. Evidence for a charge collective mode associated with superconductivity in copper oxides from neutron and x-ray scattering measurements of $\text{La}_{2-x}\text{Sr}_x\text{CuO}_4$. *Physical Review B* **89**, 020506, (2014).
- 98 Pautrat, A. & **Brulet, A.** Temperature dependence of clusters with attracting vortices in superconducting niobium studied by neutron scattering. *Journal of Physics-Condensed Matter* **26**, 232201, (2014).
- 99 Payamyar, P., Kaja, K., Ruiz-Vargas, C., Stemmer, A., Murray, D. J., Johnson, C. J., King, B. T., Schiffmann, F., VandeVondele, J., Renn, A., Gotzinger, S., Ceroni, P., Schutz, A., **Lee, L. T.**, Zheng, Z. K., Sakamoto, J. & Schluter, A. D. Synthesis of a Covalent Monolayer Sheet by Photochemical Anthracene Dimerization at the Air/Water Interface and its Mechanical Characterization by AFM Indentation. *Advanced Materials* **26**, 2052-2058, (2014).
- 100 **Petit, S.**, **Robert, J.**, **Guitteny, S.**, Bonville, P., Decorse, C., Ollivier, J., Mutka, H., Gingras, M. J. P. & **Mirebeau, I.** Order by disorder or energetic selection of the ground state in the XY pyrochlore antiferromagnet $\text{Er}_2\text{Ti}_2\text{O}_7$: An inelastic neutron scattering study. *Physical Review B* **90**, 060410, (2014).
- 101 Pham, D.-C., Biziere, N., Melilli, G., Pajon, R., Lacour, D., Bouvot, L., Tabellout, M., **Lairez, D.**, Drouhin, H. J., Clochard, M. C. & Wegrowe, J. E. Strain-induced inverse magnetostriction measured on a single contacted Ni nanowire in a polymer matrix. *Materials Research Express* **1**, 045017 (045018 pp.)-045017 (045018 pp.), (2014).
- 102 Pintschovius, L., Reznik, D., Weber, F., **Bourges, P.**, Parrishall, D., Mittal, R., Chaplot, S. L., Heid, R., Wolf, T., **Lamago, D.** & Lynn, J. W. Spurious peaks arising from multiple scattering events involving the sample environment in inelastic neutron scattering. *Journal of Applied Crystallography* **47**, 1472-1476, (2014).
- 103 **Porcher, F. F.**, Souhassou, M. & Lecomte, C. E. P. Experimental determination of electrostatic properties of Na-X zeolite from high resolution X-ray diffraction. *Physical Chemistry Chemical Physics* **16**, 12228-12236, (2014).
- 104 Qureshi, N., Steffens, P., **Lamago, D.**, **Sidis, Y.**, Sobolev, O., Ewings, R. A., Harnagea, L., Wurmehel, S., Buchner, B. & Braden, M. Fine structure of the incommensurate anti-ferromagnetic fluctuations in single-crystalline LiFeAs studied by inelastic neutron scattering. *Physical Review B* **90**, 144503 (2014).
- 105 Rao, M. N., **Lamago, D.**, Ivanov, A., d'Astuto, M., Postnikov, A. V., Hussein, R. H., Basak, T., Chaplot, S. L., Firszt, F., Paszkowicz, W., Deb, S. K. & Pages, O. Lattice dynamics of the model percolation-type (Zn,Be)Se alloy: Inelastic neutron scattering, ab initio study, and shell-model calculations. *Physical Review B* **89**, 155201 (2014).
- 106 Renard, D., Lavenant-Gourgeon, L., **Lapp, A.**, Nigen, M. & Sanchez, C. Enzymatic hydrolysis studies of arabinogalactan-protein structure from Acacia gum: The self-similarity hypothesis of assembly from a common building block. *Carbohydrate Polymers* **112**, 648-661, (2014).
- 107 **Ridier, K.**, **Petit, S.**, **Gillon, B.** & **Chaboussant, G.** Magnetic neutron spectroscopy of a spin-transition Mn^{3+} molecular complex. *Physical Review B* **90**, 104407, (2014).
- 108 Rivin, O., Shaked, H., **Gukasov, A.** & Caspi, E. N. Long-range and short-range magnetic order in the singlet ground state system TbCo_3B_2 . *Physical Review B* **89**, 174423 (2014).
- 109 Saito, K., Laulhe, C., Sato, T., Hao, L., **Mignot, J. M.** & Iwasa, K. Emergence of reentrant metal-nonmetal transition in $\text{Pr}_{0.85}\text{Ce}_{0.15}\text{Ru}_4\text{P}_{12}$ and $\text{Pr}(\text{Ru}_{0.95}\text{Rh}_{0.05})_4\text{P}_{12}$. *Physical Review B* **89**, 075131 (2014).
- 110 Sando, D., Agbelele, A., Daumont, C., Rahmedov, D., Ren, W., Infante, I. C., Lisenkov, S., Prosandeev, S., Fusil, S., Jacquet, E., Carretero, C., **Petit, S.**, Cazayous, M., Juraszek, J., Le Breton, J. M., Bellaiche, L., Dkhil, B., Barthelmy, A. & Bibes, M. Control of ferroelectricity and magnetism in multi-ferroic BiFeO_3 by epitaxial strain. *Philosophical Transactions of the Royal Society a-Mathematical Physical and Engineering Sciences* **372**, 20120438, (2014).
- 111 Schulz, J., **Ott, F.** & Krist, T. An improved prism energy analyzer for neutrons. *Nuclear Instruments & Methods in Physics Research Section a-Accelerators Spectrometers Detectors and Associated Equipment* **744**, 69-72, (2014).
- 112 **Sidis, Y.** in *Jdn 20 - Neutrons Et Magnetisme* (eds V. Simonet *et al.*) 04003 (2014).
- 113 Sood, R., Iojoiu, C., Espuche, E., Gouanve, F., Gebel, G., Mendil-Jakani, H., Lyonnard, S. & **Jestin, J.** Comparative Study of Proton Conducting Ionic Liquid Doped Nafion Membranes Elaborated by Swelling and Casting Methods: Processing Conditions, Morphology, and Functional Properties. *Journal of Physical Chemistry C* **118**, 14157-14168, (2014).

- 114 Stehle, R., Schulreich, C., Wellert, S., Gab, J., Blum, M. M., Kehe, K., Richardt, A., **Lapp, A.** & Hellweg, T. An enzyme containing microemulsion based on skin friendly oil and surfactant as decontamination medium for organo phosphates: Phase behavior, structure, and enzyme activity. *Journal of Colloid and Interface Science* **413**, 127-132, (2014).
- 115 Steins, P., Poulesquen, A., Frizon, F., Diat, O., **Jestin, J.**, Causse, J., Lambertin, D. & Rossignol, S. Effect of aging and alkali activator on the porous structure of a geopolymer. *Journal of Applied Crystallography* **47**, 316-324, (2014).
- 116 Stock, C., Gehring, P. M., Xu, G., **Lamago, D.**, Reznik, D., Russina, M., Wen, J. & Boatner, L. A. Fluctuating defects in the incipient relaxor $K_{1-x}Li_xTaO_3$ ($x=0.02$). *Physical Review B* **90**, 224302 (2014).
- 117 Sudre, G., Hourdet, D., Creton, C., **Cousin, F.** & Tran, Y. Probing pH-Responsive Interactions between Polymer Brushes and Hydrogels by Neutron Reflectivity. *Langmuir* **30**, 9700-9706, (2014).
- 118 Taghbalout, A., Yang, Q. F. & **Arluison, V.** The Escherichia coli RNA processing and degradation machinery is compartmentalized within an organized cellular network. *Biochemical Journal* **458**, 11-22, (2014).
- 119 Taillefumier, M., **Robert, J.**, Henley, C. L., Moessner, R. & Canals, B. Semiclassical spin dynamics of the antiferromagnetic Heisenberg model on the kagome lattice. *Physical Review B* **90**, 064419 (2014).
- 120 Thorner, G., Kiat, J. M., Bogicevic, C. & Kornev, I. Axial hypertoroidal moment in a ferroelectric nanotorus: A way to switch local polarization. *Physical Review B* **89**, 220103, (2014).
- 121 Toulouse, C., Liu, J., Gallais, Y., Measson, M. A., Sacuto, A., Cazayous, M., Chaix, L., Simonet, V., de Brion, S., Pinsard-Godart, L., Willaert, F., Brubach, J. B., Roy, P. & **Petit, S.** Lattice and spin excitations in multiferroic h - $YMnO_3$. *Physical Review B* **89**, 094415 (2014).
- 122 Tresset, G., Tatou, M., Le Coeur, C., Zeghal, M., Bailleux, V., Lecchi, A., Brach, K., Klekotko, M. & Porcar, L. Weighing Polyelectrolytes Packaged in Viruslike Particles. *Physical Review Letters* **113**, 128305 (2014).
- 123 Wang, W., Brisset, F., Helbert, A. L., Solas, D., Drouelle, I., **Mathon, M. H.** & Baudin, T. Influence of stored energy on twin formation during primary recrystallization. *Materials Science and Engineering a-Structural Materials Properties Microstructure and Processing* **589**, 112-118, (2014).
- 124 Wang, W., Helbert, A. L., Brisset, F., **Mathon, M. H.** & Baudin, T. Monte Carlo simulation of primary recrystallization and annealing twinning. *Acta Materialia* **81**, 457-468, (2014).
- 125 Weber, F., Pintschovius, L., Reichardt, W., Heid, R., Bohnen, K. P., Kreyssig, A., Reznik, D. & Hradil, K. Phonons and electron-phonon coupling in YNi_2B_2C . *Physical Review B* **89**, 104503 (2014).
- 126 Wronski, S., Baczanski, A., Gaj, A., Wierzbanski, K., Fitzpatrick, M. E., **Klosek, V.**, Lodini, A. & Marciszko, M. in *Mechanical Stress Evaluation By Neutrons And Synchrotron Radiation Vi Vol. 772 Materials Science Forum* 117-121 (2014).
- 127 Wu, E. D., Sun, G. A., Chen, B., Zhang, J., Ji, V., **Klosek, V.** & **Mathon, M. H.** Neutron Diffraction Study of Strain/Stress States and Subgrain Defects in a Creep-Deformed, Single-Crystal Superalloy. *Metallurgical and Materials Transactions a-Physical Metallurgy and Materials Science* **45A**, 139-146, (2014).
- 128 Xu, J. G., Kuang, X. J., Veron, E., Allix, M., Suchomel, M. R., **Porcher, F.**, Liang, C. L., Pan, F. J. & Wu, M. M. Localization of Oxygen Interstitials in $CeSrGa_3O_{7+δ}$ Melillite. *Inorganic Chemistry* **53**, 11589-11597, (2014).
- 129 Zhang, J., Zheng, L., Guo, X. B., Ji, V. & **Klosek, V.** Residual Stresses Comparison Determined by Short-Wavelength X-Ray Diffraction and Neutron Diffraction for 7075 Aluminum Alloy. *Journal of Nondestructive Evaluation* **33**, 82-92, (2014).
- 130 Zheng, Z. K., Opilik, L., Schiffmann, F., Liu, W., Bergamini, G., Ceroni, P., **Lee, L. T.**, Schutz, A., Sakamoto, J., Zenobi, R., VandeVondele, J. & Schluter, A. D. Synthesis of Two-Dimensional Analogues of Copolymers by Site-to-Site Transmetalation of Organometallic Monolayer Sheets. *Journal of the American Chemical Society* **136**, 6103-6110, (2014).
- 131 **Zhong, S. Y.**, Ribis, J., Baudin, T., Lochet, N., de Carlan, Y., **Klosek, V.** & **Mathon, M. H.** The effect of Ti/Y ratio on the recrystallisation behaviour of Fe-14%Cr oxide dispersion-strengthened alloys. *Journal of Nuclear Materials* **452**, 359-363, (2014).
- 132 **Zhong, S. Y.**, Ribis, J., Lochet, N., de Carlan, Y., **Klosek, V.** & **Mathon, M. H.** Influence of nano-particle coherency degree on the coarsening resistivity of the nano-oxide particles of Fe-14Cr-1W ODS alloys. *Journal Of Nuclear Materials* **455**, 618-623, (2014).
- 133 Zidani, M., Hadid, M. D., Messaoudi, S., Dendouga, F., Bessais, L., Baira, F., Bayarassou, M., Helbert, A. L., **Mathon, M. H.** & Baudin, T. The Drawing Process Of The Wires Of Copper And Aluminum: Evolution Of The Microstructure And (Mechanical/Electrical) Properties. *Metal 2014: 23rd International Conference On Metallurgy And Materials*, 442-446, (2014).



	2
NEWS	0
FROM THE	1
SPECTROMETERS	4

PA20 : A NEW SANS/GISANS INSTRUMENT AT LLB

S. Désert, G. Chaboussant, M. Détrez, P. Lavie, A. Brûlet

Laboratoire Léon Brillouin CEA/
CNRS UMR 12, CEA Saclay,
Gif sur Yvette, France

Sylvain.desert@cea.fr

The new SANS instrument at LLB, PA20, has been installed and completed in 2015 at the end of the cold neutron guide G5 of the hall guide. The guide cross section is 25 mm x 80 mm and delivers cold neutrons with $3 \text{ \AA} < l < 20 \text{ \AA}$. The overall length of the instrument is 40 m and is composed of a 3 m long blockhouse housing a Dornier velocity selector for monochromatization with $\Delta\lambda/\lambda \approx 12\%$ and a polarizing and spin flipper device under vacuum allowing beam polarization of 98% down to 4 \AA . The collimator is 16 m long under vacuum and has 6 sets of slits allowing beam shaping from square collimation for regular SANS to thin rectangular slits designed for GISANS (Grazing Incidence SANS). An additional set of slits is located at the blockhouse entrance to allow a 20/20m collimation/detector distance configuration in non-polarized mode, thus further expanding the accessible Q-range for users. The collimator includes 5 removable sets of guides, a guide field for polarized measurements and two removable sets of focusing lenses placed near the exit of the collimator, close to the sample. Finally, we provided a completely free pathway inside the collimator so as to anticipate eventual developments, future optic implementation or testing. Finally, the collimator is equipped with an extendable nose from 50 to 80 cm allowing a limited path in the air between the collimator exit and the sample.

The sample environment area is completely non-magnetic and consists of an orientable sample table able to accommodate sample changers, electromagnets, and cryomagnets up to 10 Tesla. Installed in 2014, the 64 cm x 64 cm ^3He detector with 5mm resolution can move inside a 19m long evacuated Aluminum detector tank that allows a sample-to-detector distance from 1 to 20 m within 15 minutes. The detector can also be translated perpendicularly to the beam by 30 cm to obtain extra Q-range when needed by the users. A second detector dedicated to larger angles is under construction and the simultaneous use of both detectors will allow measurements of the full Q-range in one shot with a dynamic Q-range $Q_{\text{max}}/Q_{\text{min}} \approx 25$. PA20 will thus allow faster measurements, with "single-shot" access to a wider range of scattering vectors (from very small scattering vectors, lower than 0.01 nm^{-1} (at $l = 8 \text{ \AA}$ and 19 m), up to 7 nm^{-1} (at $l = 4 \text{ \AA}$ and 1 m). Faster data acquisition rates enable kinetic measurements or systematic studies as a function of temperature near phase transitions where better resolution are critical to differentiate between models or theories. To this end, the potential future use of Time of Flight with the insertion of two choppers inside the blockhouse will improve the $\Delta\lambda/\lambda$ resolution between 1 and 2% and extend the dynamic q-range by a factor 10. Also, the increased Q-range coverage allowed by the 2D front and rear detectors will permit a more rigorous analysis of interface effects, their fractal aspects (Porod regime) compared to volume effects (Guinier regime).

Pushing the limits in terms of flux and resolution is also critical when dealing with samples that are difficult to synthesize or that can be obtained only in small quantity. PA20 makes it possible to tackle such studies and complements the LLB SANS



Marc Detrez inspecting the detector tank electric board

suite (PAXY, PACE, TPA) already available for soft matter, material sciences and magnetic studies. Regarding in particular magnetic studies, PA20 will be the first SANS/GISANS facility with multi-wavelength neutron polarization at LLB, fulfilling the needs to study magnetization processes in nano-objects and thin films. The GISANS setup will be particularly useful to study nanostructured surfaces and interfaces (deposited or embedded nano-objects), magnetic domain formation, multilayered materials or magnetic thin films through specular and off-specular signals. Polarized SANS will



View of PA20 from the top of the casemate. The 16m long collimator is in the foreground and the detector tank in the background.

thus increase the possibilities to study strongly correlated electrons systems, complex magnetic configurations (long-range periodicity, frustrated), photomagnetic molecular systems, and composite magnetic materials.

Increased interests in nanosciences (from surfaces or interfaces through magnetic domain formation, multi-layered materials, organic or polymeric layered films, magnetic thin films) have motivated the GISANS option on PA20 which, for this purpose, is equipped with adapted slit collimation and goniometric sample tables. GISANS is less developed worldwide but, as a surface and interface probe, complements SANS and neutron reflectivity techniques as well as GISAXS widely used in Synchrotron facilities. The fact that GISANS is sensitive to the off-specular signal enables to study structural and magnetic inhomogeneities at the surface and even in buried interfaces. Combining high-precision slit collimation and high angular coverage by both rear and front detectors will permit off-specular scattering studies in the most versatile possible way. First GISANS studies will focus essentially in the study of networks of magnetic nano-objects (wires, ribbons), magnetic correlations or domains formed at the surface or at interfaces. Important issues related to emergent materials such as thermoelectrics or multiferroics could be addressed. It will also be possible to study thin magnetic films in both SANS and GISANS modes to address questions related to surface and interface effects, modification of the properties when going from bulk to layers, etc.



Inside view of the 20m long detector tank

A NEW BI-DIMENSIONAL DETECTOR FOR 6T1

V. Klosek, S. Gautrot, A. Laverdunt, F. Prunes, G. Koskas, M.H. Mathon

Laboratoire Léon Brillouin CEA/CNRS
UMR 12, CEA Saclay,
Gif sur Yvette, France

vincent.klosek@cea.fr

Recent years have seen a growing interest from the community of engineers and metallurgists for measuring microstrains and inter- or intra-phases heterogeneities of mechanical behavior (e.g. through in situ experiments under load). We thus decided in 2010 to fully develop a new high flux and high resolution instrument, replacing the old 6T1 diffractometer, optimized for texture characterizations, internal strain measurements from multiple reflections, as well as analysis of line profiles, with reduced counting times. In particular, this new 6T1 is designed for texture studies in multiphase or low symmetry materials, as well as studies of deformation heterogeneities in polycrystalline materials, including mechanical responses of grains as a function of their orientation.

Its development was planned in three stages to spread the financing plan while ensuring users a quasi-continuous operation.

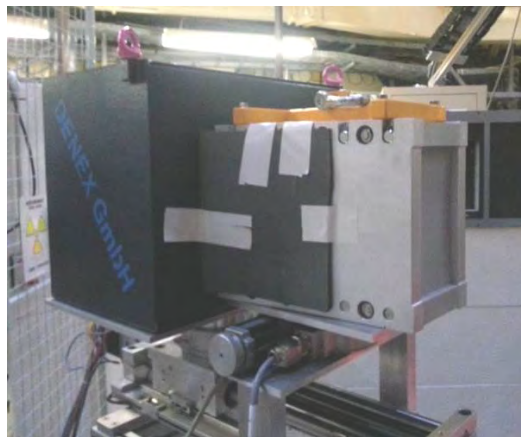


Figure 1: the new 2D detector (within its shielding) mounted on 6T1 with a radial collimator

As a first step, a new innovative Euler cradle with three integrated translations was mounted in 2012, allowing strain or texture mapping. In parallel, we have developed an original sample changer to sequentially measure textures of twelve samples without operation. Besides, the new cradle is compatible with our compact traction machine for in situ internal strain measurements, and with our

furnace for recrystallization studies.

The second step was performed in the beginning of 2014. It consisted in the installation of a new bi-dimensional detector with an active area of 200x200 mm² and a set of four radial collimators (Figure 1).

The multi-wire detector was built by DENEX [1]: it uses 3He as detection gas, and two read-out cathodes associated with two delay lines for horizontal (X) and vertical (Y) position detection. The position resolution is close to 1 mm horizontally and 2 mm vertically. Positioned at a working distance of ~90cm from the sample (i.e. from the rotation center of the cradle), it allows an angular coverage of ~12° in X and Y directions: different diffraction vector orientations with respect to the sample axis system can thus be recorded simultaneously, as well as full diffraction peak profiles over a 2q range of ~12°, with a resolution of ~0.06°.

Acquisition electronic has been developed both by DENEX (filters, preamplifiers, discriminator, ADC/TDC) and LLB (Specmaker acquisition board), and detector readout was implemented in PINGOUIN, the LLB's acquisition software. An additional dedicated software (DataGUInz, Figure 2) has been developed for all image and data treatments (calibrations, image corrections, azimuthal integrations, refinements, etc...).

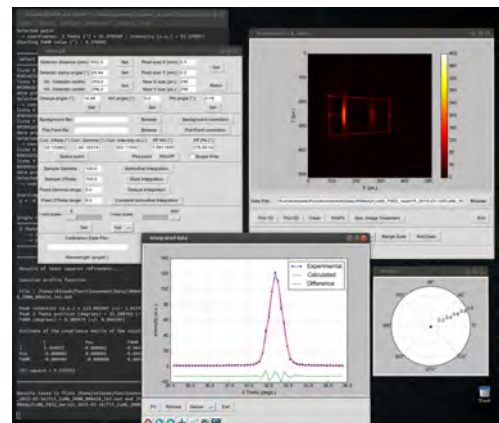


Figure 2: screenshot of the DataGUInz software

The four radial collimators, built by EuroCollimators [2], are designed for covering a wide range of divergences (from 6' to 56') and gauge volumes (FWHM values ranging from 1 to 10 mm), with very low background. Compromises between flux and resolution can thus be found depending on the kind of experiment to be carried out (typically, texture measurements generally favor high flux, whereas a high resolution and a good gauge volume definition are requested for strain measurements).

For instance, in the framework of the METAFORES ANR project, this new experimental setup was successfully applied to characterize in situ the deformation heterogeneities between Cu and Nb in a Cu-Nb architected nanocomposite wire (diam. 2mm) under uniaxial mechanical loading, using our compact tensile machine (Figure 3).

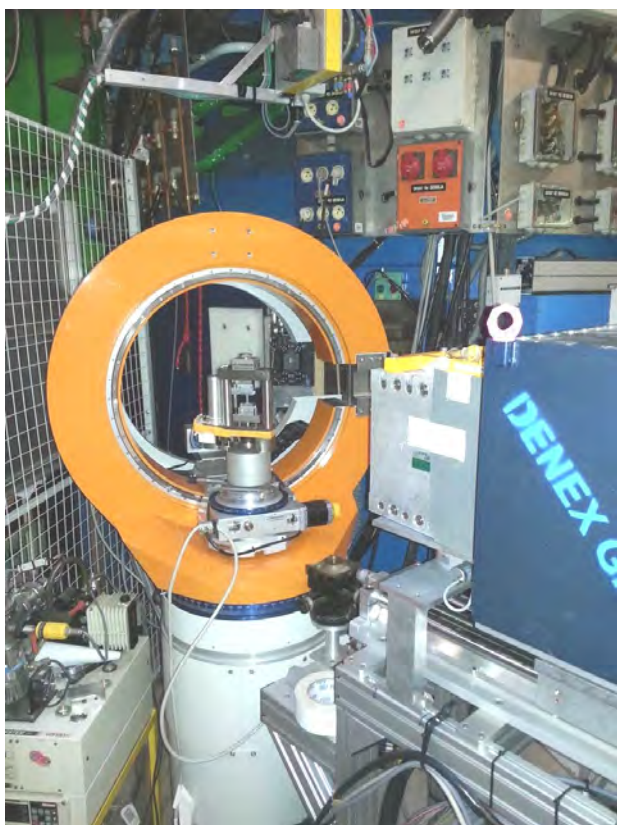


Figure 3: the new 6T1 setup, with the small tensile machine mounted at the center of the Euler cradle.

Studied wire was made of 85² Nb filaments within a Cu multiscale matrix [3]. Mechanical responses of Nb and of different Cu grain families (characterized by different orientations vs. tensile axis) have been obtained as a function of applied stress (Figure 4), from various hkl and sample orientations, with relatively small coating times (~10 min/image/sample orientation): strong heterogeneities can be observed, and these results are being compared with micromechanical simulations in

order to understand the role of the microstructural architecture on the mechanical properties.

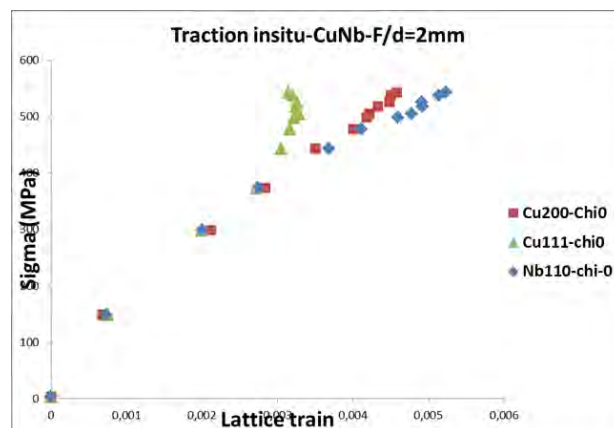


Figure 4: mechanical responses of Nb and Cu as a function of applied stress, the diffraction vector being aligned with the tensile axis.

6T1 still uses a flat Cu (111) monochromator, with a take-off angle of 32° ($\lambda = 1.16 \text{ \AA}$). The last step of this project (scheduled for late 2015 – 2016) will consist in mounting two vertically focusing monochromators (Cu (111) and PG (002)) to optimize the neutron flux at the sample location, and in modifying the monochromator shielding to define three possible take-off angles. Users will then have the choice between six wavelengths depending on the studied material and the kind of measurements: e.g. fast mapping of residual strains with a $2\theta \sim 90^\circ$ geometry will become feasible in "small" engineering samples.

References

- 1 www.denex-gmbh.de
- 2 www.eurocollimators.com
- 3 L. Thilly, S. Van Petegem, P.O. Renault, F. Lecouturier, V. Vidal, B. Schmitt, H. Van Swygenhoven, Acta Materialia 57 (2009) 3157.

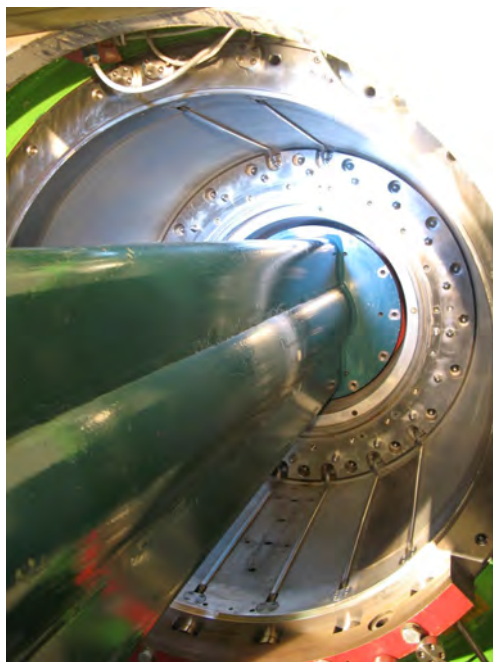
CHANGE OF THE 3T BEAM PLUG

A. Menelle

Laboratoire Léon Brillouin
CEA/CNRS

UMR 12, CEA Saclay, Gif sur
Yvette, France

Alain.menelle@cea.fr



The Orphée reactor provides to users 20 thermal neutrons ports. These beam ports extract neutrons from the heavy water tank through aluminium beam plugs. Submitted to an intense neutron irradiation, aluminium atoms of the beam plugs undergo a transmutation to silicon, resulting in a slow but constant decrease of the mechanical properties of the beam plug. As a consequence, they have to be changed before they reach a fixed irradiation level. During the shutdown of the reactor of the summer 2014, the beam plug of 3T was replaced by a new one.

Ageing of beam plugs

Beam plugs are made of aluminium. They enable the extraction of the neutrons from the heavy water tank to the instruments or neutron guides (see fig. 1). Submitted to irradiation two types of damages may occur. Fast neutrons and high energy particles could knock the atoms and induce displacements. Aluminium sustains quite well this type of damages without important changes of its mechanical properties. This effect will not request a change of the beam plug during the life of the reactor.

Thermal neutrons bear nearly no energy and may not induce direct damages in the structure of aluminium. However, they may be captured and induce transmutations. In that case, the aluminium alloy will be transformed in another one. The nose of the beam plugs being submitted in a neutron flux of $3 \cdot 10^{14}$ n.cm⁻².s⁻¹, after 30 years of operation, it will have seen a fluency of the same order of magnitude than the Avogadro's number. In these conditions, transmutations may completely change the material. If aluminium is mostly transparent to

Ageing of reactor structures

During the operation of a nuclear reactor, structures around the core are submitted to a very high level of irradiations with various types of particles. This creates damages in the materials that experienced changes in their mechanical properties. These changes can be predicted and have to be taken into account in the safety analysis of the reactor. If the design of most of the main parts of the core may be done in order to guarantee that they will not have to be changed in the whole life of the reactor, some of them will have to be replaced. This is the case of the beam plugs that have to be changed roughly each 30 years of operation.

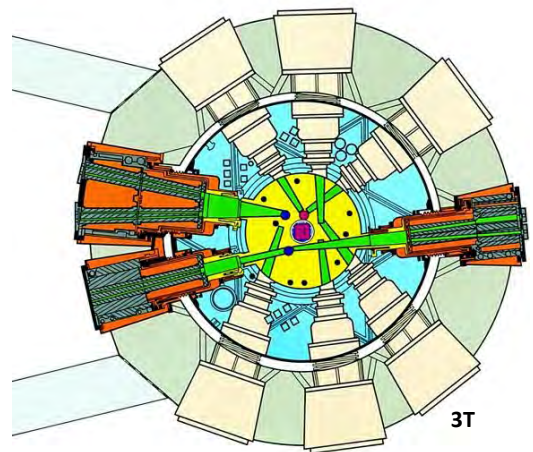


Figure 1 : Top view of the reactor bloc.

With the concrete protection (grey), the light water pool (blue), the heavy water tank (yellow), the core (purple) and beam tubes (green) extracting neutrons to the instruments.

neutrons, a small fraction of them will be captured and some will induce a transformation in silicon. With the time, the increase of silicon content will decrease the ductility of beam plug that will become fragile.

As can be seen on fig. 2, beam plugs play an important role in the safety of a reactor. They prevent heavy water to escape in the beam tubes. This should not occur. Calculations and measurements on test samples have been done to determine the maximum fluency to which aluminium could be submitted to still maintain a sufficient elasticity to sustain chocks created by a nuclear accident. Then according to the dose level to which all beam plugs will be submitted, a calendar of these changes has been set.

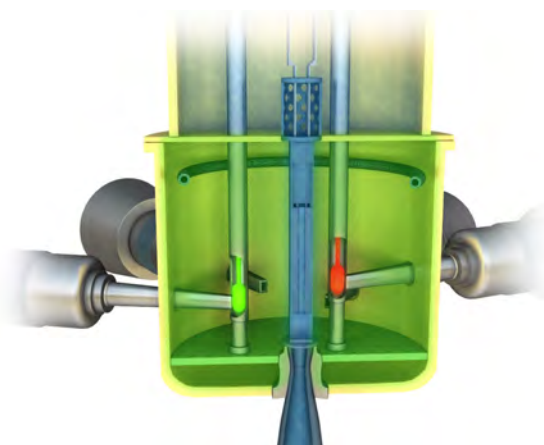


Figure 2 : 3D schematic view of the layout of the beam plugs around the core.

3T beam plug change

After the changes of 4F in 2008 (LLB 2008), 9F in 2012 (LLB 2012), this summer 3T has been replaced.

This operation requires 2.5 months of reactor shut-down. Core is unloaded, heavy water tank drained, all 6 spectrometers from 3T1 to 5C2 removed in order to leave space for the large handling machines used to position all the necessary protections against radiation, remove the old beam plug put in place the new one (see fig. 3). All these operations were successfully done before the summer closure of the Saclay centre mid-August. The nose of the old beam plug being highly radioactive (up to a few Sv), and not the other extremity, it is cut in pieces in order to be able to do waste management according to their activation level. This was finished beginning of September and scientists and technician of the LLB have reconstructed all the removed spectrometers.

By September 15th they were ready to restart normal operation, but other troubles decided other way, but this is another story.

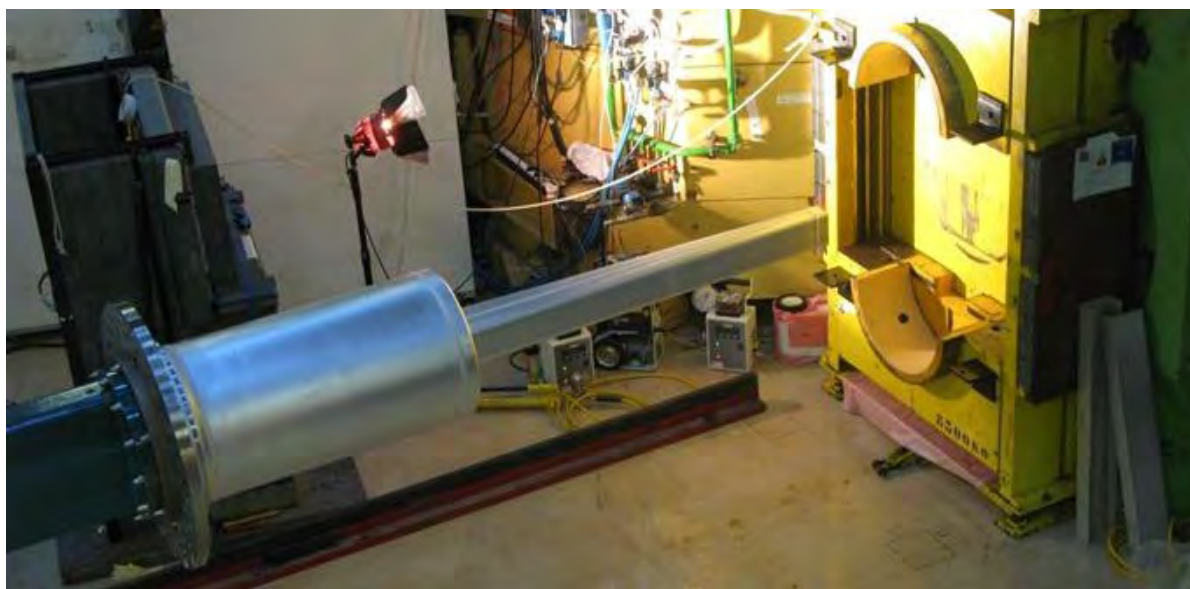


Figure 3 : The new 3T beam plug ready to be inserted

References

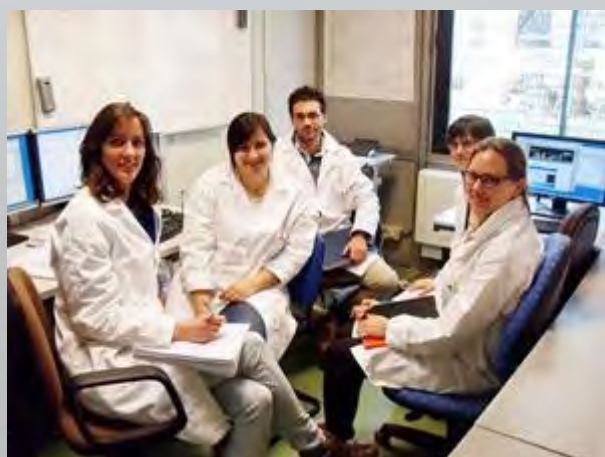
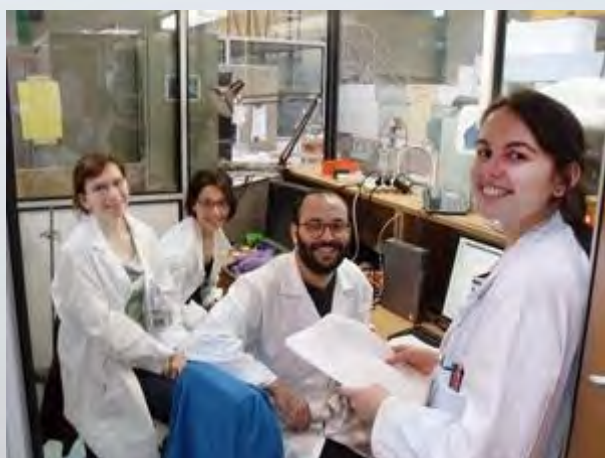
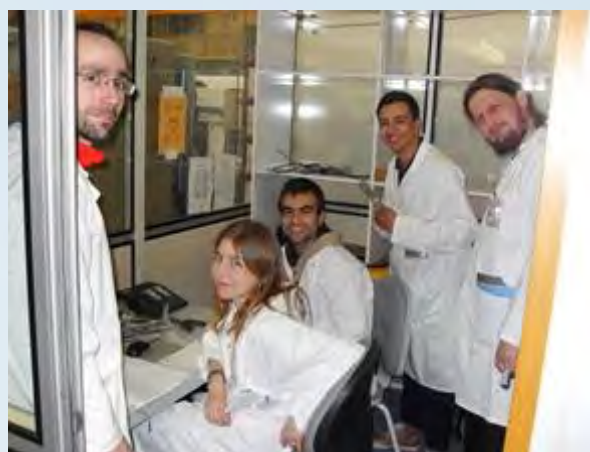
1. LLB annual report 20008-2009, page 53
2. LLB annual report 2012, page 56





TEACHING 2
AND 0
EDUCATION 1 4

HERCULES COURSES (10-14 MARCH 2014)



Hercules, the European graduate school for the large scale facilities users, gathers annually about 70 participants over several weeks for lectures tutorials, and practical sessions on the applications of X-Rays and neutron scattering. A week of this formation takes place in the Paris area, at the SOLEIL synchrotron or at the LLB for those participants interested in a reinforced experimental neutron programme. At the LLB they had the opportunity to exercise on real spectrometers after a general presentation of the installation and a visit of the reactor hall.

In 2014, the LLB was particularly solicited to compensate for the unavailability of ILL closed for repairs during the period of Hercules. Thus nearly 70 students were spread over 18 organized practical work.

LLB-SOLEIL COMMON PHD PROGRAM

SOLEIL and LLB, the two large scale structures of synchrotron radiation and neutron scattering located on the Saclay plateau, have initiated since 2012, an initiative for co-funding of PHD theses are proposed for particularly innovative subjects using complementarities of synchrotron and neutron techniques.

During the last tree years, 6 theses proposed by different French laboratories have been supported and started within this framework.

2012 Call

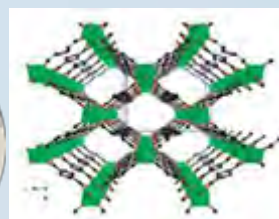
Antiferromagnetic walls: magnetically charged solitons for spintronics?

Camille Blouzon



Impact of water in MOF flexibility. Joint measurement methodology: Synchrotron XRD, NMR and neutrons diffraction/scattering

Damien Foucher



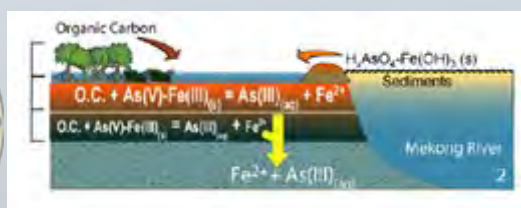
Collaboration:
Institut Lavoisier
U. Versailles-St Quentin

Collaboration: Service de Physique de l'Etat Condensé – CEA Saclay

2013 Call

Are wetlands a source of As to the underlying aquifers: characterization of organic-matter As interactions (imaging / synchrotron radiation / neutron diffraction)

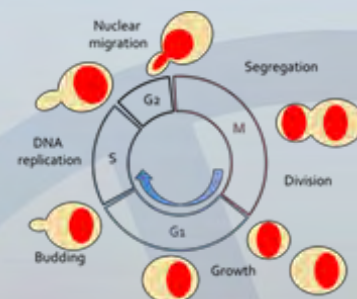
Hélène Guenet



Collaboration: Géosciences Rennes

DNA replication in eukaryotic cells : Relation between chromatin conformation and kinetic of DNA replication

Claire Panciatici

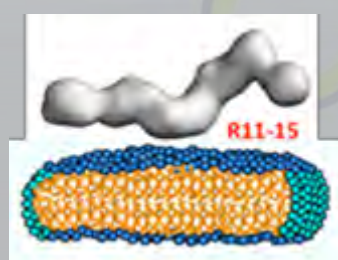


Collaboration: DSV iBiTec-S, CEA Saclay

2014 Call

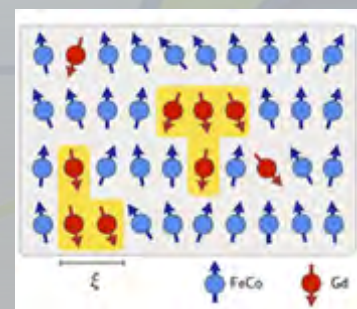
Interfacial proteins / membranes interactions: analysis by SAXS, SANS and molecular modeling of the three-dimensional structure of dystrophin in the presence of membrane lipids

Raphael Dos Santos Moraes



Ultrafast magnetization dynamics in rare-earth transition-metal compounds

Tom Ferte



JDN22 - 21-26 SEPTEMBER ILE D'OLÉRON, CHARENTE-MARITIME



The SFN 2014 prize was awarded by the chairman of the jury, T. Zemb (CEA Marcoule) to M. Deutsch for his thesis work "Experimental modelling of molecular magnets: Combined studies by X-Ray, Neutron and Polarised Neutron Diffraction" performed at the CRM2, Université de Lorraine, in Nancy.



JDN22
22èmes Journées de la Diffusion Neutronique
du 21 au 26 Septembre 2014
Ile d'Oléron, Charente-Maritime

Société Française de Neutronique

**Ecole thématique:
Cristallographie et Neutrons
21-24 Septembre 2014**

**Rencontres Rossat-Mignod
et Prix de thèse SFN 2014
24-26 Septembre 2014**

Organisation
J. M. Kiat, P. E. Janolin (SPMS, Ecole Centrale Paris)
F. Porchet, B. Gilton (LLS, CEA/Saclay)
M. T. Fernandez-Diaz (ILL, Grenoble)

Dates limites:
22 Avril 2014: Candidature au Prix de Thèse SFN
15 Mai 2014: Soumission abstracts (oral)
15 Juin 2014: Inscriptions à l'Académie et aux rencontres et soumission abstracts (poster)

http://www.sfn.jussieu.fr/JDN/JDN22



NEW PHD STUDENTS IN 2014

JENSEN Mikkel

“on the way to form a glass : what about the Debye Peak, structural heterogeneities and Liquid-Liquid phase transition?”

Supervisor : K. Niss, T. Heckher (Roskilde DK)/ C. Alba-Simionesco (*Materials and Nanosciences: Fundamental Studies and Applications*)

DOS SANTOS Raphael (Call LLB/SOLEIL 2014)

«Interactions protéines interfaciales/membranes : analyses par SAXS, SANS et modélisation moléculaire de la structure tridimensionnelle de la dystrophine en présence de lipides membranaires»

Supervisors : J.-F. Hubert (Rennes) / S. Combet (*Soft Complex Matter*)

MALABIRADE Antoine

“Analyse structurale et fonctionnelle des nanostructures formées par les acteurs du métabolisme de l'ARN chez les bactéries”

Supervisor : V. Arluison (*Soft Complex Matter*)

THUAL Marc-Antoine

“Etude de la cinétique de coalescence de nano-oxydes et incidence sur la recristallisation dans des alliages ODS”

Supervisors : M.-H. Mathon/ V. Klosek (*Materials and Nanosciences: Fundamental Studies and Applications*)

FERTE Tom (Call LLB/SOLEIL 2014)

«Ultrafast magnetization dynamics in rare-earth transition-metal compounds»

Supervisors : C. Boeglin (Strasbourg) / S. Petit (*Magnetism and Superconductivity*)

LEANG Marguerite

«Pénétration d'un solvant dans un gel poreux en consolidation : application à la restauration des œuvres d'art»

Supervisors : F. Dauphine (Orsay) / L.-T. Lee (*Soft Complex Matter*)

THESES DEFENDED IN 2014



GUENNOUNI Zineb – June 18 2014

«Etude des films de Langmuir de copolymères diblocs et formation de nanostructures inorganiques par réduction des ions argent à leur voisinage»

Supervisors : M. Goldman (Paris) / F. Cousin (*Soft Complex Matter*)

RIDIER Karl – November 17 2014

«Etudes des relations magnéto-structurales dans les composés à base moléculaire par diffusion des neutrons : des molécules individuelles aux nanoparticules»

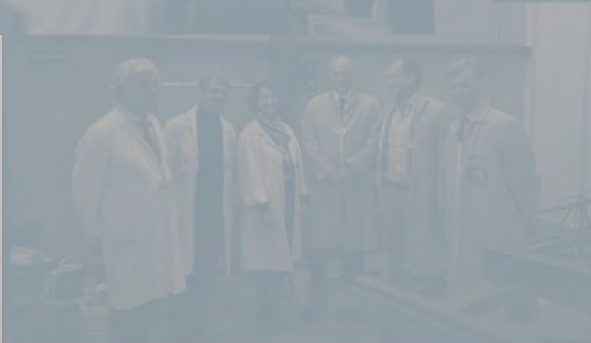
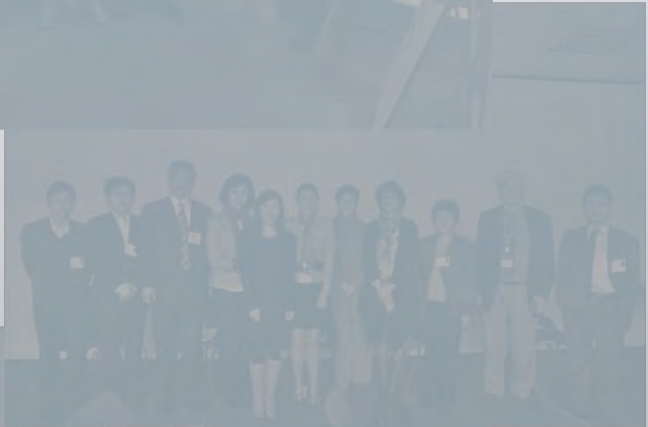
Supervisors : G. Chaboussant / B. Gillon (*Magnetism and Superconductivity*)

GENEVAZ Nicolas – December 18 2014

«Nanocomposites polymères-particules greffées : contribution de la dynamique des chaînes greffées et libres sur les mécanismes de dispersion et les propriétés mécaniques»

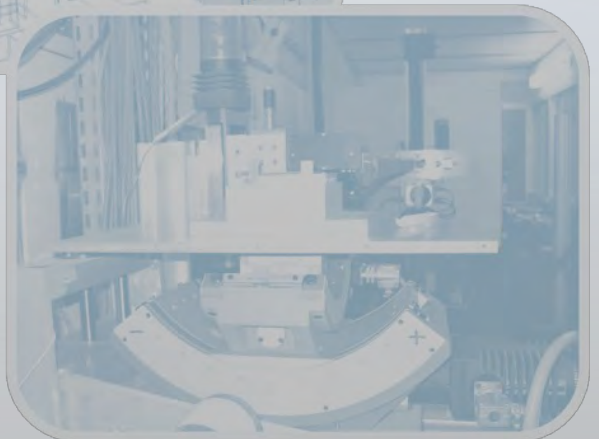
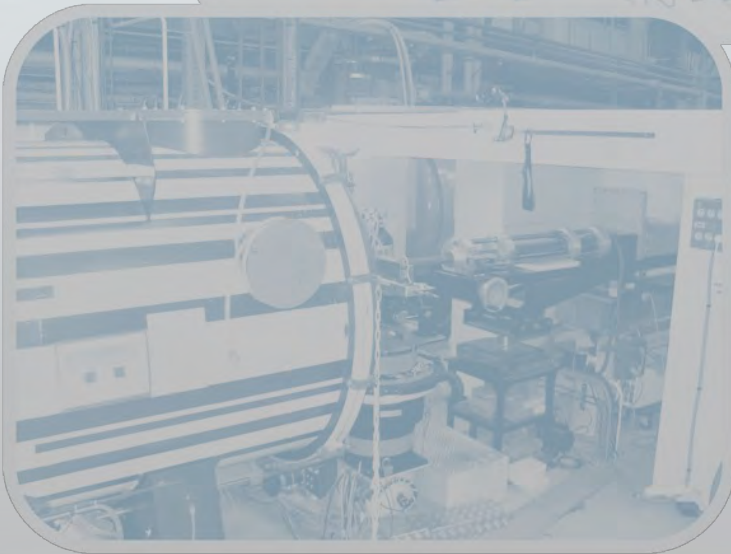
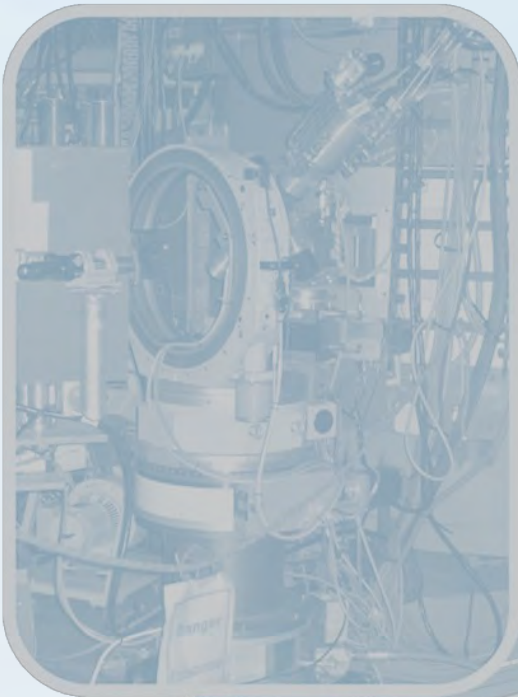
Supervisors : D. Bertin (Marseille) / J. Jestin (*Soft Complex Matter*)



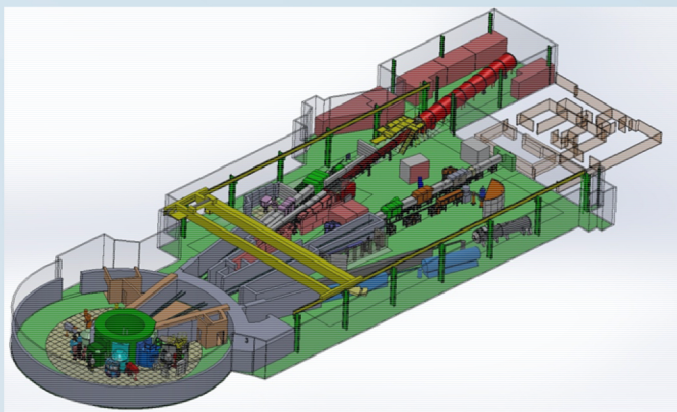




2014
BEAMTIME **1**
ACCESS **4**



GENERAL LAYOUT OF THE SPECTROMETERS



	SPECTROMETERS OPEN TO USERS	CONTACTS
	Powder diffractometers	
3T2	Florence Porcher	florence.porcher@cea.fr
G4.1	Françoise Damay	francoise.damay@cea.fr
G4.4 PHR	Florence Porcher	florence.porcher@cea.fr
G6.1	Florence Porcher	florence.porcher@cea.fr
	Single crystal diffractometers	
5C1 - VIP	Béatrice Gillon	beatrice.gillon@cea.fr
5C2	Alexandre Bataille	alexandre.bataille@cea.fr
Super 6T2	Arsen Goukassov	arsen.goukassov@cea.fr
	Diffuse scattering instrument	
7C2	Louis Hennet	louis.hennet@cea.fr
	Small-angle scattering instruments	
G1.2 - PACE	Sophie Combet	sophie.combet@cea.fr
G2.3 - PAXY	Alain Lapp	alain.lapp@cea.fr
G5.2 - PA20	Gregory Chaboussant	gregory.chaboussant@cea.fr
G5bis - TPA	Annie Brûlet	annie.brulet@cea.fr
	Diffractometers for material science studies	
6T1	Marie-Hélène Mathon	marie-helene.mathon@cea.fr
G4.2 - DIANE	Vincent Klosek	vincent.klosek@cea.fr
	Reflectometers	
G6.2 - HERMES	Didier Lairez / Lay-Theng Lee	didier.lairez@cea.fr / lay-heng.lee@cea.fr
G2.4 - PRISM	Frédéric Ott	frederic.ott@cea.fr
	Triple-axis instruments	
1T	John Paul Castellán / Yvan Sidis (CRG Instrument Karlsruhe/LLB)	john-paul.castellan@cea.fr / yvan.sidis@cea.fr
2T	Philippe Bourges	philippe.bourges@cea.fr
4F1	Sylvain Petit	sylvain.petit@cea.fr
4F2	Jean-Michel Mignot	jean-michel.mignot@cea.fr
	Quasi-elastic instruments	
G1bis - MUSES	Jean-Marc Zanotti	jean-marc.zanotti@cea.fr
	Neutron radiography	
G3bis - IMAGINE	Frédéric Ott	frederic.ott@cea.fr
G4.5	Guy Bayon	guy.bayon@cea.fr

THE LLB-ORPHÉE NEUTRON SCATTERING AND IMAGING INSTRUMENTS

Powder diffractometers

- 3T2** "Thermal neutrons" 2-axis (50 detectors) high resolution, mainly for nuclear structure determination.
- G4.1** "Cold neutrons" 2-axis (multidetector 800 cells) high flux, mainly for magnetic structure determination.
- G4.4** "Cold neutrons" 2-axis (7x10 detectors) high resolution, for structure determination on polycrystalline samples with large unit cell.
- G6.1** "Cold neutrons" 2-axis (high flux, only for friendly users) .

Single crystal diffractometers

- 5C1** "Hot neutrons" 2-axis with lifting arm, polarized neutrons, magnetic field (8 Tesla) for spin-density maps determination
- 5C2** "Hot neutrons" 4-circle for nuclear structure determination.
- 6T2** "Thermal neutrons" 2-axis, lifting arm and 4-circles, mainly for magnetic structure determination. 12 Tesla magnetic field available, 2D detector.

Diffuse scattering instruments

- 7C2** "Hot neutrons" 2-axis (multidetector 640 cells) for local order studies in liquid or amorphous systems. Cryostat and furnace available (1.2K to 1300°C).

Small-angle scattering instruments

- G1.2** "Cold neutrons" (annular detector, 30 rings) for study of large scale structures in isotropic systems (mainly polymers and colloids).
- G2.3** "Cold neutrons" (X-Y detector, 128x128 cells) for study of large scale structures (10 to 500 Å) in anisotropic systems (polymers under stress, metallurgical samples, vortex in superconductors).
- G5.2** "Cold neutrons" (X-Y detector, 128x128 cells) for study of large scale structures (10 to 500 Å) in anisotropic systems (polymers under stress, metallurgical samples, vortex in superconductors).
- G5bis** Very Small Angle Neutrons Scattering spectrometer

Diffractometers for material science studies

- 6T1** "Thermal neutrons" 4-circle for texture determination.
- G4.2** "Cold neutrons" 2-axis for internal strain determination in bulk samples with spatial resolution $\sim 1\text{mm}^3$.

Reflectometers

- G6.2** "Cold neutrons" reflectometer operating in time-of-flight mode for multipurpose surface studies.
- G2.4** "Cold neutrons" reflectometer with polarized neutrons and polarization analysis for the study of magnetic layers.

Triple-axis instruments

- 1T** "Thermal neutrons" high-flux 3-axis instrument with focussing monochromator and analyser, mainly devoted to phonon dispersion curves measurements. High pressure cells (100 Kbar) available. CRG Instrument operated in collaboration with the INFP Karlsruhe
- 2T** "Thermal neutrons" high-flux spectrometer with focussing monochromator and analyser, mainly devoted to spin-waves and magnetic excitations studies (1.5 to 80 meV).
- 4F1** "Cold neutrons" high flux 3-axis instruments with double monochromator and analyzer, mainly devoted to the study of low-energy (15 μeV to 4meV) magnetic excitations. Polarized neutrons and polarization analysis option available.
- 4F2** "Cold neutrons" high flux 3-axis instruments with double monochromator and analyzer, mainly devoted to the study of low-energy (15 μeV to 4meV) magnetic excitations. Polarized neutrons and polarization analysis option available.
- G4.3** "Cold neutrons" high resolution and low background 3-axis instrument, friendly users only.

Quasi-elastic instruments

- G1bis** "Cold neutrons", high resolution and high flux spin-echo instrument. It can study, in a large Q range, slow dynamics of large molecules in biology or long relaxation times like in glassy transition (Fourier times $\sim 20\text{ns}$)

Neutron Radiography

- G3bis** IMAGINE: Imaging station mainly dedicated to soft matter.
- G4.5** Imaging technique : white beam facility for non-destructive control or dynamics imaging (NMI3 access only).

AUXILIARY SERVICES AVAILABLE

http://www-llb.cea.fr/fr-en/spectros_p.php

Laboratories for sample preparation:

- Chemistry laboratory
- Biological laboratory

Technical help for:

- Cryostat, Furnace (0.1 – 2000 K)
- Medium/High pressures
- High magnetic fields (up to 10 T)
- Mechanics, Cryogenics, Vacuum

LLB-SOLEIL COMMON PHD PROGRAM



LLB has been selected in the frame of the European Community – Access activities of the Neutron scattering and Muon spectroscopy Integrated Infrastructure Initiative (NMI3-II) which supports



access to neutron beams for the selected user teams, travel and subsistence fees of visiting scientists. The program is opened to E.C. users and to scientists of the associated states.

<http://nmi3.eu>

Beamtime access is free of charge for any experimentalist from the French Scientific community. LLB takes in charge the expenses (travel and stay) of 2 people during the experiment.

Beamtime on the open-access spectrometers can be requested by submission of:

- **An experimental application to a Selection Committee (Normal Procedure)**
This procedure is open to any public/industrial researcher that is interested in using neutron scattering for his research. Results should be free to be totally or partially published in a Scientific Review.
DEADLINE FOR APPLICATION: April 1st and October 1st
<http://www-llb.cea.fr/en/fr-en/proposal.php>
- **An experimental application to the Directors (Exceptional)**
This special procedure should only be used exceptionally for hot topics, confidentiality reasons or if an anomaly in the review procedure is suspected. The delay between the acceptance decision and the realization of the experiment is shortened to the minimum.
No deadline applies for such propositions (Application all along the year).
<http://www-llb.cea.fr/en/fr-en/proposal.php>
- **A fast access application**
This procedure allows a rapid access (1 to 2 months delay) to the spectrometers in order to perform a short experiment (1 day max.). It can be used for feasibility tests, sample characterization, obtaining complementary results...
No deadline applies for such propositions (Application all along the year).
<http://www-llb.cea.fr/en/fr-en/prop-rap.php>

CONTACT AT LABORATOIRE LEON BRILLOUIN

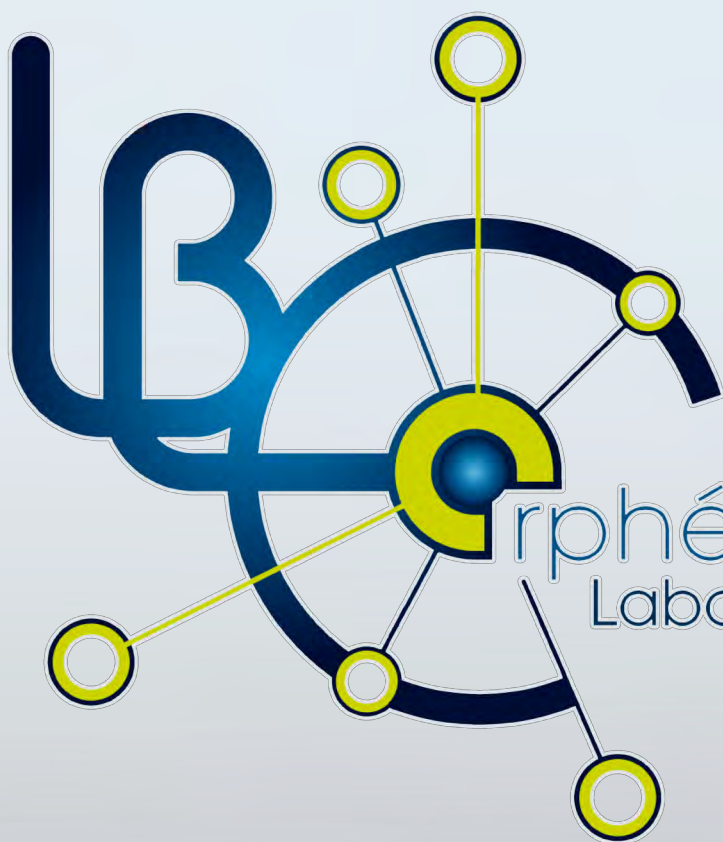
Laboratoire Léon Brillouin

Scientific Office

CEA Saclay - Bâtiment 563
F-91191 Gif-sur-Yvette cedex

Phone: 33 (0)1 69 08 60 38 • Fax : 33 (0)1 69 08 82 61

E-mail : experience-llb@cea.fr • Website: <http://www-llb.cea.fr>



Morphée

Laboratoire Léon Brillouin



LABORATOIRE LEON BRILLOUIN
UMR 12 CEA-CNRS
CEA Saclay, Bât.563
F-91191 GIF-SUR-YVETTE Cedex
France

+33 (0)1 69 08 52 41
+33 (0)1 69 08 82 61
www-llb-cea.fr



université
PARIS-SACLAY